

# **Realisation and Validation of a Biomimetic Mechanosensor assembled by Nanowires and Giant Magneto Resistive Detection**

Dissertation zur Erlangung des Grades eines  
Doktors der Naturwissenschaften der  
Fakultät für Physik der Universität Bielefeld

vorgelegt von

**Philipp Schroeder**, geboren am  
27.06.1980 in Herford

durchgeführt im Geschäftsfeld *Nano  
Systems* des *Austrian Institute of  
Technology* in Wien

18.09.2011

## **Erklärung**

Hiermit erkläre ich an Eides statt, dass ich die Arbeit selbstständig verfasst und keine außer den angegebenen Hilfsmitteln verwendet habe.

(Philipp Schroeder)

Gutachter: PD Dr. Hubert Brückl  
Prof. Dr. Andreas Hüthen

## Table of contents

1 Introduction .....	5
1.1 Motivation .....	5
1.2 Concept.....	6
1.3 Classification of mechanosensors .....	7
2 Characterization and tools .....	11
2.1 Atomic force microscopy (AFM).....	11
2.2 Magnetic force microscopy (MFM) .....	11
2.3 Scanning electron microscopy (SEM).....	12
2.4 Energy dispersive x-ray analysis (EDX) .....	12
2.5 Transmission electron microscopy (TEM).....	12
2.6 X-ray diffraction (XRD).....	13
2.7 Layer deposition and additional tools.....	13
2.8 Electrochemistry.....	14
2.9 Probe station and agitation .....	15
3 Giant Magneto Resistance.....	18
3.1 Interlayer exchange coupling .....	18
3.1.1 RKKY coupling.....	18
3.1.2 Quantum interference model .....	21
3.2 GMR theory.....	24
3.2.1 Intrinsic GMR.....	26
4 Processing.....	28
4.1 GMR-sensors.....	30
4.2 Nanowire synthesis.....	31
4.2.1 Zinc nanowires .....	32
4.2.1.1 Post-synthesis oxidation of Zn nanowires .....	38
4.2.1.2 Morphology alterations during oxidation.....	39
4.2.1.3 Discussion .....	42
4.2.1.4 Zn nanorhombs and nanobelts.....	44
4.2.2 Germanium nanowires .....	47
4.2.3 Polypyrrole nanowires.....	48
4.2.4 Nanorods by electron beam lithography (EBL) .....	51
4.3 Magnetic tagging.....	52

4.3.1 Nanoparticles: thiolate-Au bond (Ge system) .....	52
4.3.2 Sputter deposition and lift-off (Ge system) .....	54
4.3.3 Nanoparticles: EDC-crosslinking (PPy system) .....	55
4.3.4 Nanoparticles: non-specific binding (e-beam resist) .....	56
4.3.5 Sputter deposition .....	57
<b>5 Measurements .....</b>	<b>57</b>
5.1 Zinc nanowires .....	57
5.1.1 Mechanical properties and resonance behavior .....	63
5.1.2 Resonance behavior by means of finite element analysis and SEM characterization .....	63
5.1.3 Conclusion .....	65
5.2 Germanium nanowires .....	66
5.3 Polypyrrole nanowires .....	68
5.4 E-beam resist nanorods .....	72
<b>6 Micromagnetic simulation .....</b>	<b>74</b>
6.1 OOMMF model .....	75
6.2 Polypyrrole nanowires .....	76
6.3 Zinc nanowires .....	79
6.4 E-beam resist nanorods .....	80
<b>7 Conclusion .....</b>	<b>82</b>
7.1 Outlook .....	84
<b>Appendices .....</b>	<b>85</b>
A. Silicon nanowires by wet-etching .....	85
B. Nanowires of polycyanurate thermoset .....	85
C. EDX results of section 5.3 .....	87
D. Conversion of Miller- to Bravais-indices .....	89
E. Processing outline for GMR sensor structuring .....	89
<b>Bibliography .....</b>	<b>91</b>
<b>Publications .....</b>	<b>102</b>

# 1 Introduction

## 1.1 Motivation

Considering a quick growth of the world's population and a decline of fossil resources, environmentally compliant and energy-saving technologies will become more and more important. This is not only demanding for the development of a "green" energy infrastructure but also for sensory intelligence responsible for the surveillance and control of every device (automotive industry, traffic, telecommunication and domestic appliances). Though it has been possible to increase the degree of miniaturization with the aid of micromachining, sensor technology has not been able to draw level with the rapid advancements of microelectronics in recent years. There is a great demand for the implementation of novel, functional materials (e.g. organic and nanostructures) and techniques to be integrated in state of the art device fabrication. In order to increase sensor performance it is worthwhile to have a look at natural methods. Biomimetics is a field that treats the emulation of natural or biological principles - that can be processes, materials and structures - for technological reasons. The term composed of "bios" meaning life and "mimesis" meaning imitation was first utilized in 1969. While with "bionics" a combination of biological and mechanical issues is meant, biomimetics focuses on the direct mimicry or at least bio-inspired systems. Though gaining ever-increasing relevance in science and technology, major attention was dedicated to biomimetics in the last two decades because general advancements, e.g. in the information technology and in particular in the nanotechnology motivated and enabled significant progress in the field. In the following, some capabilities of natural "engineering" are discussed.

In billions of years of evolution the pressure of natural selection has forced life forms to reach a high level of optimization. Nature accomplishes this by "trial and error experiments" without a plan or logical demand but that lead to efficient performances unattainable by human engineering. The necessary information is stored in the species genes and passed from one generation to the other by replication. Cellular structures for instance feature fault tolerance and the ability of self-repair. Spider silk is a sophisticated protein-based material with a tensile strength of 1154 MPa that is - though produced at "room temperature" - superior to steel (400 MPa). Beside functional materials [1] biomimetic principles are also applied in ecology and information technology. Genetic algorithms are nowadays successfully applied for complex simulations, e.g. antenna design by the NASA. Furthermore there are attempts for the mimicry of behavioral aspects in ant colonies [2] for crowd dynamics much less the field of artificial intelligence [3]. Birds inspired aircraft engineers for using winglets at the wingtips of aircrafts that help to reduce flow vortices and thus saving fuel. Likewise the fin appendages of humpback whales are considered for being mimicked for water vehicles and wind energy plants to improve buoyant forces and efficiencies [4]. For medical applications and prosthetics, electro-active polymers [5] open up new possibilities.

An exciting area within biomimetics is the entity of mechanosensors that appear in almost every living being and serve for localizing predators or prey, regulating metabolism and reproduction. There are various designs of mechanoreceptors formed of sensory hair cells - called *cilia* - that serve in insects, vertebrates and e.g. the mammalian inner ear for the detection of vibration, flow or inertial forces in disordered, noisy environments. Fish use its lateral line system consisting of hair-like cilia as a sense for hydrodynamic imaging of the surrounding [6]. The cricket (Fig. 1a) possesses one of the most sensitive flow sensory organs known [7]. Two abdominal appendages (cerci) are equipped with approximately 2000 cilia hairs (Fig. 1b) each resting on a neural membrane. A wide length distribution between 30  $\mu\text{m}$  and 1500  $\mu\text{m}$  and 1-9  $\mu\text{m}$  in diameter at the base allows for a detection of the predators (wasp) wing beat.

Such an air-flow induced stimulus causes a drag force - rotation of the hair base - that is processed by the cilia array and “transduced” to the nerve (Fig. 1c) via ion channels ( $K^+$ ,  $Na^+$ ) when a threshold potential is exceeded. This way the concept is very sensitive. For example, the work necessary to cause a threshold displacement in these filiform hairs amounts to  $9 \times 10^{-20} - 8.4 \times 10^{-19}$  Joules<sup>1</sup> [8]. Mechanoreceptors have proven to be 100 times more sensitive than photoreceptors [9] due to a missing quantum structure of their stimuli. The optimization goes down to the thermal noise limit while the action potential lies above  $k_B T$  to avoid invalid responses.

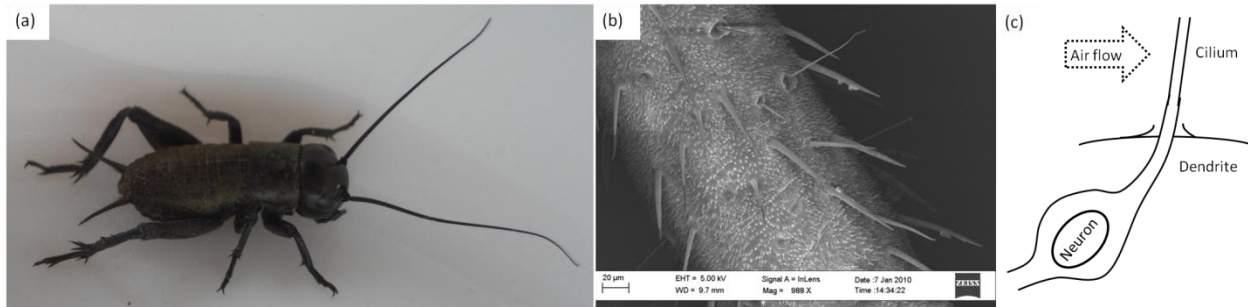


**Figure 1: House cricket (*acheta domesticus*) (a) with cercal filiform hairs (b) for flow detection. A schematic cilium cross-section is shown in (c).**

## 1.2 Concept

The presented approach for bio-inspired mechanosensing is based on self-assembled nanowires (NW) which serve as artificial cilia. To that end, particularly germanium (Ge), zinc (Zn) and polymeric structures are investigated and assembled on top of giant-magneto-resistance (GMR) multilayer sensors. Next, a magnetic component is attached (tagged) to the NW arrays. Any stimulus caused by shock or acceleration deflects the structures together with the tagging. Consequently, the magnetic stray field of the tag changes its position relative to the underlying sensor, which can be registered via a reorientation of the sensor’s magnetization state (see Fig. 2). For testing, the devices are agitated with piezo actuators. When agitated, an in-plane current is applied to the GMR sensor, and the output signal is given by the absolute value of the sensor AC voltage drop synchronized at the agitating frequency. The output is registered by a lock-in amplifier (LIA) in dependence on agitation frequency. The demonstrated sensing approach features novel magnetic detection of nanowire oscillations, moderate process complexity (no sensor micro-patterning required) and is proven to be robust and compatible with standard device fabrication methods. The presented detection principle is related to the balance sensing of mammals that detect inertial forces via small mineral deposits connected to the inner ears cilia by ionic transport [10]. The natural and the artificial system both comprise a mass attached to the cilium which causes its deflection under an external stimulus. As characteristic time scales for magnetization switching lie in the nanosecond regime [11], it is reasonable to assume instantaneous reorganization of the sensor’s magnetization within the range of applied agitation frequencies (kHz regime).

<sup>1</sup> This energy compares to that of a single photon for visible light with  $10^{-18} - 10^{-19}$  Joules.

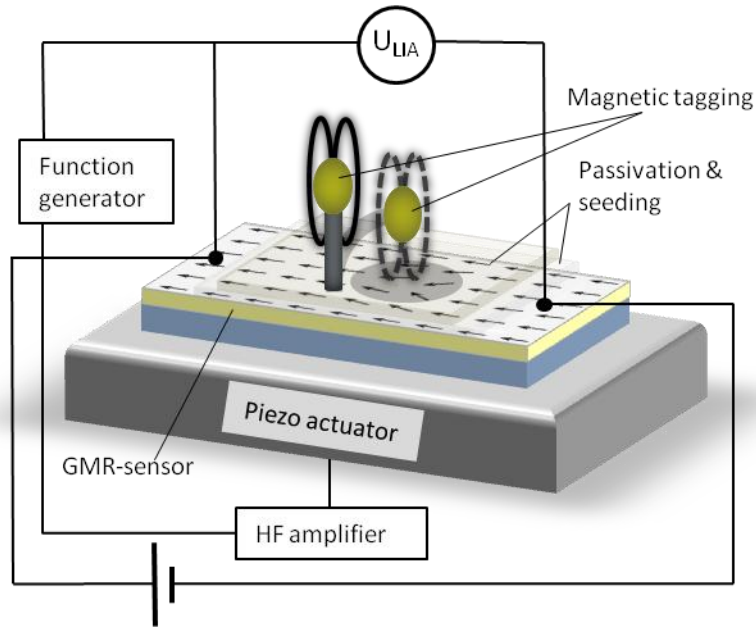


**Figure 2: Schematic measurement setup illustrating the sensor principle by means of one single NW, which comprises a magnetic tag (yellow ellipsoid). The piezo actuator delivers a mechanical stimulus that forces the NW to bend towards the sensor in vertical direction. Consequently, the stray field of the tagging changes relative to the underlying GMR sensor (dashed ellipses). The resulting resistivity change can be measured in reference to the agitation frequency with a lock-in amplifier.**

### 1.3 Classification of mechanosensors

Different sensing approaches for the detection of mechanical stimuli by mechanosensors are addressed in this section. The current technology applies a variety of measures and approaches for the detection of e.g. forces, distances, angles or pressures, such as the electrical resistance (strain gauge), electromagnetic induction, piezoelectricity and inertia. Magneto resistive sensors, on the other hand, are predominantly applied to measure distances or rotation cycles of driving shafts. The most prominent functionalities for vibration or acceleration sensors, however, utilize piezoelectric or capacitive means [12]. Fig.3a shows a cantilever-type vibration sensor equipped with an inertial mass. Any stimulus causes strain in the piezoelectric beam and a voltage output. The output signal can be tuned by a modification of the mass. Accelerometers usually apply capacitive spring-mass systems, the degree of miniaturization of which has been enhanced by micromachining and MEMS (micro-electro-mechanical-systems). In Fig. 3b, miniaturized tri-axial acceleration sensors from Bosch are depicted. In order to achieve dimensions of few millimeters, folded springs and proof masses are patterned directly into a silicon wafer by utilizing the highly anisotropic deep reactive ion etching technique [13]. Electrode sets, one of which fixed and the other one attached to the (moving) proof mass, form capacitors with an air gap in between, which allows for the detection of acceleration. Application is envisioned for example for auto-motion, cell phones and entertainment. The detection range spans up to 16 g.

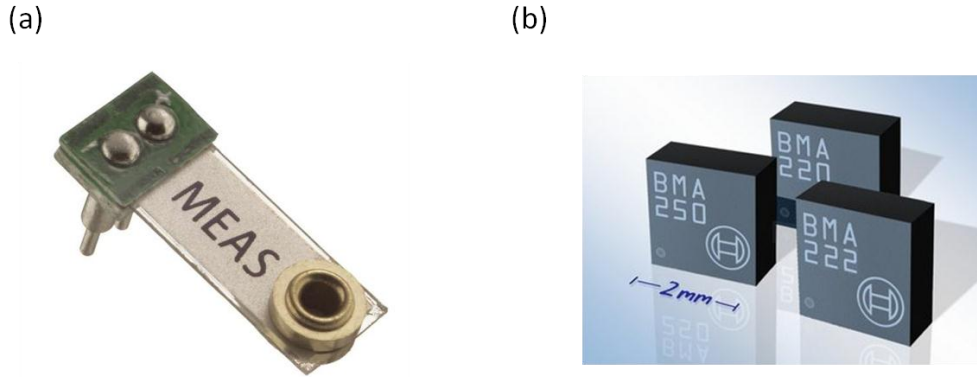


**Figure 3:** Cantilever-beam vibration sensor “MiniSense100” (taken from [14]) (a). Bosch micro-machined acceleration sensor for automotive / airbag application (taken from [15]) is shown in (b).

Moreover, it is reported on a design for the detection of pressure via the field effect of a diaphragm-like field effect transistor (FET) [16]. Recent progress in MEMS-processed single cilia and cilia arrays for sensing and actuation applications is surveyed in [17] and [18]. Fig. 4a shows a piezoresistive flow sensor composed of a semiconductor cantilever arranged on a piezoelectric strain gauge [19]. By means of its response curve (Fig.4b), it is obvious that the resistance of the device increases with increasing air flow rate (at a constant voltage biasing).

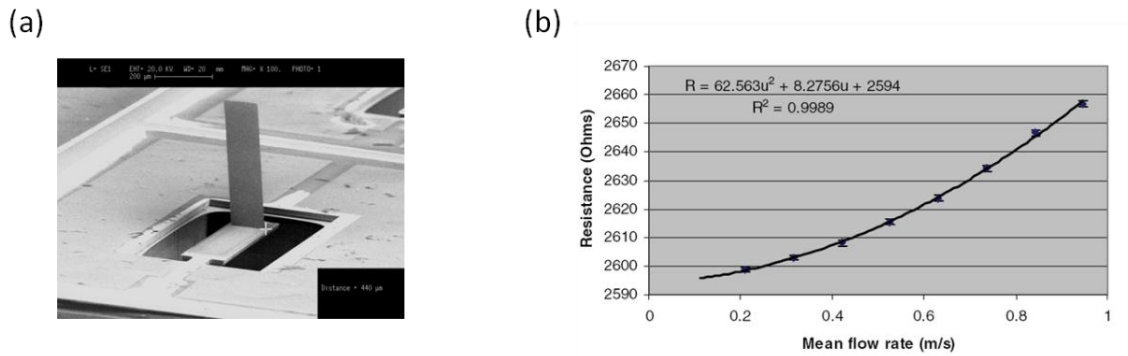


**Figure 4:** SEM image of a single-cilium MEMS-based flow sensor prototype (a) with response curve (b) (taken from [19]).

A biologically inspired fish “lateral line organ” comprising micro-machined artificial cilia has been modeled with a piezoresistive read-out as well [20]. The organ which serves the animal for flow detection and hydrodynamic imaging has been mimicked by an array of polymer cilia structured on a piezoresistive base (Fig. 5).



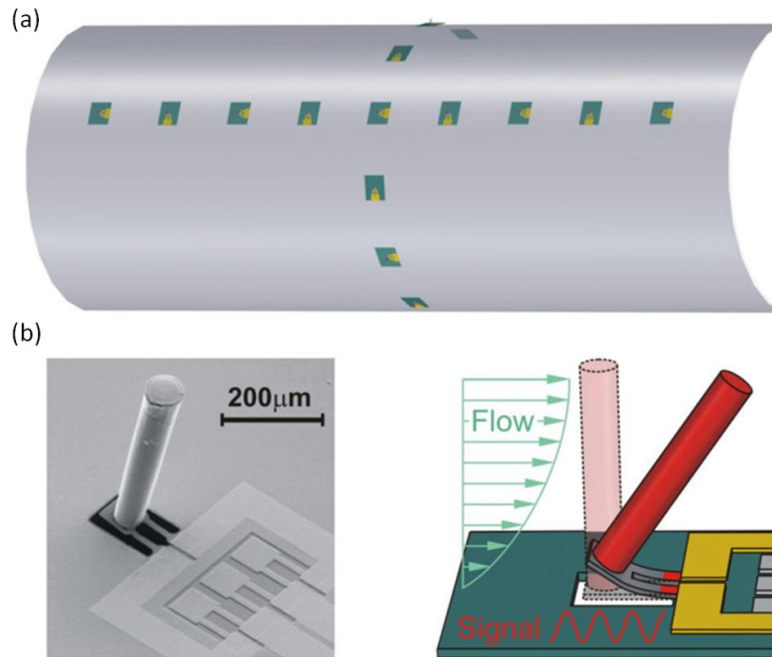


**Figure 5: Artificial fish lateral line organ (a) composed of units of polymer rods positioned on a moveable piezoresistor bridge (b). Water flow affecting the cilium leads to bending of the bridge (marked red on the right) and an analogue output voltage (taken from [20]).**

Comparable work conducted by Krijnen et al. deals with the fabrication of a MEMS-based array of artificial flow-sensitive hairs of SU-8 which are intended to resemble the natural flow-sensory system of cricket (Fig. 6a, b). The detection is carried out via double capacitors that are MEMS-structured for each of the photo-resist (SU8) rods [21]. Therefore, a sophisticated and highly complex “six-mask” lithography process including seven different etching steps is necessary for the array implementation on a suspended membrane.

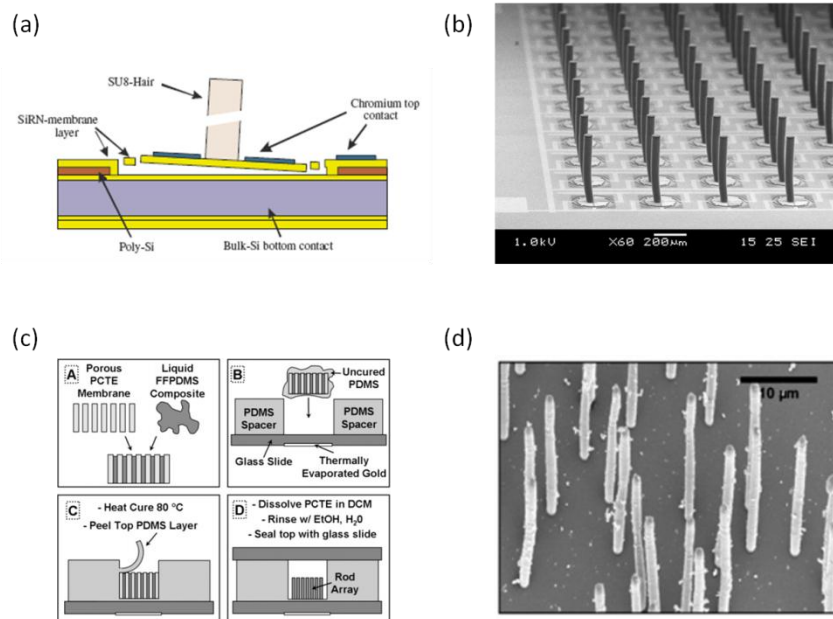


**Figure 6:** Cross-section of a single, MEMS-fabricated flow sensor unit (a). The corresponding array is shown in (b) (taken from [21]). Template fabrication of superparamagnetic rods is shown schematically in (c) while a SEM image of the final structures is shown by means of SEM in (d) (taken from [23]).

Such macroscopic structures with sizes in the micro- to millimeter range can also be designed to allow magnetic manipulation [22]. Another route for the assembly of artificial cilia is to use alumina or polycarbonate membranes as templates into which metallic or plastic structures are “filled”. Subsequently, the templates are removed and arrays of structures with dimensions of a few microns can be bound to various substrates (Fig. 6c). This way, it is reported on a superparamagnetic PDMS composite that can be actuated magnetically for fluid manipulation [23]. However, the structures show high risk of collapse during processing (Fig. 6d). By similar means, another group produced nanowires of magnetostrictive GaFe as sound transducers in an artificial cochlea [24]. A bending of the nanowires caused by an acoustic wave is intended to be registered by GMR sensors via the magnetic flux. Especially for motile artificial cilia applied in the manipulation of biochemical fluids, magnetic actuation is advantageous due to low sample interaction. Therefore, ferro- and superparamagnetic polymeric (polydimethylsiloxane PDMS) microstructures can be fabricated inside micro-fluidics and agitated by external magnetic fields [25]. The achievements in the field of MEMS technology, however, are connected with huge development costs that account for a high processing complexity and specificity of the devices [19]. Consequently, there is a demand for strategies that address the integration of novel material systems and production techniques into the standard fabrication scheme to extend sensor intelligence. An example is given by flow sensors which are composed of carbon nanotubes [26]. In order to overcome the current drawbacks of MEMS, a robust, low-cost implementation accompanied by an increased miniaturization should be targeted. In this regard, functional and organic materials, e.g. polymers, low dimensional structures and biologically inspired mechanisms are promising. One could, therefore, exploit self-assembly systems that establish spontaneously in a bottom-up manner, resembling mechanisms applied by nature. In the first part of this work, the suitability of different nanowires as artificial cilia for the mechano or acceleration sensing concept is investigated.

## 2 Characterization and tools

### 2.1 Atomic force microscopy (AFM)

AFM belongs to scanning probe methods, which allow for a thorough characterization of specific surface properties. In particular, AFM is used to detect surface forces ( $<1$  nN) that act on a small probe tip which is scanned over the sample surface. According to the surface topography, forces of different magnitudes can be registered proportionally to the deflection. The tip with usual front diameters of 5-10 nm is structured on a cantilever, the deflection of which is read out optically with the aid of a laser beam. The beam is reflected from the backside of the cantilever and projected onto a four-quadrant photodiode (see Fig. 7). Thereby the cantilever deflection delivers information about the sample topography while its torsion reflects the friction. Generally, there are two operational modes, i.e. contact and non-contact mode. In the former case, the scanning is performed with a constant deflection and the working point is adjusted to the repulsive regime to allow for most sensitive operation. In the non-contact mode, the tip is brought to oscillation in a force gradient present between tip and sample. Depending on whether the forces are repulsive or attractive, the distance between tip and sample varies and the systems resonance is shifted to lower/higher frequencies. The corresponding phase change is particularly very sensitive to eigenfrequency changes.

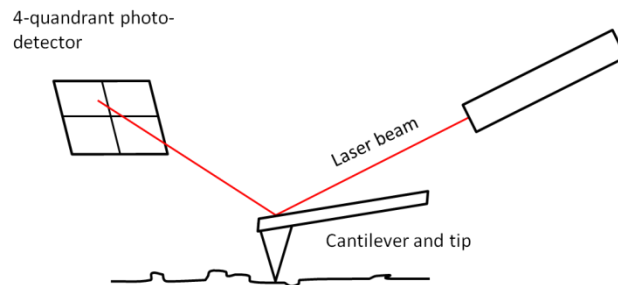


Figure 7: Schematic principle of AFM.

AFM characterization and layer thickness calibration is carried out with an instrument from “Molecular Imaging (Pico Plus)” in the tapping mode with tips of type: PPP-NCHR-50 from “Nanosensors”. For scanning, the software “AFM PicoView 1.6” is utilized.

### 2.2 Magnetic force microscopy (MFM)

By means of MFM, magnetic stray fields transverse to the sample surface can be registered with a maximum spatial resolution of 30 nm. During scanning, the tip experiences forces of different polarities according to the samples superficial domain configuration.

Magnetic surfaces are characterized with the AFM instrument and cobalt coated tips from “Nanosensors” (PPP LM MFMR-20: low moment, hard-magnetic) and “NanoWorld” (MFMR 50: hard-magnetic). For scanning, the software “AFM PicoView 1.6” is utilized. The MFM images are recorded at an interleave height of 80 nm.

## 2.3 Scanning electron microscopy (SEM)

SEM characterization allows for imaging of conducting surfaces with resolutions down to a few nanometers. The electron beam is generated via field emission or thermal release from a filament (e.g. tungsten) and manipulated with magnetic lenses. When scanning over the sample surface, either backscattered or secondary electrons are registered with a detector. At each site, the detector measures the intensity and composes an image from the information of the whole scan.

SEM characterization is mainly carried out with a “Supra 40” instrument from Zeiss. It is equipped with a “Raith” writing unit. Furthermore, a “Philips XL40”, a “Zeiss Neon 40XB” and a “Raith e-line” are utilized.

## 2.4 Energy dispersive x-ray analysis (EDX)

EDX is a means for elemental sample analysis. The systems are usually mounted inside a SEM to provide the electron beam that serves for the excitation of element specific x-rays from the sample. For the efficient capture of x-rays, an additional photo-detector is necessary. Commonly semiconductor type detectors are utilized that have to be operated at liquid nitrogen temperatures. Electron exposure of the sample material leads to a release of electrons from the inner orbitals (e.g. K-shell). Consequently, electrons from higher orbitals (e.g. L1-shell) relax into the unoccupied states accompanied by the emission of characteristic radiation. The energy transition from one orbital to the next is element-specific. The resulting spectral lines can easily be distinguished with a resolution of about 100 eV.

EDX analysis' are carried out with an “Oxford Inca energy 200, Si (lithium)” detector.

## 2.5 Transmission electron microscopy (TEM)

In contrast to SEM, in a TEM the electron beam transmits the sample. To that end, a thin (few microns thick) sample is positioned on a copper grid. Resolution is determined by the electron *de-Broglie* wavelength following the Rayleigh criterion:

$$\Delta x \approx 0.5\lambda, \text{ with wavelength } \lambda = \frac{h}{\sqrt{2m_e eU}} \quad (2.1)$$

Though the resolution is limited by aberrations of the electromagnetic lenses, it can be improved by the acceleration voltage  $U$  (usually around 200 kV). For imaging, e.g. the contrast of scattered electrons can be adducted. Furthermore, characterization is possible by means of the phase contrast. By interfering electron waves which experience a phase lag (e.g. caused by the Coulomb potential) with respect to the primary wave, defects become visible. Information about crystalline orientation of the sample can be gathered with the aid of diffraction patterns. By this means, highly resolved lattice imaging is feasible. One drawback of high performance TEM characterization is the often complex sample preparation necessary for the thinning (grinding, ion milling).

TEM characterization is carried out with “JEOL 200 CX” microscope, whereas high-resolution images are performed with a “FEI Tecnai F-20”.

## 2.6 X-ray diffraction (XRD)

XRD is a method for the chemical, i.e. element-specific, characterization of crystalline matter. Here, the sample is exposed to an x-ray beam emanated e.g. from a tube source. Prior to the exposure, all wavelengths except the one of interest get selected by a *monochromizer*. The diffracted light from the sample is then passed through an analyzer to suppress in-elastically scattered quanta and subsequently registered by the detector. Usually the intensity is scanned as a function of  $2\theta$  due to the fact that in a common setup the rotation of the sample by the angle  $\theta$  has to be compensated for by a detector turn of  $2\theta$  (see Fig. 8). Based on the Bragg condition

$$2d\sin\theta = n\lambda, \quad (2.2)$$

the lattice distance can be determined. Microscopically, the x-ray wave is scattered at the electron cloud of the respective atom. Thereby, the electrons are agitated to harmonic oscillations which itself emit radiation at a frequency of the incident wave. In fact, the resulting macroscopic electric field is given by a superposition of single scattering events. It is composed of a factor of the Bragg condition and the “structure factor” which accounts for information of the respective crystalline structure as well as the atom charge distribution (atomic form factor).

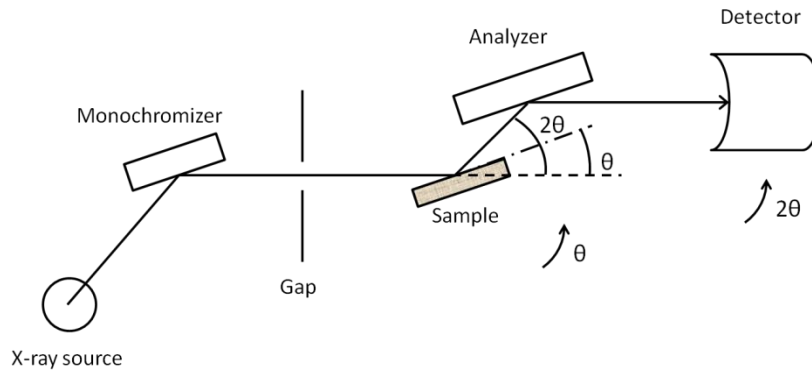


**Figure 8: Schematic setup for x-ray diffraction analysis.**

XRD characterization is carried out in a “X’Pert PRO” diffractometer from “PANalytical, Almelo/NL” with Ni-filtered Cu  $K_{\alpha}$ -radiation.

## 2.7 Layer deposition and additional tools

In the present work, a magnetron-sputtering device “Leybold Univex 450 C” comprising 11 targets (3 and 4 inches) is utilized. Unless stated otherwise, all materials are sputter deposited with Ar gas at a pressure of 2  $\mu$ bar and a constant gas flow of 6 standard cubic centimetres per minute (scm).

Further characterization and layer thickness calibration is carried out with optical microscopes of type “Leica DM 2500 M” and a “KLA Tencor”  $\alpha$ -step IQ surface profiler, respectively.

## 2.8 Electrochemistry

Recently, electrochemistry, which can briefly be described as the science of electron transfer reactions on phase boundaries, gained significant technical relevance owing to its versatility. With the aid of galvanic cells comprising an electrolyte solution and a set of electrodes (see Fig. 9), a variety of materials can be deposited as coatings (e.g. metals) or synthesized by electrolysis [27]. Depending on the electrolyte and the electrode material, anodic or cathodic deposition can occur, whereas the agents who attend the electrode reactions are not necessarily those which carry the current. Even the deposition of thin polymeric layers via oxidative polymerization is possible. By applying an adequate potential to the monomer solution, a film assembles on the electrode surface, the properties of which depend on parameters like cell geometry, choice of solvent, background electrolyte, temperature and pH. The higher the concentration of the monomer, the faster and less uniform the deposition.

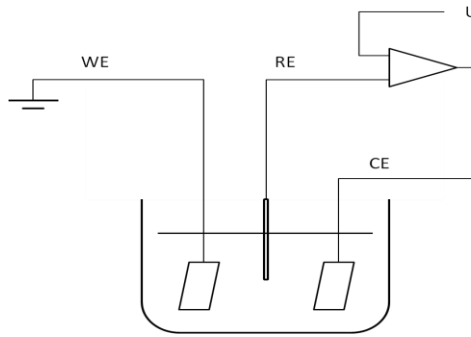


**Figure 9: Schematic electrochemical setup at a constant potential. The operational amplifier adjusts the potential difference between its inputs to zero. The abbreviations signify working, reference and counter electrode, respectively.**

The polymerization process is initiated by the monomer oxidation at the anode surface (WE). Subsequently, oligomer formation occurs via the formation of  $\sigma$ -bonds between two  $sp^3$ -hybridized carbon atoms [28]. The film thickness is determined by the passed anodic charge  $Q_p$  which defers from the total charge  $Q_{tot}$  by a factor  $f_p > 1$  that describes losses, e.g. caused by side reactions, oligomer generation in the bulk solution or outside the electrode surface or intermolecular bonds between chains:

$$Q_{tot} = f_p \cdot Q_p \quad (2.3)$$

For moderate applied potentials, the number of monomer units  $N_m$  is proportional to  $Q_p$ :

$$N_m = \frac{Q_p}{(2+q_p)F} \quad (2.4)$$

The “2” accounts for two electrons withdrawn from each monomer to form  $\sigma$ -bonds with two neighboring elements inside the chain, while  $q_p$  is the extra charge that is used to withdraw electrolyte anions for the oxidation.  $F$  denotes the Faraday constant. The solubility of the oligomers reduces with increasing chain length (6-10 units), meaning that when exceeding the threshold, the oligomers are deposited at the electrode. The subsequent polymerization includes a trapping of anions from the electrolyte that determine the electronic properties of the film.

Electrochemical experiments are carried out in an “Autolab” potentiostat (PGSTAT 30) under *potentiostatic* conditions at a potential of 0.7 V against a Ag/AgCl reference electrode.

## 2.9 Probe station and agitation

Measurements are performed in a home-built probe station consisting of a coil arrangement for lateral magnetic fields (X,Y-direction), a pair of Helmholtz-coils and a sample chuck with a tip setup for the four-point transport measurements. The Helmholtz coils serve for the generation of homogeneous magnetic fields up to a magnitude of  $450 \text{ Oe}^2$  in vertical direction. However, for long time periods, i.e. several hours, the setup is restricted to fields of 100-150 Oe. Otherwise strong Joule heat generation harms the coil insulation. Furthermore the probe station is equipped with a large focal distance microscope (Fig. 10a). Alternatively, the chuck can be replaced by the piezo drive setup (Fig. 10b).

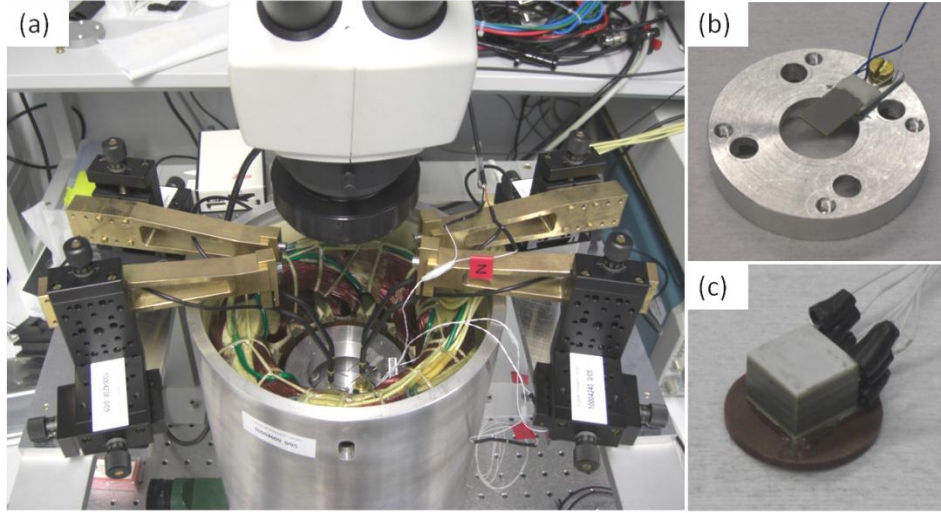


**Figure 10: Probe station with stator coils, microscope and tip holder construction. The shiny ring inside the pot exhibits the Helmholtz coils for z-field generation (a). Chuck with mounted cantilever actuator (b) and shear actuator (c).**

Two different piezo actuators consisting of lead-zirconium-titanate ceramics (“PI Physikalische Instrumente”) are applied for device testing. The commercially available instruments stand out for low power requirements, robustness due to ceramic encapsulation and high duty cycle dynamic operation. Bimorph-type cantilever actuators (“PL127.10” and “PL112.10”) capable of large displacements up to  $\pm 400 \mu\text{m}$  (statically) as well as a  $10 \times 10 \times 7 \text{ mm}^3$  shear stack (“P-143.01”) for extensions in three spatial dimensions are utilized (Fig. 10b, c). Both designs are powered with the respective custom amplifiers (“PI E-650.00” and “PI E-413.00”) and non-magnetically implemented with silver-palladium instead of nickel contacts. Voltage amplification applies to a factor of 6 and 50, respectively. Due to blocking forces of only 1-2 N, the cantilever actuators are restricted to low frequencies. Since the concept necessitates the agitation up to hundreds of kHz, the tests for all displayed measurements are performed with the multi-axis shear actuator. Its low capacity of 5.6/5.6/11nF in x/y/z direction and high blocking force of 200 N enable an operation in the kHz regime. In this respect, it has to be noted that the extension decreases with increasing agitation frequency. Two scenarios are responsible for this effect. The first is the dynamic force  $F_{dyn}$ , which can be estimated for sinusoidal operation and a given peak-to peak extension  $\Delta L$  by the applied frequency  $f$  according to

$$F_{dyn} = \pm 4\pi^2 m_{eff} \frac{\Delta L}{2} f^2, \quad (2.5)$$

<sup>2</sup> For clarity reasons, magnetic field strengths are indicated in Oersted in the following. 1 Oe amounts to 79.577 A/m.

with  $m_{eff} \approx m/3$  being the effective actuator mass [29]. Once  $F_{dyn}$  exceeds the blocking force, the piezo extension vanishes. Assuming e. g. a sample mass of 0.6 g and an extension of 40 nm, the maximum frequency can be estimated to about 460 kHz in case of the shear instrument.

The second issue is a limitation caused by the output current of the amplifier. The higher the frequency gets, the more charge has to be transferred between the amplifier and the piezo drive as capacitive load. The current necessary for the charge transfer is given by

$$I = C \frac{dU}{dt} \approx fCU_{pp} , \quad (2.6)$$

with  $C$  and  $U_{pp}$  being the piezo capacity and applied peak to peak voltage, respectively. During the measurements it turned out that the amplifier which drives the shear stack provides sufficient output current. The input wave is provided by an ‘‘Agilent 33220A’’ function generator.

In order to overcome the drawback of heating in the coils, a setup including two permanent magnets which sandwich the sample equidistantly, is set up as an alternative to the electromagnets. The NdFeB-discs ( $\emptyset$  40 mm, thickness 3 mm) are separated by 20 mm (see Fig. 11a, b) to allow for a symmetric positioning of the piezo actuator and the sample. A to scale cross-section of the setup is shown schematically in Fig. 11c. The intention of this setup is to achieve larger magnetic fields than those which can be generated with the coils of the probe station for a longer period of time. Though the z-fields are indeed stronger ( $\sim 1900$  Oe directly centered on the surface and  $\sim 650$  Oe at a distance of 10 mm of one single disc, measured with a Hall-probe), they are also less homogeneous and much larger in-plane field components of approximately 80 Oe evolve (centered at a distance of 10 mm). Since such large lateral fields are expected to saturate the GMR field sensors, which would erase any signal originating from the tagged NWs, the measurements have been performed with the Helmholtz coils of the probe setup.



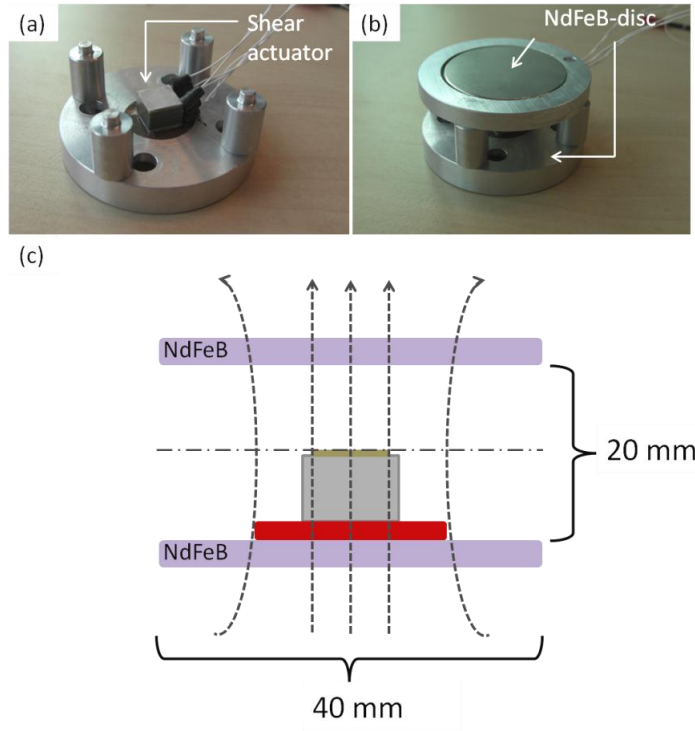


**Figure 11: Alternative setup which includes the shear actuator and two stacked NdFeB discs (a, b). A to scale scheme of the setup is depicted schematically in (c).**

For characterizing the sensors GMR amplitudes, a strong, water-cooled yoke-type electromagnet was calibrated and utilized (see Fig. 12).

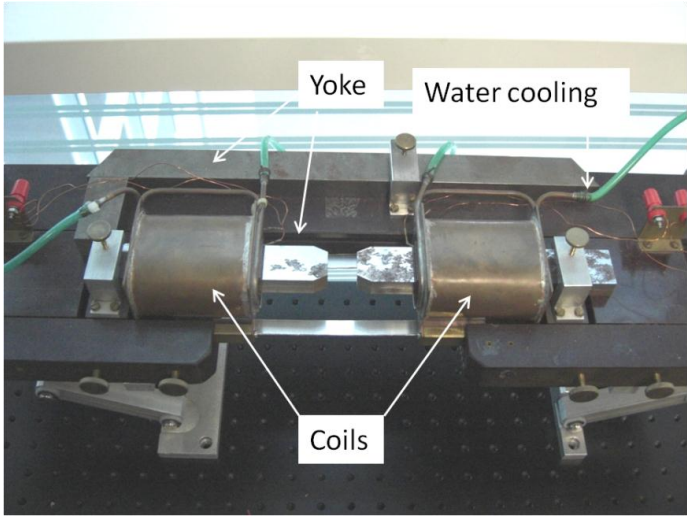


**Figure 12: Yoke-type (iron) electromagnet consisting of two water-cooled coils and a yoke loop to apply magnetic fields of up to 4 kOe in the air gap.**

## 3 Giant Magneto Resistance

In 1988, Grünberg [30] and Fert [31] discovered a resistivity dependence of alternately arranged Fe/Cr films on external magnetic fields. This giant magneto resistance is independent of the angle between current and magnetic field direction, by which means it differs from the AMR (anisotropic magneto resistance), that was found earlier in ferromagnetic metals. By now, the GMR has been found in a variety of material systems [32]. Due to its relevance in sensor applications, e.g. in read heads of magnetic hard disc drives, the GMR effect has triggered a lot of research effort and its discovery was awarded with the *Nobel prize* in 2007.

In the thin Fe films, an indirect exchange interaction prevailed across the Cr spacer layer that provided the required magnetic ground state condition, i.e. opposing magnetization directions in consecutive Fe layers. Parkin et al. showed that this so-called *interlayer exchange coupling* - found in 1986 [33] - oscillates as a function of thickness of the metallic spacer [34]. In order to obtain large GMR amplitudes, the thickness must correspond to antiferromagnetic (AF) rather than ferromagnetic (FM) coupling. Besides the interlayer coupling, the AF ground state can also be achieved by exchange biasing and hysteresis [35] effects in spin valves.

### 3.1 Interlayer exchange coupling

#### 3.1.1 RKKY coupling

The RKKY-interaction describes the interaction of isolated magnetic moments in metallic host crystals. It is referred to the original theory established by Rudermann, Kittel, Kasuya and Yosida [36], which utilizes perturbation methods.

In this section, basic aspects are outlined that address the transition from the RKKY interaction towards the interlayer coupling following [32]. At first, a nonmagnetic impurity in a non-magnetic host as a free-electron medium is considered. The electrons screen the potential of the impurity and thus lower its value  $V$ . The consequent change in electron density  $\Delta n$  is given by

$$\Delta n(\mathbf{r}) = \int \chi_0(\mathbf{r}, \mathbf{r}') V(\mathbf{r}') d(\mathbf{r}'), \quad (3.1)$$

where  $\chi_0(\mathbf{r}, \mathbf{r}')$  is the free-electron susceptibility. It describes the electron density change at a position  $\mathbf{r}$  caused by a Delta-potential jump at  $\mathbf{r}'$ . The integration is done over the impurity volume. For a weak defect potential and isotropically scattered electron waves emanated from point  $P$ ,  $\chi_0$  becomes

$$\chi_0(\mathbf{r} - \mathbf{r}') = -\frac{2m}{\hbar^2 4\pi |\mathbf{r} - \mathbf{r}'|^2} \int_0^{k_F} \sin(2k |\mathbf{r} - \mathbf{r}'|) k dk \quad \text{with } k = \sqrt{\frac{2mE}{\hbar^2}}. \quad (3.2)$$

Thereby  $m$ ,  $E$  and  $k_F$  denote electron mass, energy and Fermi wave number. After integration and with  $R = |\mathbf{r} - \mathbf{r}'|$ , it applies:

$$\chi_0(R) = \frac{m}{\hbar^2 (2\pi)^3 R^4} (2k_F R \cos(2k_F R) - \sin(2k_F R)). \quad (3.3)$$

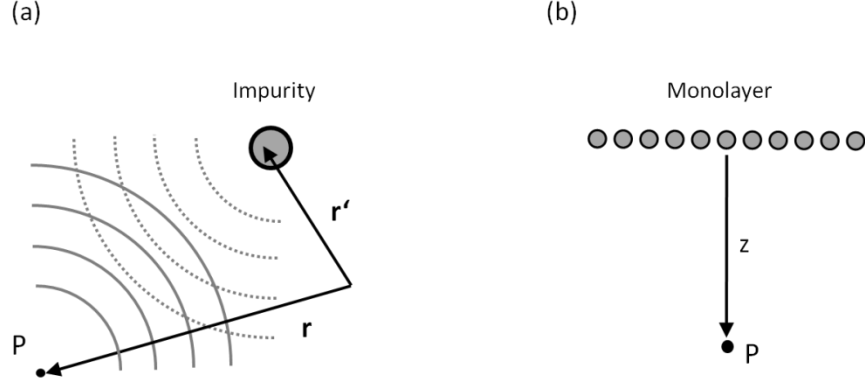


**Figure 13:** Scheme, indicating the interference of electron waves emanated from  $P$  and scattered at the impurity leading to spatially varying electron density (a). A monolayer of magnetic atoms at a distance  $z$  from point  $P$  is shown in (b). The scheme is related to that of the derivation in reference [32].

The oscillating nature of  $\chi_0$  is determined by  $k_F$  and expresses the formation of standing waves from the interference with scattered waves (Fig. 13a), thus resulting in a spatially varying electron density. By the integration of (3.1), the situation can be transferred to the case of a plane monolayer of magnetic atoms perpendicular to  $z$  (Fig. 13b). With evenly distributed scattering centers and  $V(\mathbf{r}')$  replaced by  $V\delta(z)'$ , the spatial variation of the free-electron density is

$$\chi_2(z) = \frac{4mk_F^2}{\hbar^2(2\pi)^2} \int_{2k_F z}^{\infty} \frac{u \cos u - \sin u}{u^3} du. \quad (3.4)$$

With  $u = 2k_F r'$  and for  $2k_F z \gg 1$ , it applies

$$\chi_2(z) = -\frac{m}{\hbar^2(2\pi)^2} \frac{\sin(2k_F z)}{z^2}. \quad (3.5)$$

The coupling strength which is proportional to  $\chi_2(z)$  is thus proportional to the inverse square of the distance  $z$  to the monolayer. In the following, the scattering potentials are examined, which are supposed to be spin-dependent, since the 3d-band structure of magnetic transition metals is different for both spin directions. The d-bands of elements residing left of the respective magnetic element in the periodic table resemble the minority d-band (indicated with “-”) which intersects the Fermi level. The majority band (+), on the other hand defers. Consequently, minority carriers are scattered less and the spin asymmetry becomes  $\alpha = \rho^-/\rho^+ < 1$ . The scattering potential can be assessed by

$$V^- \cong V_a \quad (3.6a)$$

$$V^+ \cong V_a + v_m M_s \quad (3.6b)$$

with  $M_s$  describing the saturation magnetization. Contrarily, for elements on the right of the element in the periodic table, it holds with  $\alpha > 1$ :

$$V^+ \cong V_a \quad (3.7c)$$

$$V^- \cong V_a + v_m M_s. \quad (3.7d)$$

Based on (3.1), the derived spin-dependent scattering potentials will influence the respective electron densities. The spatial variations in the electron densities in the ferromagnetic monolayer as well as in the differences between them are related following:

$$\Delta n(z) = \Delta n^+(z) + \Delta n^-(z) = \chi_2(z)V_a \quad (3.8a)$$

$$|\mathbf{j}(z)| = \Delta n^+(z) - \Delta n^-(z) = -\chi_2(z)v_m M_s . \quad (3.8b)$$

Thereby  $|\mathbf{j}|$  is the magnetic polarization in the nonmagnetic medium induced by the magnetic medium (declared in Bohr magnetons). Here, the susceptibility  $\chi_2$  completely covers the magnetization distribution in the nonmagnetic medium. In order to close the gap to the RKKY coupling, a magnetic atom is assumed to be located in the nonmagnetic medium at  $P$ , a distance  $z$  away from the monolayer. The coupling energy is then given by

$$\Delta E = \int (V^+(\mathbf{r}')n^+(z') + V^-(\mathbf{r}')n^-(z'))d\mathbf{r}' - \int 2V_a(\mathbf{r}')n_0 d\mathbf{r}'. \quad (3.9)$$

With (3.6), (3.7) and  $\Delta n^{\pm} = n^{\pm} - n_0$ , in which  $n_0$  exhibits the free electron density for each spin channel, the coupling energy becomes

$$\Delta E = \int (V_a(\mathbf{r}')\Delta n(z') - v_m(\mathbf{r}')\mathbf{j}(\mathbf{r}') \cdot \mathbf{j}_1(z'))d\mathbf{r}'. \quad (3.10)$$

The first term of (3.10) describes the chemical interaction and the second one the magnetic exchange energy, which can also be expressed as

$$\Delta E_{bil} = \mathbf{m} \cdot \mathbf{M}_1 \int v_m(\mathbf{r}')\chi_2(z')v_m d\mathbf{r}', \quad (3.11)$$

with  $\mathbf{m}$  being the magnetic moment of the impurity in  $P$ . Considering the lateral translation invariance, one obtains the interlayer exchange energy density between two parallel magnetic monolayers separated by a nonmagnetic medium with thickness  $d$ . When taking the potentials for both spin directions of the other magnetic layer distributed evenly in the lateral dimension, the *bilinear* exchange energy density follows from the integration to

$$\Delta E_{bil} = C\chi_2(d)\mathbf{M}_1 \cdot \mathbf{M}_2 = -J_{bil}\hat{\mathbf{i}}_1 \cdot \hat{\mathbf{i}}_2 , \quad (3.12)$$

where  $\mathbf{M}_1$  and  $\mathbf{M}_2$  are saturation magnetizations of both monolayers with respective unit vectors  $\hat{\mathbf{i}}_1$  and  $\hat{\mathbf{i}}_2$ . Like  $\chi_2$ , the bilinear coupling constant  $J_{bil}$  oscillates as a function of  $d$ . In other words, this means that the first monolayer probes the spatially varying electron densities of both spin directions that are induced by the second monolayer. The oscillation period  $\lambda$  that comes out of this model is equal to  $\pi/k_F$  and amounts to values comparable to the lattice plane distance of the spacer ( $\sim 3 \text{ \AA}$ ). However, the observed periods are much longer, namely approximately in the range of  $10 \text{ \AA}$ . This deviation in the period lengths comes from neglecting the crystalline discreteness of the spacer material. Since  $\chi_2$  consequently also takes discrete values, the electron density is only probed at the positions of the lattice planes. The *aliasing* approach which introduces the shape of the Fermi surface accounts for this. As *Fermi* surfaces of crystalline matter are actually non-spherical, the wave number  $k_F$  as well as the oscillation period depend on the crystallographic orientation [37, 38]. For the common metal spacers with [100] orientation, there is usually more than one period observed (see Fig. 14b). Assuming an elliptical *Fermi* surface (Fig. 14a) with stack normal  $\hat{\mathbf{i}}_z$ , there is only one direction with wave vectors  $k_F$  and  $k_{F'}$  for which  $\mathbf{Q} = \hat{\mathbf{i}}_z - k_{F'}$  is parallel to the layer normal with opposing group velocities  $\mathbf{V}_G$  and  $\mathbf{V}_{G'}$ . The *Fermi* surface indicated in

(Fig. 14b) is typical for cubic lattices and possesses two extremal distances describing two independent periods for which the above condition holds. The variables  $Q_1$  and  $Q_2$  denote the respective short and long period. By this means, the interlayer coupling oscillation periods can be estimated satisfactorily. Actually, a contribution from both oscillation periods is concerned, whereas in real multilayers the situation is complicated by interfacial roughness.

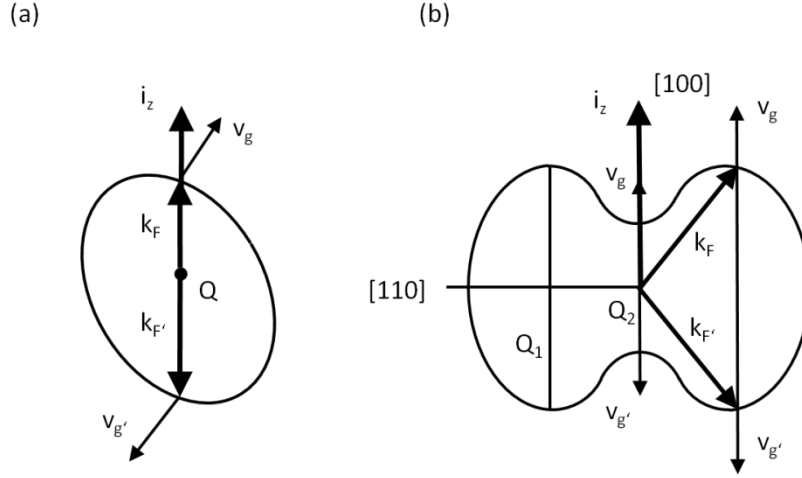


**Figure 14: Scheme of an elliptical Fermi surface (a) and the “dog bone” Fermi surface (b) with indicated Fermi wave vectors. The interlayer coupling oscillation period depends on the extremal distances. The scheme is related to that of the derivation in ref. [32].**

Obviously, in general the drawn picture cannot describe the coupling strength quantitatively due to the over-simplified introduction of scattering potentials in (3.6). A resort would be given by *first-principles* calculations of the total energy. However, such methods lack the required accuracy of energy differences, which are small as compared to the total energy. Furthermore, those calculations are generally restricted to low spacer thicknesses. Bruno et al. [38, 39] gave a detailed modification of the RKKY-interaction in order to explain the interlayer coupling. Though the oscillation periods predicted by this model coincide well with experimental findings [32], it is unable to correctly describe intensity and phase of the oscillations. Therefore, *first-principles* calculations are necessary that apply e.g. *tight-binding* approaches like conducted for instance by Mathon et al. [40]. The authors calculated the amplitude of exchange coupling in Co/Cu/Co tri-layers using these fully numerical methods.

### 3.1.2 Quantum interference model

Relying on [41], a brief outline of the interlayer coupling by means of a quantum interference model is given. It is referred to Bruno et al. [42] for a comprehensive description. In particular the change in density of states (DOS) and energy of an electronic system confined by a potential well with discrete energies is discussed. Moreover, an electron with wave vector  $k_x = k^+$  moving in x-direction transverse to the layer structure is assumed (Fig. 15).

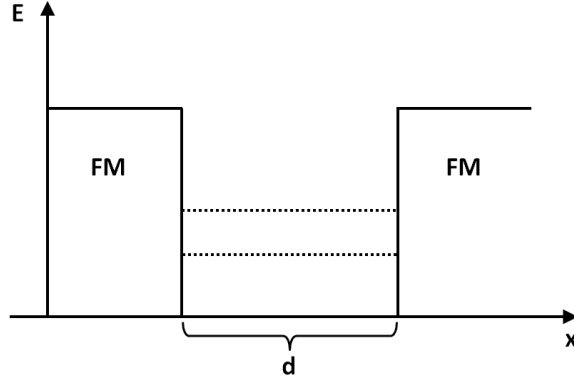


**Figure 15: Schematic quantum well structure of a tri-layer model system. The interlayer has thickness  $d$ . Dashed lines represent discrete energy states.**

When arriving - without loss of generality - at the left boundary, represented by a ferromagnetic layer, the electron will be reflected due to the potential step with coefficient  $r_L = |\mathbf{r}_L|e^{i\Phi_L}$ . Consequently, it propagates with wave vector  $k^-$  from left to right and is reflected according to  $r_R = |\mathbf{r}_R|e^{i\Phi_R}$ . Thereby  $|\mathbf{r}|$  and  $\Phi$  indicate amplitude and phase shift of the reflection. The interference of the electron waves propagating back and forth lead to a modification of the DOS in the interlayer. The phase shift of one cycle is given by

$$\Delta\Phi = (k^+ - k^-)d + \Phi_L + \Phi_R. \quad (3.13)$$

For constructive interference the following relation holds:

$$\Delta\Phi = \pm 2n\pi. \quad (3.14)$$

In this case the DOS is increased due to an increased probability density, while the other phase shifts are destructive and lead to a decreased DOS. Hence a DOS modification according to  $\cos(k^+ - k^-)d + \Phi_L + \Phi_R$  is expected. Furthermore the change should be proportional to the reflection amplitude  $|\mathbf{r}|$ , the interlayer thickness  $d$  and to the DOS per unit width and energy  $\frac{2}{\pi} \frac{d(k^+ - k^-)}{dE}$ , in which the number “2” originates from spin degeneracy. With respect to higher order interferences, accounted for by  $n$ , the change in DOS becomes:

$$\begin{aligned} \Delta n(E) &\cong d \frac{2}{\pi} \frac{d(k^+ - k^-)}{dE} \sum_{n=1}^{\infty} |\mathbf{r}_L|^n |\mathbf{r}_R|^n \cos[n((k^+ - k^-)d + \Phi_L + \Phi_R)] \\ &= \frac{2}{\pi} \text{Im} \left( id \frac{d(k^+ - k^-)}{dE} \sum_{n=1}^{\infty} (r_L r_R)^n e^{in(k^+ - k^-)d} \right) \\ &= \frac{2}{\pi} \text{Im} \left( i \frac{d(k^+ - k^-)}{dE} \frac{r_L r_R e^{i(k^+ - k^-)d}}{1 - r_L r_R e^{i(k^+ - k^-)d}} \right). \end{aligned} \quad (3.15)$$

Substituting the integrated DOS,  $\Delta N(E) = \int_{-\infty}^E \Delta n(E') dE'$  with the expression from (3.15) yields

$$\Delta N(E) = \frac{2}{\pi} \text{Im} \sum_{n=1}^{\infty} \frac{(r_L r_R)^n}{n} e^{in(k^+ - k^-)d} = -\frac{2}{\pi} \text{Im} \ln(1 - r_L r_R e^{i(k^+ - k^-)d}). \quad (3.16)$$

The imaginary part of the natural logarithm of a complex number is equal to its argument. Thus  $\Delta N(E)$  is determined by the argument of a point in the complex plane, which corresponds to an angle  $\Delta\Phi$  on a circle with radius  $|r_L r_R|$  around 1. In order to calculate the energy change of the electronic system due to quantum interferences, the potential of the grand-canonical ensemble is considered as follows:

$$\Psi \equiv -k_B T \int_{-\infty}^{\infty} \ln \left( 1 + e^{-\frac{E-E_F}{k_B T}} \right) D(E) dE = - \int_{-\infty}^{\infty} N(E) f(E) dE. \quad (3.17)$$

For  $T=0$ , the potential is simplified (due to the *Fermi*-distribution at  $T=0$ ) and given by

$$\Psi = \int_{-\infty}^{E_F} (E - E_F) D(E) dE = - \int_{-\infty}^{E_F} N(E) dE. \quad (3.18)$$

With (3.16) the total energy change in the interlayer as a consequence of quantum well formation becomes

$$\Delta E = \frac{2}{\pi} \text{Im} \int_{-\infty}^{\infty} \ln(1 - r_L r_R e^{i(k^+ - k^-)d}) dE. \quad (3.19)$$

For ferromagnetic boundaries the reflection coefficients  $r$  depends on the spin orientation of the electron with respect to the prevailing magnetization direction. This can be accounted for by potential steps of different heights, namely a higher one for electrons facing a boundary in which the magnetization opposes the spin and a lower one for electrons with the spin aligned parallel to the magnetization.

Although this model is widely accepted today and reasonable values for the oscillation periods can be extracted, it is oversimplified since the exact band structures are not considered. In addition, the model refers to only one dimension and a treatise in three spatial dimensions would complicate the situation in terms of the considered wave vectors. For the sake of simplicity, also the magnetic layer thicknesses are assumed infinite. For reasonable thicknesses in real multilayers, there will be transmission and further reflection of electron waves at adjacent interfaces. Consequently, interference and coupling strength will depend also on the magnetic layer thickness, as has been predicted [43] and verified experimentally [44]. Further investigation of the exchange coupling in magnetic multilayers in terms of reflection and transmission coefficients at interfaces has been carried out by Stiles et al. [45].

Fig. 16 gives an experimental verification of the interlayer coupling. The GMR amplitude (a) and corresponding saturation field (b) of two material systems (NiFe/Cu and CoFe/Cu) are shown as a function of the spacer, i.e. Cu thickness. An oscillation of the GMR amplitude owing to the oscillatory interlayer exchange coupling is obvious in (a). From (b), one can see that due to an enhanced coupling, the corresponding saturation fields increase drastically, the thinner the spacer gets.

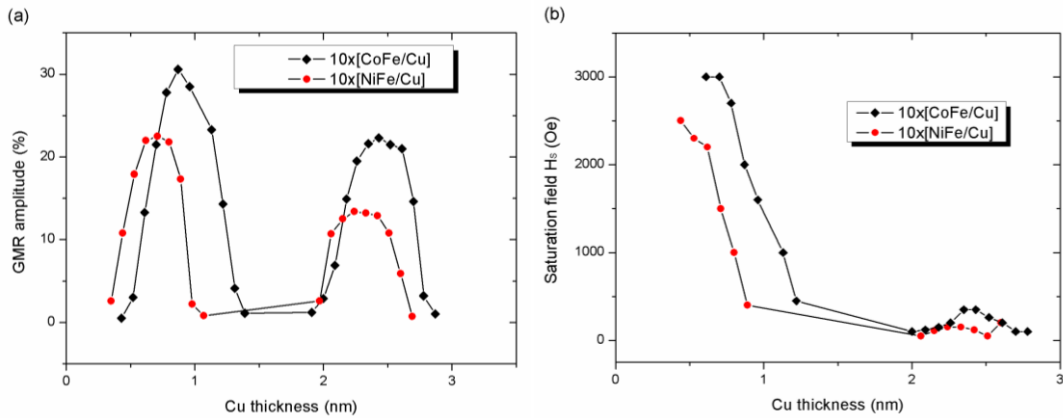


**Figure 16: Experimentally verified oscillation of the GMR as a consequence of the interlayer coupling. Amplitude (a) and corresponding saturation field (b) are shown as a function of spacer (Cu) thickness. The exact layer stacks are: MgO (4 nm) / 10x [CoFe(2 nm) / Cu(x)] / Ta(2 nm) and MgO (4 nm) / CoFe(2 nm) / 10x [Cu(x) / NiFe(3 nm)] / Ta(2 nm).**

### 3.2 GMR theory

In the previous section, so-called *biquadratic* coupling has been neglected (see formula 3.12). In the case that the respective coupling dominates compared to the bilinear one, an angle of  $90^\circ$  between magnetizations directions results, which is expected to originate from rough interfaces and magnetic impurities [46]. In the following, it is focused exclusively on magnetic multilayers with the current applied parallel to the layer plane, i.e. CIP (current in plane) geometry.

The origin of the GMR can be explained phenomenologically by spin-dependent carrier scattering at the ferromagnetic metals. Therefore, Mott [47] proposed a model that divides the current into a spin-up and a spin-down component. Assuming the channels to be independent and the spin orientation to be preserved in the majority of scattering processes, a high resistivity arises for AF aligned magnetizations (Fig. 17a) since both spin channels experience significant scattering. In the presence of an external field that aligns the magnetizations in the layers parallel, electrons with its spin aligned parallel to the respective magnetization direction get scattered less and the over-all resistivity decreases (see Fig. 17b). While actually bulk scattering plays a crucial role in alloys like NiFe [48], mostly interface scattering dominates as e.g. in genuine magnetic layers like Co.



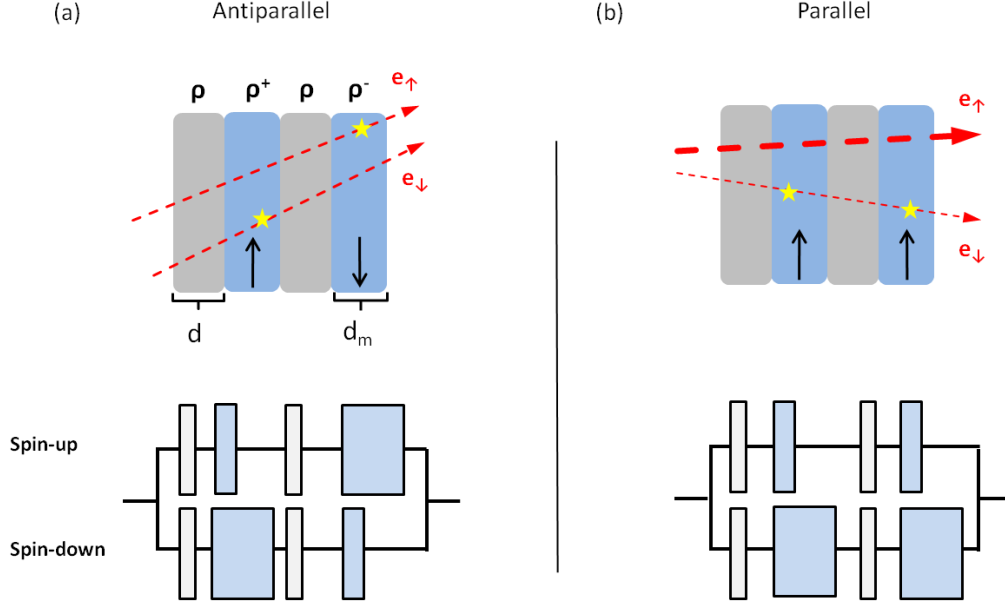


**Figure 17:** Schematic cross section of a multilayer with indicated spin dependent scattering at FM layers (top) with corresponding resistor network for spin-up and spin-down electrons (bottom). The situation for antiparallel (a) and parallel alignment (b) of magnetizations is shown. The stars indicate scattering events that lead to an over-all higher resistivity for the parallel case as denoted by the resistor widths.

Mott's two current model [49] is valid for moderate temperatures, at which spin-conserving defect scattering is predominant<sup>3</sup>. In contrast, probability of spin-flips increases with the temperature, since electrons collide with magnons and phonons which are generated to a larger extent.

The conductivity  $\sigma$  in this picture is composed of contributions from the majority as well as minority electrons. Derived from the *Drude* theory and according to [41], the conductivity becomes

$$\sigma^\pm = \frac{n_s e^2 \tau_s^\pm}{m_s^*} \quad (3.20)$$

where  $n_s$  and  $\tau_s$  denote density and relaxation time (time between two collisions) of 4s conduction electrons, respectively. As the quasi-free 4s-electrons are known to have a lower effective mass  $m_s^*$  than 3d electrons, they mainly carry the current. Majority electrons (spin-up) on the other hand, cannot occupy d-levels due to a filled 3d-band (compare Fig. 18a). Consequently mostly 4s<sup>+</sup> electrons contribute to the conductivity, and the resistivity

$$\rho^- = \rho_{ss}^- + \rho_{sd}^- \quad (3.21)$$

dominates. It reflects the sum of a contribution from 4s to 4s and from 4s to 3d states. The analogue holds for majority carriers. Assuming a negligible resistivity in the nonmagnetic interlayer, the total resistivity yields

$$\rho_p = \frac{2\rho^+\rho^-}{\rho^+\rho^-} \quad (3.22)$$

for parallel and

$$\rho_{ap} = \left( \frac{1}{\rho^+\rho^-} + \frac{1}{\rho^-\rho^+} \right)^{-1} = \frac{\rho^+\rho^-}{2} \quad (3.23)$$

<sup>3</sup> For 3d metals the spin-flip scattering cross section is 2 orders of magnitude smaller than that for spin conserving scattering [50].

for antiparallel magnetizations in the ferromagnetic layers. The latter term is obviously higher and with (3.22) and (3.23), the relative resistivity change following the definition of the GMR amplitude can be expressed as:

$$GMR = \frac{\rho_{ap} - \rho_p}{\rho_p} = \frac{(\rho^+ - \rho^-)^2}{4\rho^+ \rho^-}. \quad (3.24)$$

The second term suggests that the magnetoresistance is large, when the resistivities strongly depend on whether the spin orientation is parallel or antiparallel to the respective magnetization alignment in the layers. When taking into account the finite resistivity of the interlayer  $\rho$ , one obtains

$$R_p = \frac{(1+\gamma a)(1+\gamma b)}{2+\gamma a+\gamma b} \frac{2\rho d}{A}, \quad (3.25)$$

$$R_{ap} = (2 + \gamma a + \gamma b) \frac{\rho d}{2A} \quad (3.26)$$

and finally for the GMR amplitude

$$GMR = \frac{R_{ap} - R_p}{R_p} = \frac{(a-b)^2}{4(a+\gamma)(b+\gamma)}. \quad (3.27)$$

Variables  $A$ ,  $\gamma = d/d_m$ ,  $a = \rho^+/\rho$  and  $b = \rho^-/\rho$  denote cross-sectional area, the relation of interlayer and magnetic layer thickness and the given resistivity relations, respectively (see Fig. 17). In this rather simple scheme, there is obviously no correlation between the interlayer coupling and the GMR. Moreover it is pointed out that the conductivity is more properly described by the expression for thin films in the *Sondheimer* approximation. A more comprehensive solution is given by the semi-classical *Fuchs-Sondheimer* theory. It approaches the GMR based on (3.20) with *Fermi-Dirac*-distributed, free electrons and implies bulk as well as specular interface scattering [51]. However it is deficient for layer thicknesses smaller than the electron mean free path. In order to account for diffuse interface scattering, fully quantum mechanical approaches are required [52]. In the regard of a quantitative description of the GMR, the *Kubo* formalism<sup>4</sup> has been proven to be most successful. Due to a large number of parameters that are difficult to address experimentally, there is a great demand for analytical expressions of the GMR [54]. Furthermore, the model lacks for the explanation the GMR amplitude that depends on the wiring. In fact, for the current applied parallel or perpendicular to the layer structure, different current densities arise.

### 3.2.1 Intrinsic GMR

The next section enters into the intrinsic origin of the GMR that arises when a current is passed through a multilayer stack. The following derivation is based on the quasiclassical *Boltzmann* theory of transport and taken from ref. [41]. In the relaxation time approximation and with  $g(\mathbf{k}) = -e\tau(\partial f_0/\partial E)\mathbf{v}(\mathbf{k})\mathbf{E}$ , the current density becomes

$$\mathbf{J} = \frac{2}{V} \int e\mathbf{v}(\mathbf{k}) g(\mathbf{k}) d^3\mathbf{k} = \frac{2e^2\tau}{V} \sum_{\mathbf{k}} \mathbf{v}(\mathbf{k}) \mathbf{v}(\mathbf{k}) \mathbf{E} \left( -\frac{\partial f_0}{\partial E} \right), \quad (3.28)$$

---

<sup>4</sup> Method, evaluating the response of a quantum mechanical system to an external potential [50, 53].

with the stationary distribution function  $g(\mathbf{k})$ , the equilibrium *Fermi-Dirac* distribution  $f_0$  and  $\mathbf{v}$ ,  $\mathbf{k}$ ,  $\mathbf{E}$  and  $V$  being carrier velocity, wave vector, electric field and volume. The conductivity of the multilayer structure is a tensor and given by:

$$\hat{\sigma} = \frac{2e^2\tau}{V} \sum_{\mathbf{k}} \mathbf{v}(\mathbf{k}) \mathbf{v}(\mathbf{k}) \delta(E(\mathbf{k}) - E_F). \quad (3.29)$$

Due to the thermal energy being much larger than the *Fermi* energy ( $k_B T \ll E_F$ ),  $(-\partial f_0 / \partial E)$  can be approximated by  $\delta(E - E_F)$ . With neglected spin-flip scattering and (3.27), the GMR becomes:

$$GMR = \frac{\sum_{\mathbf{k}} \delta(E^+(\mathbf{k}) - E_F) v_{k_i}^{+2} + \sum_{\mathbf{k}} \delta(E^-(\mathbf{k}) - E_F) v_{k_i}^{-2}}{2 \sum_{\mathbf{k}} \delta(E^{ap}(\mathbf{k}) - E_F) v_{k_i}^{ap2}} - 1. \quad (3.30)$$

$v_{k_i}$  denote the Cartesian coordinates of *Fermi* velocities [55]. Since relaxation times have been assumed to be spin-independent, they cancel out and the GMR amplitude is designated by the intrinsic electronic structure. Substituting the density of states  $N(E_F) = \sum_{\mathbf{k}} \delta(E(\mathbf{k}) - E_F)$  and with the square of the respective velocity components  $\langle v_{k_i}^{+2} \rangle$  and  $\langle v_{k_i}^{-2} \rangle$  averaged over the Fermi surface, it applies

$$GMR = \frac{N^+(E_F) \langle v_{k_i}^{+2} \rangle + N^-(E_F) \langle v_{k_i}^{-2} \rangle}{2N^{ap}(E_F) \langle v_{k_i}^{ap,2} \rangle} - 1. \quad (3.31)$$

Thus, the GMR amplitude depends on the DOS of majorities and minorities at the *Fermi* level, their mean velocities as well as the corresponding total values in the case of antiparallel configuration. The findings of (3.31) are illustrated when looking at the 3d-band structure at the *Fermi* level. For ferromagnets, the DOS at the *Fermi* level is spin-polarized as a consequence of the *Pauli* principle. The scheme in Fig.18a indicates the situation for e.g. Co and Ni.

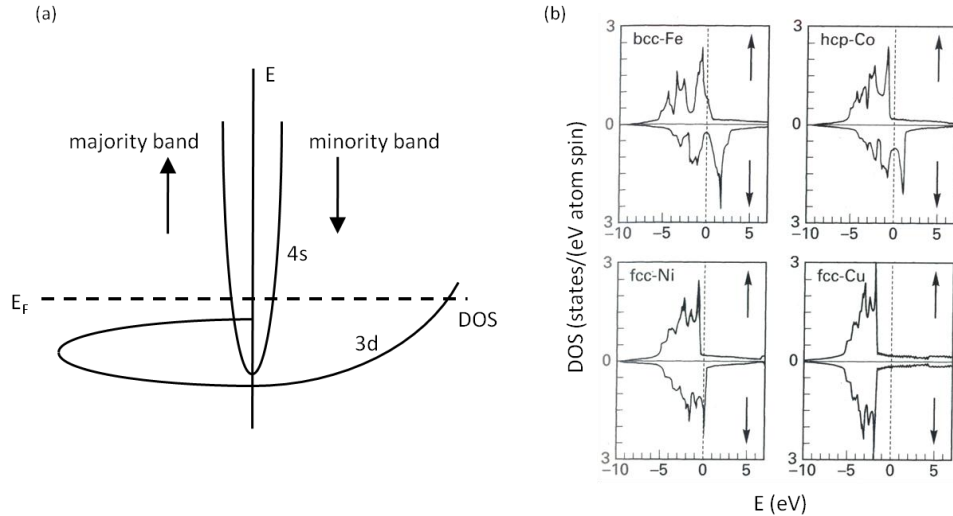


**Figure 18:** Schematic band structure as a function of DOS for ferromagnetic 3d metals (a). The arrows indicate the spin orientations. Spin-polarized DOS around  $E_F$  (dashed line) for Fe, Co, Ni and Cu obtained from self-consistent *ab initio* band structure calculations (taken from [56]) are shown in (b).

Though mainly free-electron-like s-states with energies close to  $E_F$  contribute to the electrical conductivity, the scattering as the origin of resistivity is expected to occur into d-states which possess a larger effective mass. The majority band (spin-up) contains electrons with spin parallel to the spontaneous

magnetization and lies completely below  $E_F$ . Minority electrons (spin-down), on the other hand, possess a large number of states, into which the carriers are scattered. Consequently, the scattering is high for spin-down electrons in the minority band and lower for those with spin-up. Despite of simplifications, i.e. the neglect of hybridization, the scheme is useful for the understanding of the basic mechanisms. Fig. 18b shows the *ab initio* calculated band structure of Fe, Co, Ni and Cu. A good electronic band match of spin up electrons for Co and Cu and a dissimilar one for electrons with spin down is striking. Thus, due to the resulting potential steps, which predominantly the minority electrons face at the interlayer, the *Fermi* velocities of majority electrons are larger than those of minority electrons. If one compares the in- and out-of-plane components of the velocities, it is even possible to explain the differences that arise between CIP and CPP (current perpendicular to plane) geometry. In section 3.2, it has already been entered into the extrinsic aspects of the GMR, i.e. the spin dependent scattering at impurities as a consequence of non-ideal interfaces (see also Fig. 17). Besides electronically well matched layers, also a good structural match and a high layer quality is important, since a lattice mismatch induces dislocations that might cause spin-flip-scattering.

In the case of Fe/Cr system, the Cr modifies the band structure of Fe - which is intrinsically a weak ferromagnet - in such a way, that a high DOS is generated (“virtual bound states”). The highest GMR values obtained equal ~220 % [57] for Fe/Cr and ~120 % [58] for Co/Cu at temperatures of 4.2 K.

## 4 Processing

According to the intended concept (section 1.2), the GMR sensor layers have to be deposited first. For samples coated with Zn and Ge NWs (the synthesis of which is described in sections 4.2.1.1 and 4.2.1.2), there have been attempts to deposit the sensor layers on top of the NW structures. After establishing electrical contacts to the NW arrays (outlined in section 5), it turned out that in case of Ge and owing to the wire density (see Fig. 38d), the non-continuity of sensor layers causes the electrical resistance to increase to ~1 M $\Omega$  and completely deteriorates the GMR properties. For the Zn sample, shunting occurred and led to a drastic decrease and distortion of the GMR signal.

Consequently, the processing of devices in this work is performed according to the workflow shown in Fig. 19, which depicts schematically the processing sequence. Unless otherwise stated, an insulating layer of magnesium oxide (MgO) is deposited on top of the GMR stack to avoid current shunting caused by subsequent coating. Prior to the NW synthesis, a thin metal is deposited which serves either as seed or catalyst. In case of the polymeric structures (see section 4.2.3), the metal solely ensures sufficient electrical conduction. The passivation and seed/catalyst metal deposition is confined to an area smaller than the GMR stack in order to leave a free area for electrical sensor contacts (confinement realised by shadow masks and *Kapton*<sup>5</sup> tape).

---

<sup>5</sup> Vacuum-proof adhesive tape.

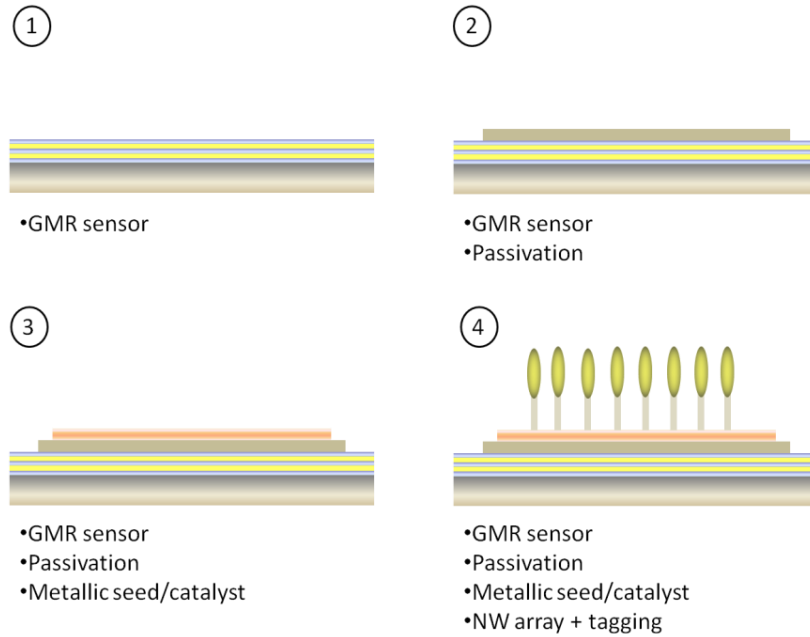


**Figure 19: Schematic of the device processing sequence.**

Originally, Si and Ge NWs (treated in section 4.2.2) were intended for the concept. For the catalytic reactions and diffusion processes involved in the NW self-assembly, usually high growth temperatures (>400 °C) are required. However, it is known that GMR multilayers deteriorate in performance already at comparably low temperatures of ~250 °C [59]. Annealing results for our GMR samples are summarized in table 1 (samples annealed under high vacuum conditions on a ceramic heating plate of pyrolytic graphite, temperature controlled with a type K thermocouple, see section 4.2.1.2). In order to maintain the magnetic properties of the GMR sensor stack during post-processing, the respective temperature dependence is investigated. It is obvious that a loss in GMR signal sets in around 300 °C annealing temperature, but manifest stronger for the CoFe/Cu system. One could speculate that this is due to an increased contribution of bulk scattering in the case of NiFe [48]. The thermal reduction of the GMR amplitude is generally related to slight material intermixing and “dead layer” formation at the interfaces leading to a decrease of spin dependent scattering [60, 32]. Due to the temperature sensitivity of the GMR sensor, it is necessary to deposit NW structures at low temperatures.

**Table 1: As-deposited and annealed GMR amplitudes (of 2<sup>nd</sup> antiferromagnetic maximum) summarized for different annealing temperatures and multilayer systems. The material indications refer to 10-fold multilayers.**

	As-dep. GMR (%)	Annealed GMR (%)	Annealing T (°C)	Annealing t (min)
NiFe/Cu	12.5	12.5	250	30
NiFe/Cu	12.5	9.2	300	35
NiFe/Cu	10.8	7.5	300	35
NiFe/Cu	12.9	8.3	325	35
CoFe/Cu	18.9	1.9	350	35
CoFe/Cu	18.2	1.4	300	35

## 4.1 GMR-sensors

In the present work, planar Ni<sub>79</sub>Fe<sub>21</sub>/Cu multilayers in the second antiferromagnetic coupling maximum are utilized as magnetic field sensors. In particular, the following system is sputter-deposited on silicon wafers<sup>6</sup> (CZ, Ø 100 mm, p-doped (boron), (100) or (111) orientation) with native or 50 nm thermal oxide:

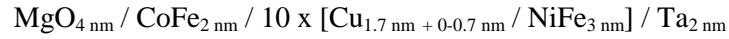


Table 2 displays sputtering modes, e.g. pre-sputtering time and source power for the individual layers. Owing to a larger spatial homogeneity of the GMR-amplitude as well as sensitivity all over the wafer, the Cu interlayer is processed in two steps (1.7 nm static and 0 - 0.7 nm in dynamic mode).

**Table 2: Multilayer sputtering parameters.**

Material	Source	Power (W)	t <sub>presputtering</sub> (s)	Mode	Deposition rate (nm/s)
MgO	RF	150	120	static	0,027
CoFe	DC	20	120	static	0,045
Cu	DC	40	60	static	0,265
Cu	DC	40	60	dynamic	
NiFe	DC	20	60	static	0,06
:	:	:	:	:	:
Ta	DC	20	120	static	0,067

This system excels in good sensitivity to small magnetic fields and hysteresis-free characteristics due to the vanishing crystalline anisotropy of NiFe [61]. The GMR amplitude is defined as:

$$GMR = \frac{R_{ap}-R_p}{R_p} 100 \% \quad (4.1)$$

<sup>6</sup> The wafers are directly loaded into the sputtering machine without any further cleaning.

Amplitude values of 13.3 % and sensitivities of about 0.33 % / Oe are obtained in the as-deposited state (see Fig. 20). The working point is set to zero lateral bias-field in order to avoid unintended sensor saturation as well as partial compensation effects owing to the radially symmetric in-plane components of stray fields of the magnetic tagging layer magnetized perpendicular to the sensor plane (see chapter 4.3). Unless stated otherwise, the GMR substrates are cleaned by soft ultrasonication in acetone and isopropanol prior to the synthesis.

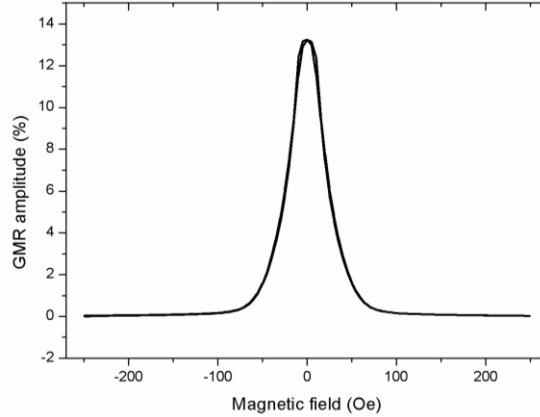


Figure 20: As-deposited GMR response curve.

## 4.2 Nanowire synthesis

One-dimensional (1D) nanostructures like NWs, nanotubes or nanobelts gain ever increasing importance as promising building blocks for the development of novel devices at the nanoscale [62]. Among all growth techniques, those employing vapor transport methods and Vapor-Liquid-Solid (VLS) [63] or Vapor-Solid [64] (VS) growth processes have been proven to be most promising and versatile regarding the composition and morphology. Many different materials including elemental and compound semiconductors, oxides, carbides, and nitrides were successfully synthesized utilizing such growth techniques. The formation process is thereby guided by the chemical potential. It is defined as the change in *Gibbs* free energy with the particle number:

$$\mu = \left( \frac{\partial G}{\partial n} \right)_{T,p} . \quad (4.2)$$

Deferring chemical potentials of two parts of a system lead to mass transport towards the system with the lower chemical potential in order to lower the free energy of the whole system. Hence, for the NW formation following the VS or VLS process,  $\mu$  has to be lowest for the respective solid phase. Therefore, the state of supersaturation exhibits a prerequisite. When regarding the free energy change per unit volume

$$\Delta G_V = - \frac{k_B T}{\Omega} \ln \frac{p_V}{p_S} \quad (4.3)$$

with temperature  $T$  and atomic volume  $\Omega$ , supersaturation is guaranteed for a vapor pressure  $p_V$  bigger than  $p_S$ . However the situation is simplified, since it only holds in case of thermodynamic equilibrium, which is often not fulfilled.

This chapter describes successively the synthesis and implementation of various NW designs, namely zinc, germanium and polymeric polypyrrole (PPy) that are foreseen as artificial cilia. While the first three subsections deal with self-assembly<sup>7</sup> processes, NWs synthesized by e-beam lithography (EBL) are introduced in chapter 4.2.4.

### 4.2.1 Zinc nanowires

In this section, we present a cold-wall physical vapor deposition (CWPVD) approach for the synthesis of metallic Zn NWs. At first a motivation for the research on metallic NWs is given followed by a detailed description of the setup.

Metal NWs, which are considered as possible interconnects or functional elements in future nanodevices, need to be synthesized by methods beyond the self-assembly owing to the lack of applicable catalyst materials. First metal NWs which showed conductance quantization and ballistic transport were fabricated by mechanical methods [65, 66], for example by vertical pulling of scanning tunneling microscope tips after point contact [65]. Metal NWs were also fabricated by electrochemical thinning of microscale wires [67] and electrodeposition [68] into templates of nanoporous materials [69] (e.g. porous anodic alumina, track-etched polycarbonate, mesoporous silica, etc.). The resulting nanocomposites have well-defined geometries preset by the pore dimensions and granular, polycrystalline or amorphous structures. Recently, single-crystalline NWs were demonstrated utilizing pulsed electrodeposition [70]. Electrochemical methods produce low yields due to the small template sizes. Post-synthesis device assembly requires removal of the nanoporous membrane which may cause damage to the NWs. Finally, metal NWs have also been demonstrated by step edge decoration [71] and solution phase methods [72]. Zn nanocomposites have recently shown unique thermoelectric and superconducting properties such as a very high room temperature *Seebeck* coefficient [73] ( $-130 \mu\text{V/K}$ ) and a novel antiproximity effect in a system of electrodeposited Zn NW arrays sandwiched between superconducting bulk electrodes [68]. Few groups focus actually on the synthesis of elemental Zn NWs by utilizing vapor transport methods. Whereas the Zn NWs introduced here feature unidirectional morphologies as well as much lower growth temperatures. Vivekchand et al. [74] e.g. utilized a nebulized spray pyrolysis technique to synthesize wool-like Zn NWs (see Fig. 21) by decomposition of Zn acetates at temperatures of 800-1000 °C.

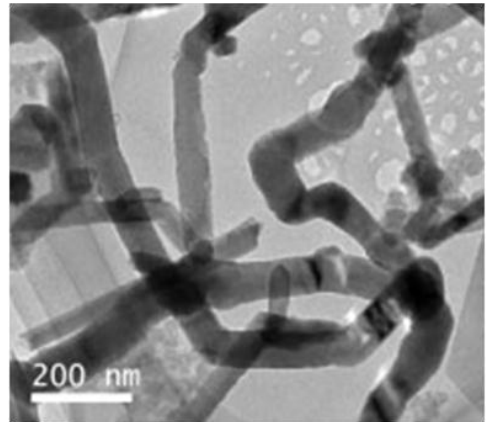


**Figure 21: Wool-like Zn NW morphology by TEM taken from [74].**

Kar et al. [75] synthesized similar structures by thermal evaporation of ZnS powders at 1225 °C. Besides the formation of ZnS nanoribbons, they also found wool-like Zn NWs in the cooler region of the quartz tube (~350 °C). Synthesis of Zn NWs was also demonstrated by carbo-thermal reduction of ZnO with graphite at temperatures of 1100 °C [76] and 1060 °C [77]. Zn NWs were obtained by thermal evaporation of pure Zn at temperatures of 580 °C [78], 600 °C [79] and 900 °C [80], respectively. The reported Zn NWs grow only in a wool-like morphology and are exclusively found in the cooler regions of

<sup>7</sup> Process controlled by the ambience or an external system, in which the assembly grows spontaneously.



the quartz tubes in an estimated temperature range of 200-350 °C. It is apparent, that the growth temperature in externally heated tube furnaces is strongly coupled to the sublimation temperature of the solid precursor materials. This coupling limits the parameter settings for the NW synthesis. Therefore, a CWPVD chamber, in which the substrate temperature is controlled independently from the Zn vapor source is set up. The underlying growth follows the VS principle, in which crystallization along one direction is guided by anisotropy of crystal surface energies. During the growth process, the morphology of the NWs strongly depends on the complex interplay of the relevant parameters (ambient pressure, substrate temperature, etc.), which control the kinetics of precursor atoms on the substrate surface and on the NWs. The chamber consists of standard vacuum parts (see Fig. 22). Elemental Zn (99.99%, Sigma-Aldrich) is thermally evaporated from an alumina crucible by resistive heating in high vacuum conditions. The sample is mounted on a distant heater facing down to the precursor vapor source. The temperature of the sample heater is measured by a type K thermocouple. A quartz microbalance (QMB) is used to monitor the Zn deposition rate and the nominal film thickness. The Zn atom flux to the substrate can be blanked by a mechanical shutter.

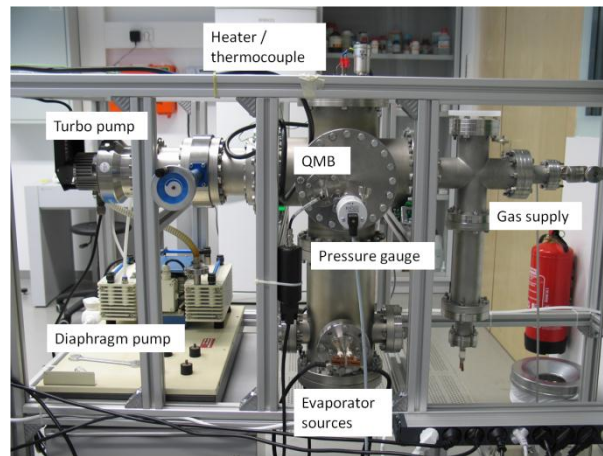


**Figure 22: CWPVD-chamber composed of standard vacuum parts.**

As substrates, as-deposited silicon wafers are cut into pieces of 20 mm x 20 mm and sputter coated with island-like gold (Au) or platinum (Pt) films (~3 nm). After the sample is mounted on the heater, the growth chamber is evacuated to base pressures of  $\sim 5 \times 10^{-7}$  mbar. Subsequently, the work pressure is set within a range of  $10^{-6}$ - $10^{-5}$  mbar by introducing oxygen or argon gas into the growth chamber. The Zn evaporation rate is usually set to 0.1 nm/s and the temperature is set to the growth temperature.

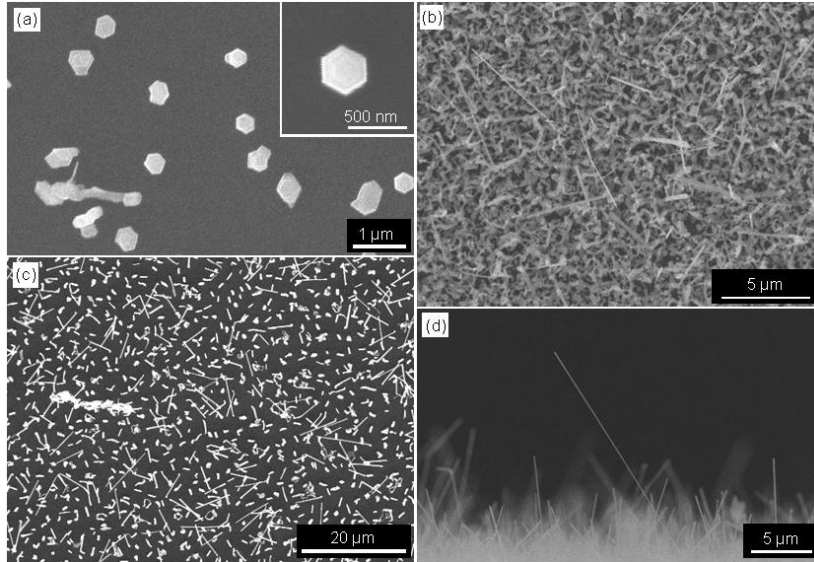


**Figure 23: Top-view SEM image of Zn nanocrystals grown on bare silicon (a). The inset shows a SEM image of an individual hexagonal Zn nanocrystal. Top-view SEM image of wool-like and rod-like NWs grown on gold covered substrate surfaces at  $T=150\text{ }^{\circ}\text{C}$  (b). Top-view SEM image of 1D NWs grown on a platinum coated substrate at  $T_s=150\text{ }^{\circ}\text{C}$  (c). Representative side-view SEM image of unidirectional NWs grown on the edges of gold or platinum coated substrates (d).**

Fig. 23a shows a SEM image of Zn nanostructures grown on bare silicon without any metal seeds. At a substrate temperature of  $T=150\text{ }^{\circ}\text{C}$ , the evaporated Zn nucleates on the silicon surface and crystallizes in the hexagonal closed-packed lattice structure assembling nanosized islands with the  $[0001]$  direction being perpendicular to the substrate surface. In contrast, bare Si substrates (the same holds for GMR substrates) covered with gold seeds exhibit NWs of two different morphologies, as shown in Fig.23b ( $T=150\text{ }^{\circ}\text{C}$ ). The dominating NWs have 1D wool-like and also termed zigzag or serpentine morphology, which have already been reported by other groups as mentioned above. In addition, rod-like NWs are also observed. A representative side view of NWs observed on the substrate surfaces and on the edges of the substrates is shown in Fig. 23d. The NWs have diameters in the range of 30-350 nm and are up to 89  $\mu\text{m}$  long. Fig. 23c shows NWs grown on the substrate initially coated with platinum instead of gold at  $T=150\text{ }^{\circ}\text{C}$ . In contrast to the nanostructures obtained on the gold covered substrate, the surface does not show any wool-like NWs. The dominating NWs show rodlike morphology, are homogeneously distributed, have uniform dimensions and enclose arbitrary angle with the substrate. Between the NWs, the surface seems to be free of Zn deposits indicating a high surface mobility of Zn adatoms. This observation is consistent with the growth on bare Si (Fig. 23a). Furthermore, the substrates with Pt exhibit larger interwire spacings compared to those with Au. AFM measurements of Au and Pt substrate surfaces prior to nanowire growth show similar high grain densities which imply that the density of Zn nanowires on the individual substrate surfaces does not relate to the density of metal seed (Pt or Au) islands or grains. In contrast, the metal seed layers (Pt or Au) modify the surface mobility of Zn on the Si substrate and hence result in different densities of critical Zn nuclei coalescing in the first stage of the NW growth. AFM measurements also revealed a much lower surface roughness of Pt substrates (compared to Au). Fig. 24 depicts a 2 nm Au (a) and 3 nm Pt (b) layer, sputter-deposited at 25 W on silicon by AFM. The root-mean-square (RMS) roughness of Au (1.93 nm) turned out to be almost one order of magnitude higher than that of Pt (0.18 nm).

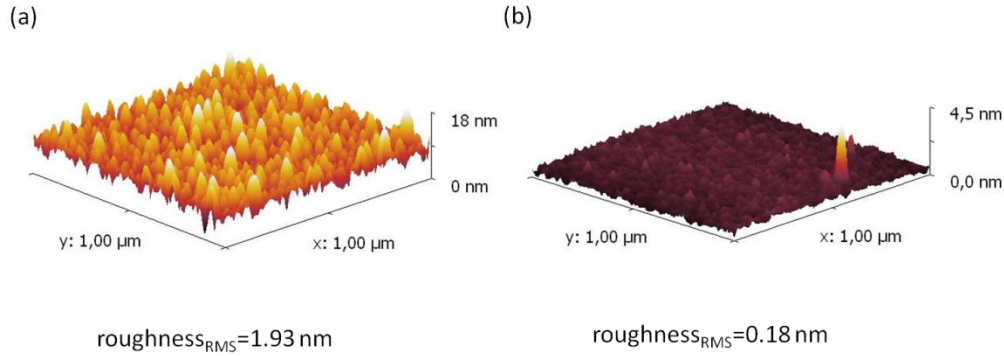


**Figure 24: Surface roughness of an as-deposited Au (a) and Pt (b) layer on a silicon (100) substrate with native oxide by AFM. The RMS roughnesses are indicated respectively.**

Increasing the surface roughness of Pt/Si by annealing the substrate prior to the growth for 3 min at 650 °C leads to the same results as obtained for Au/Si presented in Fig. 23b. Therefore, we do not attribute the suppression of wool-like NW to the nature of the platinum seed material. We find that growth of Zn nanowires on Si requires nanosized features which support Zn nucleation on the substrate surface. The density of Zn nuclei depends on the Zn adatom surface mobility which is influenced by the nanoscopic surface roughness. Therefore, smooth surfaces without pronounced nucleation sites favor the nucleation of homogeneous Zn nuclei which act as seeds for the growth of unidirectional NWs.

In order to obtain further insight into the NW growth, silicon substrates coated with 100 nm thick Au and Pt layers were also tested as substrates. After the individual growth runs, neither Zn grains nor Zn nanostructures could be observed on the metal surfaces. In addition, we evaporated Au layers exhibiting thickness gradients on silicon oxide using shadow masks. After the growth, NWs of rod- and wool-like morphologies are observed only in the areas where the Au coating becomes non-continuous and island-like. These formations of nanofeatures seem to act as nucleation sites. On continuous Au films, Zn does obviously not nucleate due to (i) the presence of metallic surface bonds which suppress surface diffusion in the first instance and (ii) probably alloy formation by bulk diffusion of Zn. On areas without Au we observe Zn nanocrystals similar to the structures shown in Fig. 23a. Zn island growth is favored due to the higher surface energy of Zn compared to SiO<sub>2</sub>.

At growth temperatures higher than 200 °C, Zn does not nucleate on any of the aforementioned substrates. After the standard growth time of one hour, the samples did not show any Zn deposits. A high Zn desorption rate at  $T \geq 200$  °C dominates surface diffusion and hence impedes Zn nucleation on the sample surface. At this point it is important to note that the morphologies of the Zn nanostructures grown by CWPVD do not depend on the type of gas used during the individual growth runs.

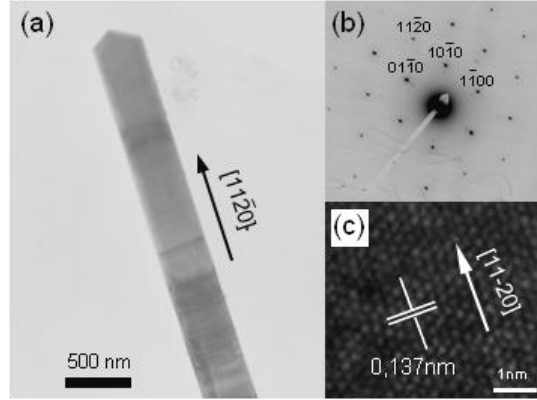


**Figure 25:** Low magnification TEM image of NW tip showing two distinct facets including an angle of  $120^\circ$  (a). Diffraction pattern of a single-crystalline Zn NW (b) and high resolution TEM image of a single Zn NW (c) are shown. Lattice plane distance of 0.137 nm determines the growth direction to [11-20].

EDX measurements have proven that all nanostructures grown consist of pure Zn. Fig. 25a shows a low magnification TEM image of an individual NW of rodlike morphology harvested from the substrate surface after an ultrasonic treatment and dispersed onto a copper grid. The NW tip shows two distinct facets including an angle of  $120^\circ$ . The diffraction pattern shown in Fig.25b reveals a single crystalline phase. Fig.25c shows a HRTEM image of the Zn lattice planes perpendicular to the growth direction. From the lattice plane distance of 0.137 nm, we deduce the growth direction to be [11-20]. This growth direction was determined on all NWs studied, independent of the seed material. Fig.26a shows a HRTEM image of the NW sidewall. The dark area depicts the core of the NW consisting of single-crystalline Zn covered with a 2 nm thick native oxide (dark-gray). The HRTEM image shown in Fig. 26b reveals the single-crystallinity of the surface oxide.

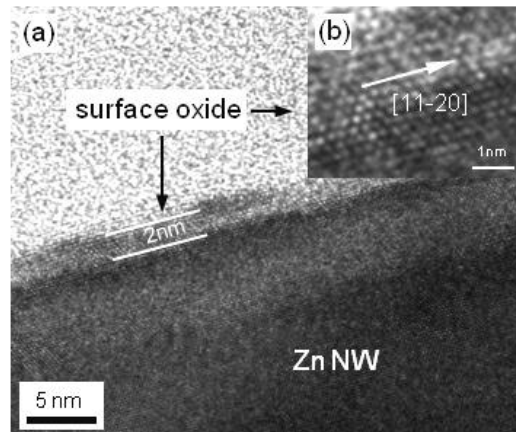


**Figure 26:** High resolution TEM image of a Zn NW sidewall covered with a 2 nm thick surface oxide (a). High resolution TEM image of single-crystalline surface oxide is shown in (b).

Since no catalyst particles are present on the tips of the NWs, it is evident that the synthesis proceeds via the VS growth process. At first, precursor atoms nucleate on the substrate surface forming nanocrystallites. The according free energy change for heterogeneous nucleation applies to:

$$\Delta G = A r^3 \Delta G_V + B r^2 \gamma . \quad (4.4)$$

Thereby  $r$  depicts the radius of the nucleus,  $\gamma$  the surface energy density and  $A$  and  $B$  geometry constants. In a second stage, continuously adsorbing Zn adatoms migrate to the nanocrystallites being incorporated at positions having the lowest surface energies. When the nanocrystals form stable side facets, the crystallization is driven along one direction, i.e. [11-20] resulting in 1D (one-dimensional) NW growth. The ratio of the NW length growth rate to the precursor deposition rate is a first measure of the Zn adatom mobility on the NW. In our experiments, the highest NW length growth rate obtained from SEM analysis equals  $R_{NW} = 53.33$  nm/s which exceeds the deposition rate of  $R_{Zn} = 0.062$  nm/s by a factor of 860. This result gives direct evidence that the NWs are predominantly formed by surface diffusing Zn adatoms and that direct impingement of precursor atoms on the NW tip does not play a significant role during the growth process.

The Zn surface diffusion length on the NW sidewall is determined using the mass transport model presented by Seifert et al. [81] In this model, a liquid catalyst particle on the NW tip acts as a sink which creates the driving force for material flow from the substrate surface and the NW sidewalls towards the NW tip. Effective surface diffusion lengths on the substrate  $\lambda_s$  and along the nanowire  $\lambda_w$  are introduced which are obtained from studying the dependence of the NW length growth rate  $dL/dt$  on the NW radius  $r_w$ . In the late growth stage, where  $L \gg \lambda_w$  holds, the length growth rate is given by the simple equation

$$\frac{dL}{dt} = 2R \left( 1 + \frac{\lambda_w}{r_w} \right) \quad (4.5)$$

where  $R$  stands for the effective impingement rate of adatoms on the substrate surface, NW sidewalls and NW tips. The first term on the right side depicts the growth by direct impingement of precursor atoms on the NW tip. The second term depicts diffusion controlled growth. The main conclusion of this equation is that thinner NWs grow faster than thicker ones. In order to apply this mass transport model to VS growth of Zn NWs, the hemispherical liquid catalyst particle is replaced by the cone-shaped tip shown in Fig.25a. In contrast to the initial model, where the full NW shell is exposed to impinging atoms, only half of the NW shell is exposed to the highly directed precursor deposition flux, due to shadowing effects in high vacuum conditions. As a consequence the NW length growth rate results in

$$R_{NW} = R_{Zn} \left( 1.155 + \frac{\lambda_w}{r_w} \right). \quad (4.6)$$

Since the ratio  $R_{NW}/R_{Zn}$  exceeds values of 850 as mentioned above, the contribution of direct impingement on the NW tip is neglected and the equation can be reduced to

$$\lambda_w = \frac{R_{NW}}{R_{Zn}} r_w. \quad (4.7)$$

Since the growth of individual NWs starts randomly in time during one growth run, the NWs show a clear length distribution, as can be seen in Fig. 23d. As a consequence, the geometry of the longest NW observed by SEM ( $L=89$   $\mu$ m,  $r_w=100$  nm,  $t=60$  min) only allows to determine a lower limit of the effective surface diffusion length which results in

$$\lambda_w \geq 39 \mu\text{m}. \quad (4.8)$$

The surface diffusion length plays a crucial role in how the NW lateral size develops during the growth process. In diffusion controlled NW growth processes, tapering of the NW diameter occurs at NW

lengths exceeding the surface diffusion length [82]. Since most of the NWs do not exceed this length, as shown in Fig. 23c, no tapered NWs are observed by SEM. For the sensor device, silicon substrates are coated with GMR multilayers and 20 nm of MgO which serves for the electrical insulation.

#### 4.2.1.1 Post-synthesis oxidation of Zn nanowires

Although ZnO nanowires are never used in our sensor developments, the post-synthesis oxidation described in the following together with our CWPVD process could be a promising method for industrial ZnO NW fabrication at low temperatures. Zinc oxide (ZnO) as a low cost, biocompatible, and wide band gap semiconductor material plays a significant role in current sensor and energy harvesting technologies. Since nearly two decades, special attention has been paid to ZnO in order to assemble devices on the nanoscale and to study novel, size-induced physical properties. Hexagonal wurtzite ZnO NWs have been applied as field effect transistors [83], gas sensors, surface coatings [84] and solar cells [85]. The inherent oxygen vacancy states of ZnO cause a charge transfer and therefore a conductance change when molecules adsorb on the wire surfaces. The detection of NO<sub>2</sub>, NH<sub>3</sub>, O<sub>2</sub> or ethanol has been successfully demonstrated by ZnO-based nanosensors [86]. In 2001, Huang et al. [87] reported room-temperature, short-wavelength lasing emission of ZnO NWs where the hexagonal end facet act as reflecting mirrors for the cavity. Magnetically (Mn, Cu, Co) or electrically doped (Al, In, Ga) [88] zinc oxides are promising materials for applications in spintronics, solar cells (as transparent conductive oxides) and heat insulation glazings. Owing to the piezoelectricity of ZnO, its nanostructures are also utilized as nanogenerators [89], nanoforce sensors and piezoelectric FETs [90]. A huge variety of morphologies has been fabricated by different methods, such as rod-shaped NWs, nanobelts, nanorings and nanocages [91]. ZnO NWs have been produced by e.g. physical vapor deposition (PVD), e.g. sputter deposition [92], or metal organic chemical vapor deposition (MOCVD) [93]. Furthermore, ZnO NWs and dendritic structures exhibiting [0001] and  $[\frac{1}{3}\frac{1}{3}-20]$  growth direction have been fabricated without any metal catalysts by heating Zn powder [94] or nanocrystallites [95] to temperatures of 500-600 °C. Conley et al. succeeded in transforming atomic layer deposited ZnO into an assembly of ZnO NWs. The annealing at temperatures of 915 °C for 30 min results in the formation of the nanostructures [96]. In order to lower the growth temperature, controlled VLS-growth of ZnO NWs is obtained by carbo-thermal reduction. The precursor is then mixed with graphite which reduces the ZnO and generates Zn vapor [97]. In summary, the ZnO NW synthesis by PVD methods has been conducted at temperatures ranging from 400 °C [98] to 1100 °C [99].

The industrial synthesis of ZnO nanostructures demands for reproducibility and compatibility with standard device fabrication processes. Whereas the melting point at 1975 °C and the sublimation at ~1800 °C set the upper limit, practical limitation is given by the choice of substrate materials and compatibility with post-processing and semiconductor technology. Fabrication processes are required to work at lower temperatures. One possibility is the electrochemical approach, where the structures are grown into “nanochannels” of anodic alumina membranes [100] at low temperatures (<100 °C). However, the products often consist of polycrystalline material which deteriorates their mechanical and electrical properties. In recent years, the transformation of Zn NWs to ZnO NWs has been considered as a possible route to effectively reduce the temperature of ZnO NW synthesis. Since Zn NWs grow at temperatures as low as 150 °C, while significant oxidation of Zn sets in at temperatures of 300 °C [79], this approach appears to close the gap between standard CMOS technologies and ZnO NW synthesis. Kim et al. have

reported on the fabrication of coaxial Zn/ZnO nanocables and polycrystalline ZnO rods by post-synthesis annealing of Zn NWs [101]. In 2004, Vivekchand et al. studied oxidation of Zn NWs (produced by a “nebulized spray pyrolysis” technique) by annealing in air at 450 °C [74]. The resulting nanostructures exhibit tubular ZnO of wool-like morphology with dimensions comparable with the polycrystalline starting material (diameters: 50-100 nm). In 2005, Liu et al. [79] succeeded in converting Zn NWs into ZnO NWs by subsequent oxidation at moderate temperatures of 300 °C. The authors report that the morphologies of the NWs do not change significantly during the oxidation process, which can be perceived as diffusional mass flow. Based on a derivation of microscopic atom transport and *Ficks* phenomenological law<sup>8</sup> of diffusion, the mass flow (oxygen)  $J$  applies to

$$J = -\frac{1}{6}a^2\nu e^{-\frac{E_D}{k_B T}} \frac{dc}{dx} \quad (4.9)$$

with lattice constant  $a$ , lattice oscillation frequency  $\nu$ , diffusion activation energy  $E_D$  and the concentration gradient  $dc/dx$  [102]. The process is thus thermally driven whereas the middle term is described by the *Maxwell-Boltzmann*-distribution.

#### 4.2.1.2 Morphology alterations during oxidation

Next a study on morphology alterations of single-crystalline Zn NWs during post-synthesis oxidation in ambient air is presented. Unlike other groups that have mainly studied transformations of wool-like or serpentine Zn NWs, rod-shaped Zn NWs synthesized by CWPVD (see section 4.2.1) at 150 °C [103] are utilized. The samples are oxidized on a plate of boron nitride which is current-heated by a coil of pyrolytic graphite (see Fig.27). The temperature is monitored by a type K thermocouple. During a typical oxidation cycle the temperature of the heater is (i) ramped to the set-point at rates of  $\sim 1^\circ\text{C/s}$ , (ii) held at the oxidation temperature (200-500 °C) for 30 min and finally (iii) cooled down in air to room temperature. Fig. 28(a) and (b) show XRD patterns of samples oxidized at temperatures of 200-500 °C for 30 min in air. The prominent peaks at  $61.69^\circ$  and  $33^\circ$  originate from the silicon substrates. The former is the  $K_\beta$ -reflection of the (40-40) lattice planes and the latter is ascribed to the (0002) forbidden diffraction that can be induced by atomic displacements in the silicon crystal.

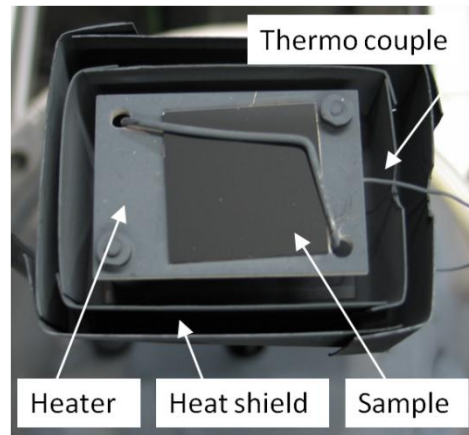


**Figure 27: Heat-shielded boron-nitride heater plate with mounted sample.**

The XRD pattern of the reference sample exhibits distinct diffraction peaks at Bragg angles of  $36.40^\circ$ ,  $39.11^\circ$ , and  $43.35^\circ$  which are attributed to the (0002), (10-10), and (10-11) lattice planes of crystalline Zn, respectively (Fig. 28a). The absence of additional diffraction peaks is ascribed to the rod-shaped morphology and the special growth direction of Zn NWs. Although Zn NWs are covered with a 2-4 nm thin native oxide [103], no ZnO-related diffraction peaks were observed. The XRD patterns of

<sup>8</sup> Relates the mass flow  $J$  to the concentration gradient  $dc/dx$  by the diffusion constant  $D$  according to  $J = -D \frac{dc}{dx}$ .

samples oxidized at 200 °C and 250 °C indicate that no significant oxidation occurs up to temperatures of 250 °C. Only the decrease in intensities of Zn-related diffraction peaks indicates the onset of Zn oxidation.

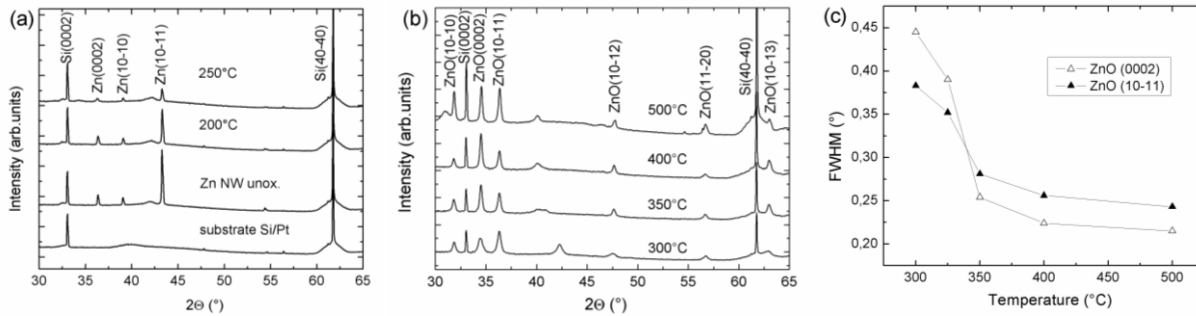


**Figure 28:** XRD patterns of samples oxidized at 200 °C, 250 °C and the reference (a). XRD analysis of samples oxidized at 300 °C, 350 °C, 400 °C and 500 °C (b). The diffractograms exclusively indicate ZnO crystallites. With increasing temperature the peak width decreases while the intensity increases. The XRD analysis of ZnO (0002) and (10-11) crystallites shows saturation in the FWHM with increasing temperature (c).

Fig. 28b shows XRD patterns of samples oxidized at temperatures between 300 °C and 500 °C. In contrast to the results presented (a), diffraction peaks at 31.8°, 34.5°, 36.3°, 47.6°, 56.7° and 63° are clearly evident which are attributed to the (10-10), (0002), (10-11), (10-12), (11-20), and (10-13) lattice planes of ZnO with lattice parameters of  $a=0.325$  nm and  $c=0.521$  nm [104]. Furthermore, no evidence for crystalline Zn was found in the diffractograms, which confirms - in agreement with the findings of Ref. 25 - that 300 °C are sufficient to oxidize Zn NWs to an extent where no elemental Zn is detected within the sensitivity of XRD analysis.

According to the *Scherrer* formula, the crystallite size is inversely proportional to the peak width, corrected for instrumental peak broadening. Therefore, the line widths extracted from the individual XRD patterns provide additional information about the Zn to ZnO transformation during the oxidation process. For all Zn diffraction peaks, a clear broadening of the line widths accompanied by a decrease in the corresponding peak intensities is observed, which clearly indicates the vanishing of the Zn phase. In contrast, a dramatic decrease in the line widths of selected ZnO diffraction peaks between 300 °C and 350 °C depicts different oxidation states of Zn/ZnO NWs (Fig. 28c). At temperatures  $\geq 350$  °C, the line widths and correspondingly ZnO grain growth obtain saturation, which confirms complete transformation of Zn to ZnO. Fig. 29 shows SEM images of Zn NWs oxidized at room temperature (a-c), 250 °C (d-f) and 350 °C (g-i), respectively. The individual rows depict top-view (left) and side-view images (middle) of the substrate surface as well as high-resolution SEM image of individual NW tips (right).



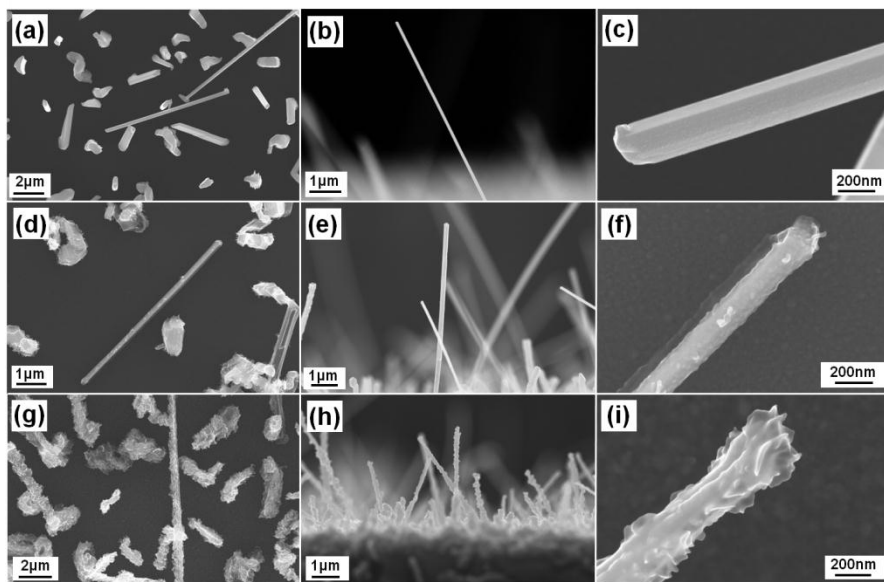


**Figure 29:** SEM image of the reference sample with Zn NWs oxidized at room temperature (a-c), at 250 °C (d-f) and at 350 °C (g-i). The structures of each row depict top-view (left), side-view (middle) and high resolution images (right). It can be seen that the morphologies are roughening with increasing temperature.

Selected-area electron diffraction (SAED) patterns revealed that the oxide grows in the same crystal direction as the Zn wire, whereas this growth is regarded as pseudomorphic up to a critical thickness, which is inversely proportional to the lattice mismatch and the distance between dislocations that compensate for misfit strain. Such a native oxide grows very rapidly by a first adsorption of an atomic oxygen layer on the surface and the formation of subsequent layers, whereas surface charge builds up by tunneling of electrons from the Zn metal through the growing oxide layer [105]. The resulting electric field across the oxide pulls metal ions through the oxide film until equilibrium is reached. In contrast to metals like e.g. Cu or Fe, the native oxidation rate of zinc drops off completely after the initial growth stage, wherefore ZnO is regarded as a protective oxide. The thickness of this protective oxide mainly depends on the temperature. It has been reported that the oxide thicknesses of Zn NWs annealed at 110 °C and 150 °C amount to about 7 nm and 10 nm [106]. Kim et al. [101] found that NWs of up to 120 nm in diameter oxidized at 200 °C form a polycrystalline oxide shell, approximately 15 nm in thickness.

Oxidation in air at 250 °C for 30 min leads to blurry outlines of individual Zn NWs and nanocrystallites as shown in Fig. 29d-f. Direct comparison of Figs. 29(c) and (f) reveals that the originally well-defined NW sidewalls undergo a morphology change driven by the elevated oxidation temperature. Since the corresponding XRD spectrum (Fig. 28a) does not show any evidence for a significant oxidation of the Zn nanostructures, we attribute this morphology change to the high surface mobility of Zn atoms on the NW sidewalls which impedes homogeneous oxidation of individual facets. Moreover, non-planar recrystallization of Zn atoms is supported by the inhomogeneous thickness of the native oxide covering the Zn NW prior to the oxidation process [103].

### 4.2.1.3 Discussion

It is known that with increasing temperature the oxidation of Zn further proceeds by the migration of metal ions that provide the necessary activation energy. This process satisfies the parabolic law [105] in which the oxide thickness is proportional to the square root of the oxidation time. Oxidation in air at 350 °C leads to an even more pronounced morphology change as shown in Fig. 29g-i. Although, the original geometries of NWs and crystallites are conserved, they exhibit a distinct surface roughness. Since an annealing of a NW sample with a rate of 5 °C/min to 350 °C lead to similar results, the temperature rising rate can be excluded as an important factor for the observed NW morphology changes. The mechanism of the morphology alteration can be understood by considering the dependence of the oxidation rates on the surface energies of individual crystal faces. Since the oxidation rates are directly proportional to the surface energies, the anisotropy of the Zn crystal results in different oxidation rates at the faces. Fig. 30 shows the transformation of serpentine Zn NWs into hollow ZnO nanotubes as reported by Lu et al. [106]. The conversion is ascribed to a quick oxidation of the Zn NW sidewalls followed by the sublimation of the Zn cores at the nanowire tips.

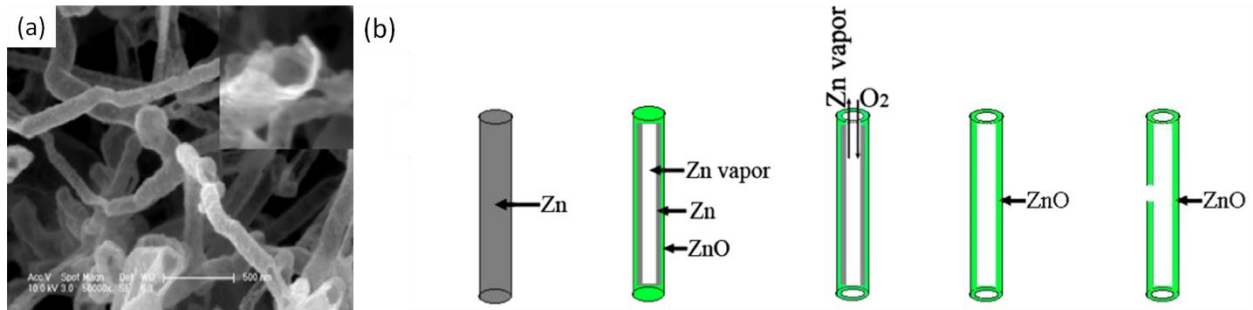


**Figure 30: Zn NWs with hatches at the ends (inset) by SEM (a). Schematic of the transformation into tubular ZnO nanostructures (b) taken from [106].**

This is because the end faces mainly represent stable, low-energy (0001) planes with lower oxidation rates than the sidewalls. Consequently, outbursts occur at the NW tips and the NWs are oxidized from the inside, thus forming nanotubes.

Since CWPVD-grown Zn NWs grow along the  $[\frac{1}{3}\frac{1}{3}20]$  direction, the NW sidewalls do not consist of equivalent lattice planes, like Zn NWs grown along the [0001] direction. Consequently sidewall faces of Zn NWs experience different oxidation rates according to their individual surface energies. The SEM image in Fig. 31 reveals that two opposing NW faces show bursts while the faces in between basically conserve its original shape after being oxidized at 350 °C. In Fig. 32 the concluded transformation mechanism with the corresponding crystal faces is illustrated schematically. The scheme is simplified as the NW cross section is not necessarily quadratic. Contrary to Fig. 32a, the NW in Fig. 32b shows starting, quick oxidation of the crystal faces of highest surface energies at 250 °C. Concurrently the Zn starts to sublime due to the high temperature. Thus the Zn vapor pressure increases until the ZnO shell bursts at its weakest positions, i.e. the lowest energy (0001)-face. Subsequently the oxidation over the whole NW is completed at ~300 °C like confirmed by XRD. From Fig. 32c it is obvious that the higher energy faces, which oxidize faster, serve as a backbone for the NWs and this way conserve the rod-like appearance. Due to the burst morphology and the absorbed oxygen, the NW diameters appear larger. A further temperature increase to 400 °C and 500 °C has no effect on the morphologies. However a color change can be observed by eye with increasing oxidation temperature. As shown in Fig. 33 the original grey color turns

yellow, when oxidizing a sample at 300 °C for 30 minutes while it appears blue when increasing the temperatures to 350 °C and 400 °C. The effect can be attributed to different oxygen deficiencies of the deposit.

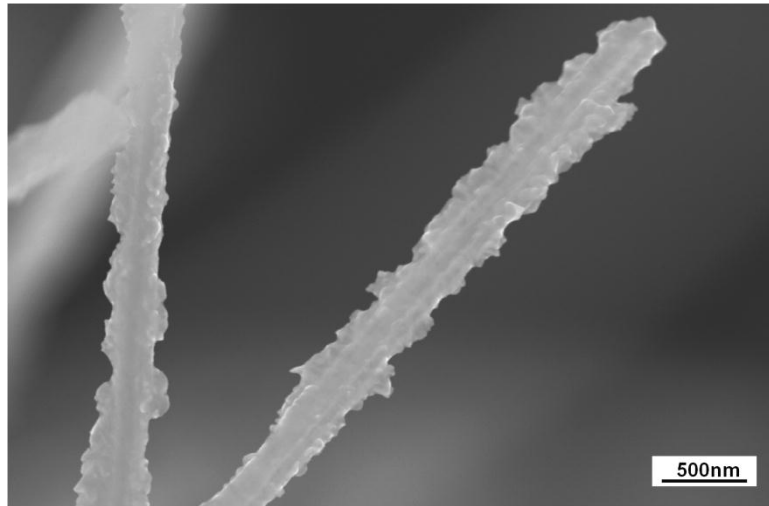


**Figure 31:** Side view SEM image of NWs on the substrate edge oxidized at 350 °C for 30 min. The temperature originated morphology alteration occurs predominantly at opposing, low-index crystal faces. Smooth morphology of faces of higher surface energy remains unchanged.

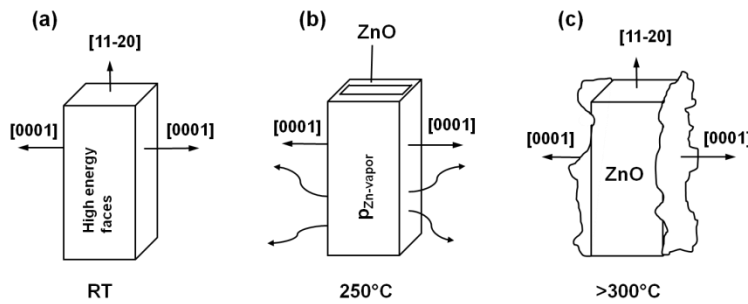


**Figure 32:** Schematic illustration of the morphology alteration process of CWPVD-grown Zn NWs. Scheme of a NW with corresponding crystal faces at room temperature (a). Zn NW annealed at 250 °C for 30min (b). The vapor pressure of Zn encapsulated by a thin oxide shell increases due to the low melting point of Zn. NW morphology which develops during oxidation at 300 °C for 30 min after outbursts formed (c).

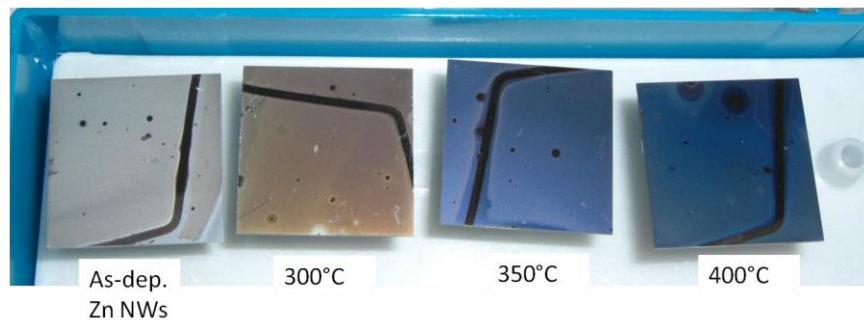


**Figure 33:** Color evolution of Zn NW-samples from grey (as-deposited), over yellow-brown, blue and dark blue. The oxidation was performed within 30 minutes each.

#### 4.2.1.4 Zn nanorhombs and nanobelts

During the synthesis runs of Zn NWs, also unique 2D structures formed, which this section is dedicated to. The understanding of crystal growth at the nanoscale can offer the possibility to arbitrarily control the morphologies. Although it has been reported on nanobelts of Zn [107], rhombic 2D structures (Fig. 36a-f) formed by CWPVD (see section 4.2.1) exhibit a novelty. However various morphologies of the related oxide (ZnO) have already been synthesized utilizing vapor-transport methods and often Au catalysts. Owing to the hexagonal crystal, Zn and ZnO tend to form elongated designs determined by thermodynamics and growth kinetics prevailing in the respective growth setups [108]. Wang et al. reported on e.g. ZnO *nanocastles* which can be formed by a switch in the vapor concentration inside the chamber [109], whereby zinc and oxygen are provided by carbo-thermal reduction at 950 °C. It is stated that at first a hexagonal base is grown and as soon as the furnace is switched off, the vapor pressure drops and allows for the formation of polygonal nanostructures at the outer walls of the hexagons, thus forming nanocastles. Fig. 34 shows a top view of such a nanocastle by means of SEM (a) and schematically with the respective crystal facets (b). Beside triangles and belts, also rhombic posts with lengths of few microns are observed. It is argued that supersaturation is still present in the second growth step, which induces the growth of the side features due to dangling bonds. Hence the crystal growth is perturbed here by a pressure-induced instability.

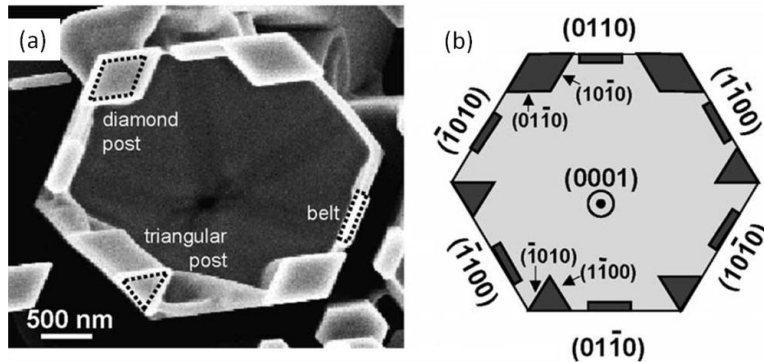


**Figure 34: ZnO Nanocastle by SEM (a) and schematically (b) with indicated crystallographic planes. The structure exhibits a monolithic crystal with nanosized features at the outer walls (taken from [109]).**

Similarly Yang et al. found elongated, ZnO rafts [110] growing on copper grids that were placed inside the reaction furnace at temperatures between 500 °C and 1000 °C. An example of rhombs growing on a ZnO belt is shown in Fig. 35 by means of SEM. The structures are expected to build up from hexagons whereas rhombic  $\{10\text{-}10\}$  planes develop at the expense of  $(0\text{-}110)$  and  $(01\text{-}10)$  planes (see Fig. 35b), which possess a faster growth rate. ZnO nanorods with a rhombic cross section have also been synthesized by Yu et al. [111] on Cu-filled porous silicon substrates. Here the morphologies obtained at 900 °C are interpreted as favored by the monoclinic lattice of CuO.

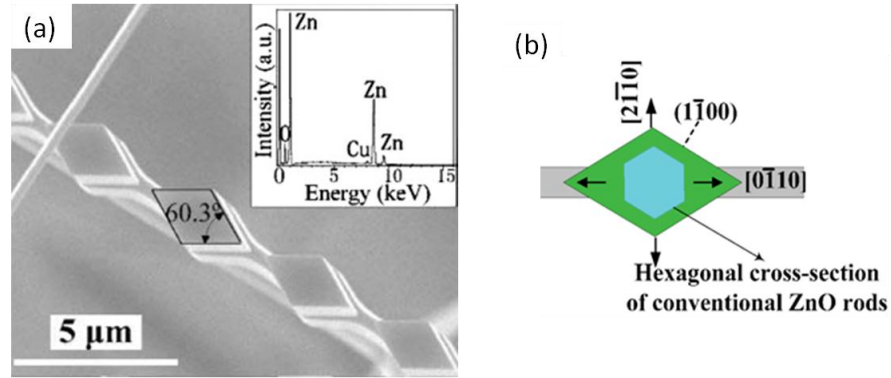


**Figure 35: Rhombic chain of Cu-doped ZnO formed on a belt-like structure examined by SEM (a). The EDX spectrum in the inset reveals a copper content of 1.6 at. %. Schematic relationship between hexagonal and rhombic structure is shown in (b) (taken from [110]).**

Based on the reports mentioned above one could regard the Cu or CuO contaminant as the cause of rhombic zinc oxide evolution. The evidence that the morphology of ZnO nanostructures can indeed be switched from NWs to nanobelts is given by Fan et al. [112]. An addition of  $\text{In}_2\text{O}_3$  and C to the source materials<sup>9</sup> lead to [11-20]-oriented belts instead of wires grown along the [0001]-direction. Hexagonal materials are known to grow along the energetically favored  $\langle 10\text{-}10 \rangle$ ,  $\langle 11\text{-}20 \rangle$  or  $\langle 0001 \rangle$  directions [113]. In order to allow a switch in the orientation as reported, the energy barrier from [11-20] to [0001] has to be overcome<sup>10</sup>. Fan et al. suggest that the ternary phase of Au as catalyst, Zn as precursor and In as the contaminant<sup>11</sup> (with a content of 4-6 at. % in the resulting structures) induces a certain strain which modifies the surface free energy and thus changes the nucleation behavior of ZnO. Likewise parameters like temperature, heating rate, synthesis duration as well as catalyst material and composition affect the morphologies of hexagonal GaSe nanostructures, as reported by Peng et al. [115].

The Zn rhombs and belts obtained by CWPVD are depicted in Fig. 36 by means of SEM. Edge lengths lie within a range from 750 nm to 1.5  $\mu\text{m}$  while the belts show lengths up to 13  $\mu\text{m}$ , widths from 480 nm to 1000 nm and thicknesses of less than 50 nm. The images in the upper row exemplify structures for which a Cu contamination of 0.27 at. % was found by EDX analysis. The Cu traces could have caused strain instabilities which changed the morphology from NWs into rhombs. For comparison, in reference [110], a copper content of 1.6 at. % was revealed by EDX. Since the electron contrast of a NW from behind is detected through the rhomb (circle in Fig. 36a), it is obvious that the rhombic plates have a very thin, quasi 2-dimensional morphology. In (b) the transition from a thin belt into such a rhombus is depicted. Fig. 36d-f show results in which a temperature step is applied from 100  $^\circ\text{C}$  to 150  $^\circ\text{C}$  during synthesis. Although also rhombs are observed, the thermal instability mainly provokes the evolution of belt-like zinc. A belt-wire-belt transition is e.g. depicted in Fig. 36d. The indicated angles of 60 $^\circ$  and 120 $^\circ$  (c and f) reflect the hexagonal symmetry of zinc. Since the free energy of equivalent lattice planes is the same and due to the fact that different morphologies coexist on a sample, it is obvious that the structural switches consume very little energy.

In section 4.2.1, TEM characterization revealed the NW growth to occur exclusively along the [11-20] direction which exhibits the plane of lowest energy under consideration of the respective kinetic conditions. This way the (11-20) plane vanishes since it possesses the fastest facet growth rate. When the

<sup>9</sup> Setup and growth conditions are comparable to the cases above. However NWs and belts formed via the VLS mechanism catalyzed by Au dots.

<sup>10</sup> Thermodynamically the [0001] direction is favored over the [11-20] direction (ref. [114]).

<sup>11</sup> Cu is supposed to originate from the base of the sputter target.

morphology changes e.g. from wire into a rhombus as a consequence of growth instabilities, 2D crystal growth along the equivalent facets  $(-1010)$ ,  $(-1100)$ ,  $(1-100)$  and  $(10-10)$  (see Fig. 35b) takes over. Thereby the  $(0001)$ -facet with the largest surface grows slowest while the fastest growth direction becomes  $[01-10]$ . Fig. 37 gives an overview over the crystal faces and directions involved. Strain or thermal perturbations are proposed here to overcome the energy barrier between  $[11-20]$ - and  $\langle 01-10 \rangle$ -growth and vice versa. This holds also for the belts (Fig. 36d and f). Comparison of the features from Figs. 36 (a) and (f) suggest that also the belts grow along  $\langle 01-10 \rangle$ , since the present  $120^\circ$  angles are related to the rhomb structures. Especially Fig. 36e delivers the directional relationship between NW and 2D structure.

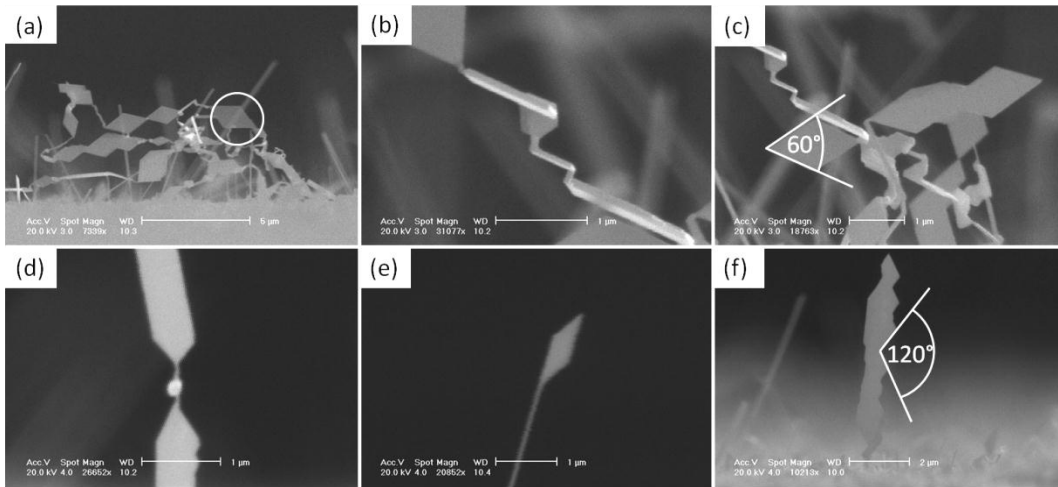


**Figure 36: Nanorhombs and -belts of Zn as well as “superstructures” by CWPVD evolving as a consequence of crystal growth perturbation. The indicated angles in (c) and (f) reflect the hexagonal symmetry.**

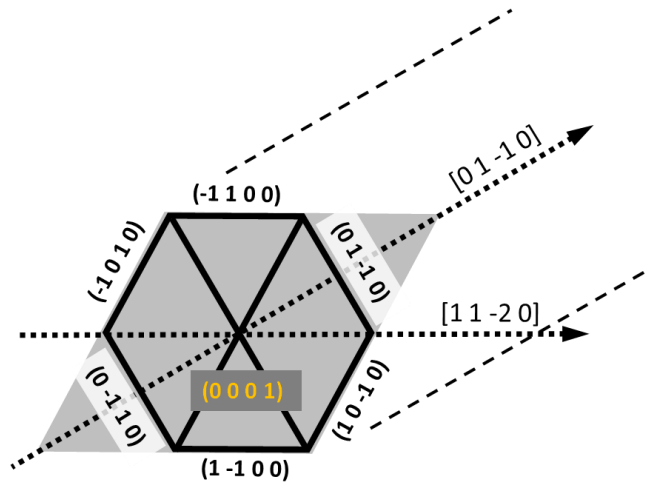


**Figure 37: Crystallographic relationship between the hexagonal lattice and rhombic structure. Lattice planes and growth directions of 2D structures ( $[01-10]$ ) and corresponding NWs ( $[11-20]$ ) are indicated. The image plane exhibits the  $(0001)$ -surface. Outer dashed lines indicate belt contour.**

Although it has been reported on sheet-like ZnO structures [116], the belt widths or rhombs are size limited. Obviously, at a certain point the sheets do not further grow but either start to shape a belt or an additional rhombic element. This point could be determined by adatom diffusion. In section 4.2.1 it is

pointed out that surface diffusion<sup>12</sup> plays a major role for the NW formation. It can be concluded that thermally driven diffusion is hampered by (i) thermal fluctuations and (ii) the lower average growth temperature applied in the cases shown in Fig. 36d-f. As a consequence the 2D-features are limited to dimensions in the range of the self-diffusion length of impinging Zn atoms at the prevailing temperature.

In general the occurrence of crystallization instabilities is favored by the low temperature of our setup. The higher the temperature the more likely it is that thermodynamical equilibrium is reached and kinetic aspects loose importance. A report on the thermodynamics of metastable phase nucleation on the nanoscale is given by [117]. It is stated here that the size dependence of the *Gibbs* free energy may contribute to the evolution of peculiar nanostructures.

## 4.2.2 Germanium nanowires

While Zn nanowires are grown at the AIT (Austrian Institute of Technology), the growth of Ge nanowires is carried out at partner institution, i.e. the Vienna University of Technology.

Various NW materials can be synthesized by the VLS process [63]. Thereby, the precursor vapor is cracked at the surface of a nanosized catalyst that is pre-deposited on the substrate surface. Subsequently, it is dissolved in the liquid droplet until it reaches the state of supersaturation. Provided there is an adequate eutectic phase of the respective material system, the precursor material precipitates continuously at the interface between the droplet and the substrate, thus forming 1D structures with the catalyst residing at the tip. In the present case, a diluted GeH<sub>4</sub> precursor (2% in He) is lead into a hot wall CVD system (Fig.38a) at a flow rate of 100 sccm and low chamber pressure of 75 mbar [118]. Ge NWs with diameters around 40 nm and lengths of few microns at a growth duration of 20 minutes are typical. The GMR substrates are protected with 40 nm GaN and finally coated with 2 nm thin discontinuous Au (catalyst) prior to the synthesis. Due to a eutectic temperature of 361 °C (Fig.38b) for the Au-Ge system, the growth is feasible at low temperatures of about 300 °C. In principle the NW diameters can be controlled by the catalyst sizes and the lengths by the growth time. Fig. 38 (c) and (d) depict the result of syntheses performed at 300 °C and 340 °C respectively. It is obvious that for the lower temperature, the NW density is significantly lowered while a crystallite background arises. In the present setup, tapering of the NW structures occurs (see inset Fig. 62a), the origin of which is attributed to the radial VS growth dynamics, meaning a deviation of the NWs initial radius from the “critical” radius [119].

---

<sup>12</sup> Formula (4.9) also applies for surface diffusion, when the adequate activation energy is set in and 1/6 is replaced by 1/4.



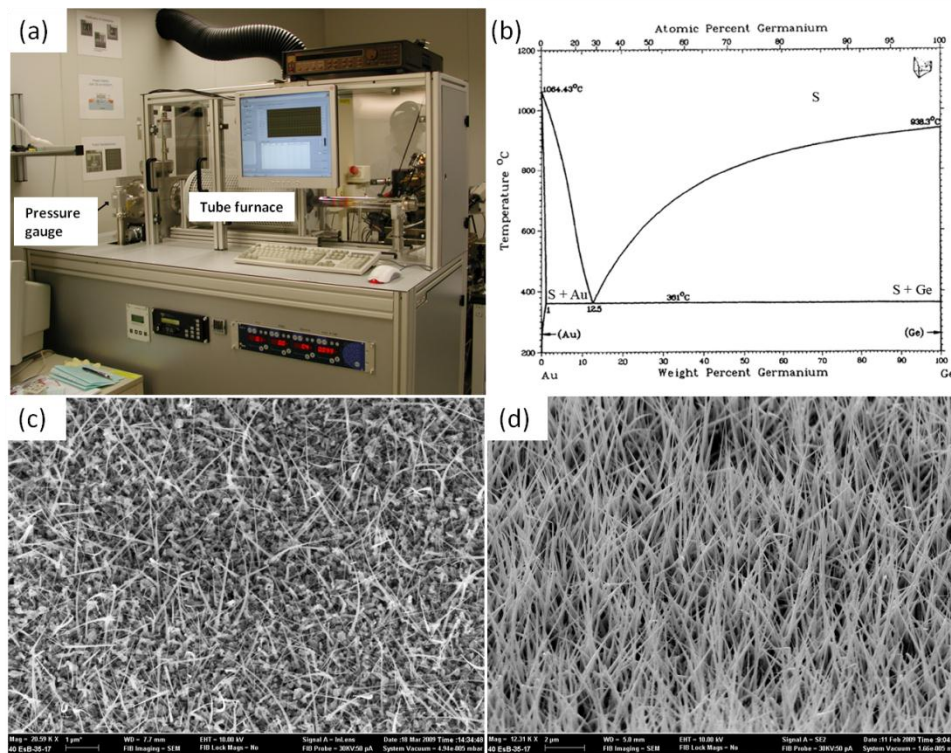


**Figure 38:** Low-pressure CVD system for the synthesis of GeNWs via the VLS growth process (a). Schematic Au-Ge binary phase diagram (b). Germanium NW synthesis at 300 °C (c) and 340 °C (d) on a GMR substrate.

### 4.2.3 Polypyrrole nanowires

This section concentrates on polypyrrole, ( $C_4H_5N$ ) one of the principal families of conducting, conjugated polymers, which are synthesized by an oxidative polymerization [120]. PPy was discovered by Diaz et al. [121] in 1979 and since then it is predominantly applied in electrodes, actuators (due to its electro-activity), capacitors and anti-corrosion coatings. Although it has been reported on nano-structuring [122] and nano-composites [123] of polypyrrole, there are few studies published of PPy NWs [124, 125]. The template-free synthesis is conducted according to [124].

With the addition of perchlorate ( $NaClO_4$ ) ions into the electrolyte solution, the morphology of the deposit can be switched from film to the aimed NW structures. Thereby, at first an insulating PPy film (see inset Fig. 41b) forms that incorporates weak acidic  $HPO_4^{2-}$  ions. However, the further mechanism is not yet completely understood, it is described in [124] that water oxidation leading to the local formation of  $O_2$  in combination with the non-reactive perchlorate counterions causes the formation of rod-like<sup>13</sup> structures with lengths up to few microns and diameters between 80-150 nm. The film, located at sites where no wires evolved, experiences overoxidation<sup>14</sup> of the polymer accompanied by de-doping, i.e. a release of ions and a loss of conjugation and electrical conductance (see Fig. 39).

<sup>13</sup> Nevertheless, based on [22], the structures are called NWs in the following.

<sup>14</sup> Is expected to occur as a consequence of water oxidation and OH radical formation.



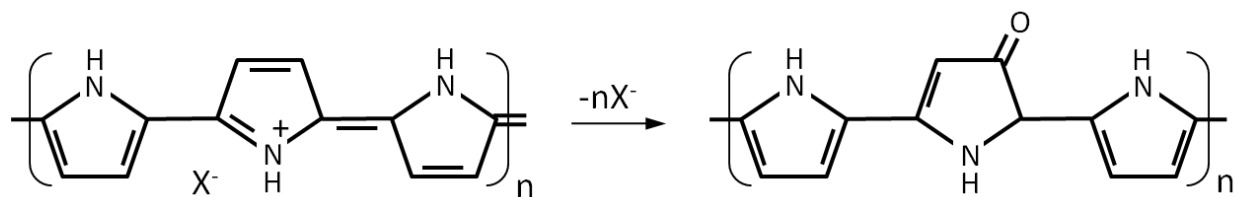


**Figure 39: Genuine polypyrrole (left) and the overoxidized composition (right) showing an oxygen bond at the expense of conjugation.**

Prior to the NW synthesis, 2 nm of tantalum as adhesive layer and a 15 nm Au seed layer are deposited on the GMR sample (which represents the working electrode) to ensure sufficient electrical conduction for the electrodeposition process. A 20 nm thick insulation of MgO between the GMR layers and the Au layer prevents shunting of the sensor (see Fig. 19). For the counter electrode, a 20 mm x 20 mm silicon wafer (50 nm thermal oxide) was sputter-coated with 5 nm of titanium as adhesion mediator and 80 nm of Au. A solution of 0.2-molar  $\text{Na}_2\text{HPO}_4$  for the electrolyte and 1-milimolar  $\text{NaClO}_4$  for the non-reactive ions is prepared. Since pyrrole downgrades and polymerizes under UV-illumination and air contact, the polymer processing and the NW synthesis is performed under inert gas atmosphere. Therefore, after 2 minutes of ultrasonication the vessel is introduced into a glove box with argon inert gas, which is flushed with pure argon at a flow rate of 20 l (normalized) per minute until the residual gas concentration in the atmosphere falls below 200 ppm. A pyrrole volume (260  $\mu\text{l}$ ) according to a 0.15-molar pyrrole concentration is then pipetted into the solution. Subsequently, the electrodes are positioned in a teflon holder at a plane parallel distance of around 2.5 cm (see Fig. 40a), the clamps are mounted and the whole apparatus is placed into the solution and sealed by a teflon lid and a paraffin-based “parafilm” closure foil. The sockets for the electrode plugs have also been sealed. For the synthesis (Fig.40b), the vessel is protected to UV-illumination by aluminum foil and the parafilm is pierced through by the plugs (red and black in Fig.40a) to exclude major oxygen contact. The region of deposition can simply be confined by Kapton tape (Fig.40c). The black area represents a PPy NW array attesting strong light absorption (black color). In the left region, the deposition has been blanked. During synthesis, the area captured by the meniscus of the liquid was also blanked to avoid capillary effects (see circle in Fig.40a).

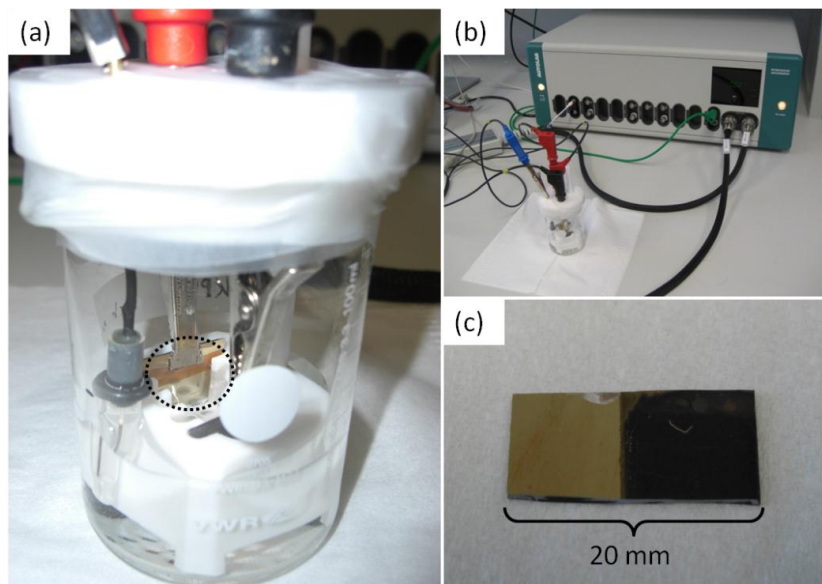


**Figure 40:** Sealed vessel with electrode setup is shown in (a). The red contact plug belongs to the working electrode and the Ag / AgCl reference electrode is located left inside the vessel (grey top). The potentiostat setup is shown in (b). A gold coated substrate partly deposited with PPy NWs is depicted in (c). The growth region has been confined by Kapton tape (see also circled region in (a)).

Fig. 41a shows the current curve under constant potential with a steep decrease in the initial phase, followed by a slight increase over time which is characteristic for the polymerization. In a later stage of the experiment (~5500 s), this increase breaks down once the potential drop across the film becomes too large. At this point, the NW growth stops. By applying a larger potential, the current increase can be shifted to a shorter and steeper form. Owing to the self-assembled nature, the structure morphology depends strongly on the various transition resistances of the setup configuration and parameters like electrode pretreatment and electrolyte. In (Fig. 41b), typical wire morphology is depicted by means of SEM. Due to the polymers intrinsic electrical conductance, the picture could be recorded without any prior metal coating to prevent sample charging. The inset shows a sample cross-section with wires at the interface. The mentioned overoxidized PPy layer reveals a thickness of only 80 nm.

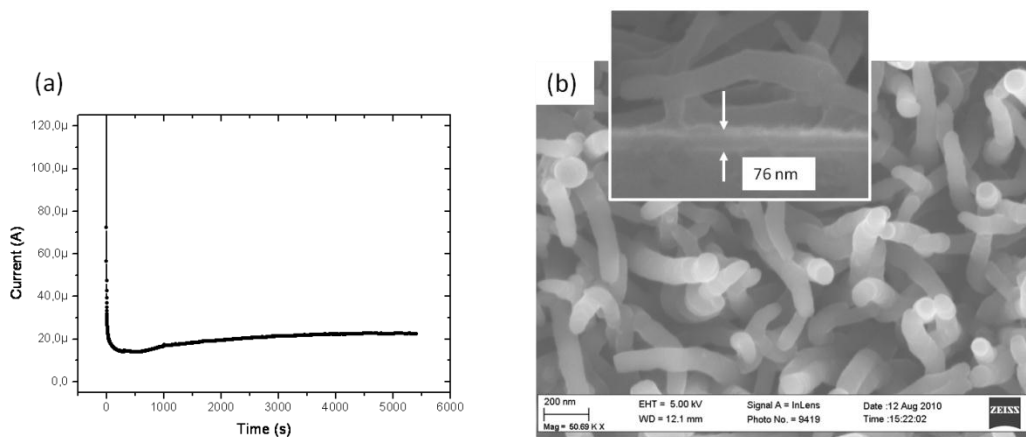


**Figure 41:** Current as a function of time during the synthesis of PPy NW (a). Top-view SEM image of characteristic PPy NW morphology on a GMR substrate (b). The inset shows a cross-sectional image of as-deposited NWs. Underneath the array, an overoxidized polypyrrole (OPPy) layer formed.

#### 4.2.4 Nanorods by electron beam lithography (EBL)

To supplement the self-assembly NW systems, an approach of top-down assembled nanorods with EBL is presented. In this case, the substrates are left as-deposited without any protective layer or seed. Instead, the resist structures are directly arranged onto the GMR substrate by lithographic means. A negative e-beam resist (“Allresist ARN7500.18”) is spun onto the sample twice to achieve a thicker layer. Afterwards, the sample is loaded into the chamber of a “Zeiss Supra 40” SEM, aligned and finally exposed in a point by point pattern. After the exposure, the sample is treated in a developer and stopper liquid (Fig. 42). By tilting of the sample during exposure, an oblique rod alignment can be achieved which is intended to favor the approach towards the sensor. The employed processing parameters are outlined in table 3.

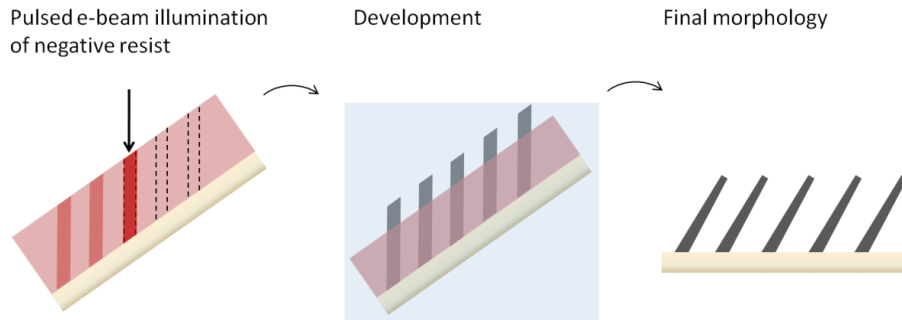
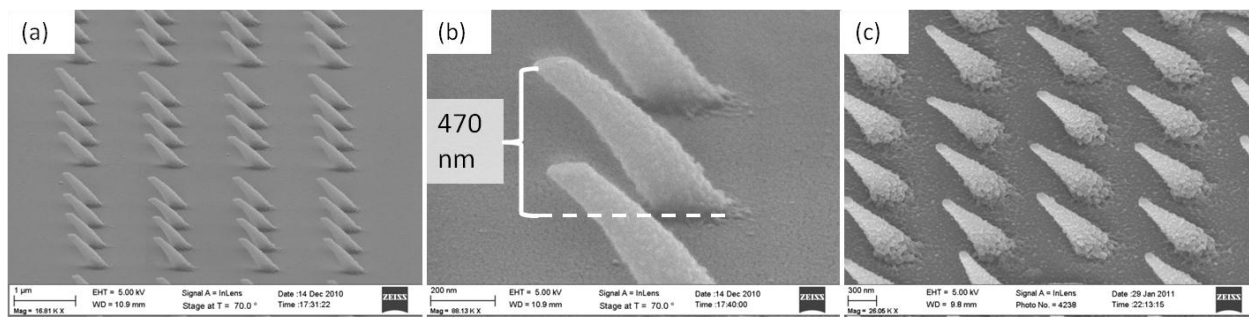


Figure 42: Schematic of the e-beam process flow.

Table 3: Parameters of the e-beam process.

Spinning	Bake	Devel./stopper each	Dose	Working dist.	Acc. voltage	Beam current	Aperture
2 (krpm) 30 s	1(2) min at 85 °C	55 s	8.4 x 200 $\mu\text{As}/\text{cm}^2$	10 mm	20 kV	~40 pA	10 $\mu\text{m}$

The resulting resist structures shown in Fig. 43a-c possess lengths between 700 nm and 1000 nm and center diameters of ~150 nm. From Fig. 43b, it is obvious that the distance from the tip to the surface amounts to about 500 nm, which is given by the total resist thickness. Though the structures excel in flexibility, density, mutual mobility and proximity to the sensor surface, the serial writing process is time consuming. The assembly of an array 0.5 mm<sup>2</sup> in size takes more than 14 hours for the given setup. Hence, it is impossible to equip an area of approximately 70 mm<sup>2</sup>, which amounts to that of the applied active area for the Zn and PPy devices, in a reasonable time with rods. To compensate, the sensor area is confined lithographically to rectangular meanders (see section 5.4).



**Figure 43:** Tilted (a, b: 70° and c: 40°) SEM images of an obliquely arranged (~45°) nanorod array synthesized by electron beam lithography.

## 4.3 Magnetic tagging

### 4.3.1 Nanoparticles: thiolate-Au bond (Ge system)

For the tagging, various techniques have been applied. Originally, VLS-grown Ge NWs were intended for the sensor design. An elegant way to bind magnetic material onto their Au tips - which are their natural seeds - seems the thiolate-gold bond. Thiols are known for their strong chemisorption (binding energy: 28 kcal/mol) to noble metals via covalent (and also slightly polar) interactions [126]. The adsorption brings molecules together and allows for two-dimensional ordering and thiolate monolayer formation via intermolecular *van der Waals* interactions [127]. The specific immobilization of nanoparticles can be achieved with a crosslinker, e.g. EDC (1-Ethyl-3-[3-dimethylaminopropyl] carbodiimide hydrochloride) which connects the interface group of thiol with the functionalization of magnetic / superparamagnetic nanoparticles [128]. The crosslinking is outlined in Fig. 44.

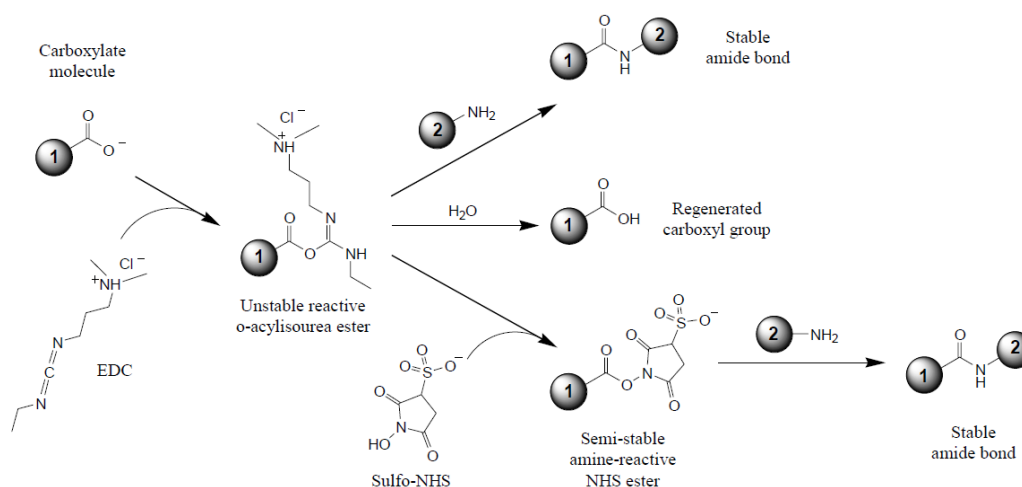


**Figure 44:** EDC crosslinking of carboxylates with amines taken from [128].

In this work, MHA (mercaptohexadecanoic acid) and  $\text{NH}_2$ -groups are utilized, respectively (Fig. 45a). To that end, a cleaned (10-20 s in 3 % HF and 30 s in 10 %  $\text{H}_2\text{SO}_4$ ) silicon wafer is coated with 3 nm Au and annealed to obtain an island-like coverage. The sample is then incubated (24 hours) in a 1 millimolar MHA-ethanol solution. Next, it is exposed to a 2 millimolar solution of EDC in distilled water. After the

addition of  $\text{NH}_2$ -functionalized, superparamagnetic particles (Nanomag 1301252, diameter: 250 nm), the solution is stirred for 2 hours. Subsequently, the sample is rinsed to flush away unspecifically bound molecules. The result is shown in Fig. 45b by means of AFM. In principle, the immobilization is demonstrated, however the binding density appears low. A reason therefore could be weak binding, particle agglomeration or binding that works only starting from a critical size of the Au islands. In any case however, the density of magnetic particles is low with respect to a magnetic response, which the particles would have on a plane GMR sensor.

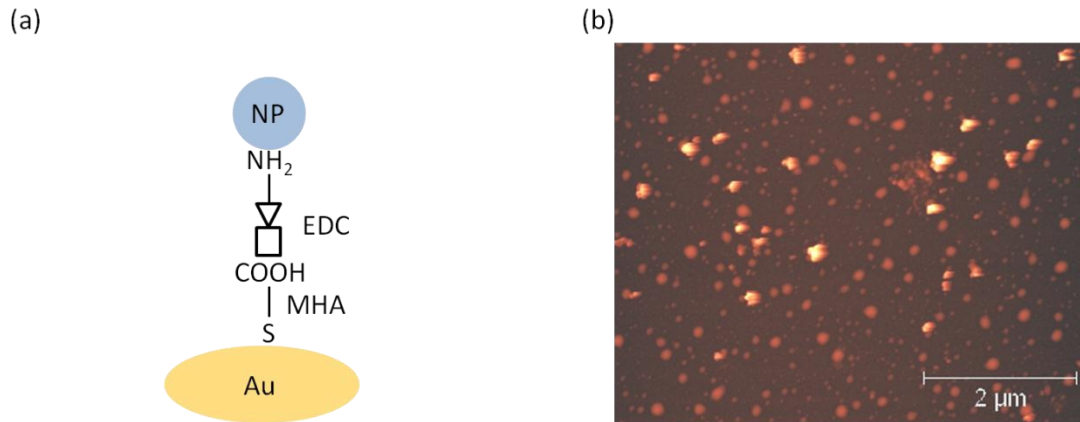


**Figure 45: Schematic of the immobilization of an  $\text{NH}_2$ -functionalized nanoparticle to a gold island via EDC and thiol bond (a). The result of (partial) immobilization on a 3 nm Au layer is shown in (b) by means of AFM. The bright dots denote bound nanoparticles.**

The same binding procedure applied to a Ge NW surface led to unsatisfying results, since the Au tips of these conical structures usually measure less than 20 nm. The resulting reactive area has proven to be much too small. Additionally, the Au residing at the Ge NW tips is strongly curved and contaminated with precursor material. Fig. 46 shows unspecific binding of the particles applied by this procedure to VLS-grown silicon NWs as a consequence of adhesion on the NW-“roughened” surface.

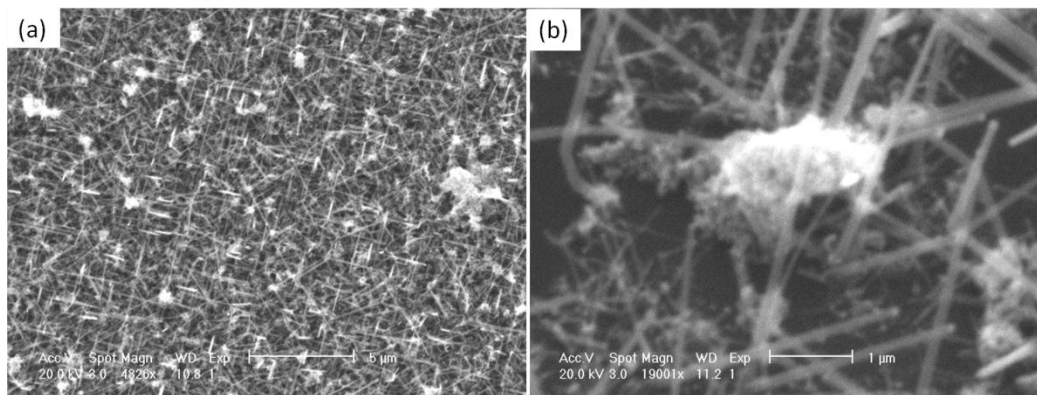


**Figure 46: Low (a) and high (b) magnification SEM image of functionalized “Nanomag”-particles and respective agglomerations on a Si NW surface. The binding is unspecific with a low density.**

### 4.3.2 Sputter deposition and lift-off (Ge system)

In order to tag the NWs exclusively at the tips, sputter deposition is combined with a lift-off process (Fig. 47). These experiments have been carried out with Ge NW samples due to the equal length distribution of these nanowires.

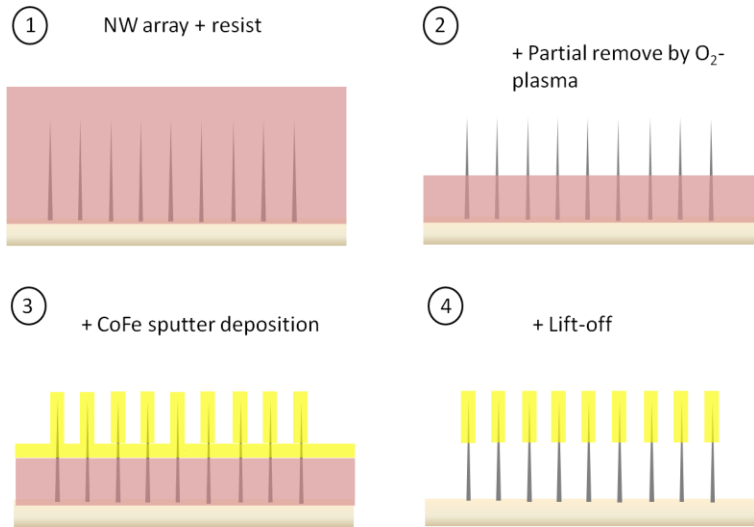


**Figure 47: Schematic of the intended process for the attachment of CoFe to the NW tips.**

The fabrication process starts by spin-coating a photo resist onto the nanowire sample (AZ5214E spun for 30 s at a speed of 5 krpm). Next, the resist is pre-baked for 50 s at a temperature of 110 °C. Fig. 48a presents a SEM image of Ge NWs grown at 340 °C embedded in the resist after free-etching of the tips in an O<sub>2</sub>-plasma device at a power of 150 W for 5 min. Fig. 48b shows the same sample after coating it with 250 nm of copper (for test purposes) and a subsequent lift-off in acetone by SEM. Though the process seemed to work for the Cu deposition (as there is no residual resist observed), it is unclear what happened to the NW roots. Fig. 48(c) and (d) give the results for a similar process, but with a 150 nm thick Co<sub>50</sub>Fe<sub>50</sub> film as tagging. In (c), the sample is depicted after back-etching in an O<sub>2</sub>-plasma reactor (Femto, Diener electronic) with a power of 50 W at 70 °C and subsequent Co<sub>50</sub>Fe<sub>50</sub> coating. It is obvious that the NW density seem to have decreased since a fraction of shorter and/or obliquely oriented wires got buried by the resist. However, successful coating of the free wire tips is confirmed by the increase in wire diameter. Resist lift-off is performed in acetone at 75 °C for 20 min. SEM characterization delivered unsatisfying results and the lift-off was repeated in NMP (MR1165) remover at 80 °C for 2 hours. It turned out that the magnetic metal still strongly coheres and either adheres to the wires (Fig. 48e) or breaks or crops the wires off the substrate. Fig. 48f shows a part of the surface, whereas the coating is detached as a whole. Under-running of the solvent is obviously hampered by the density of the NW array. Ultrasonication during the lift-off is not applicable since the NWs are immediately detached from the substrate even at a low power level.



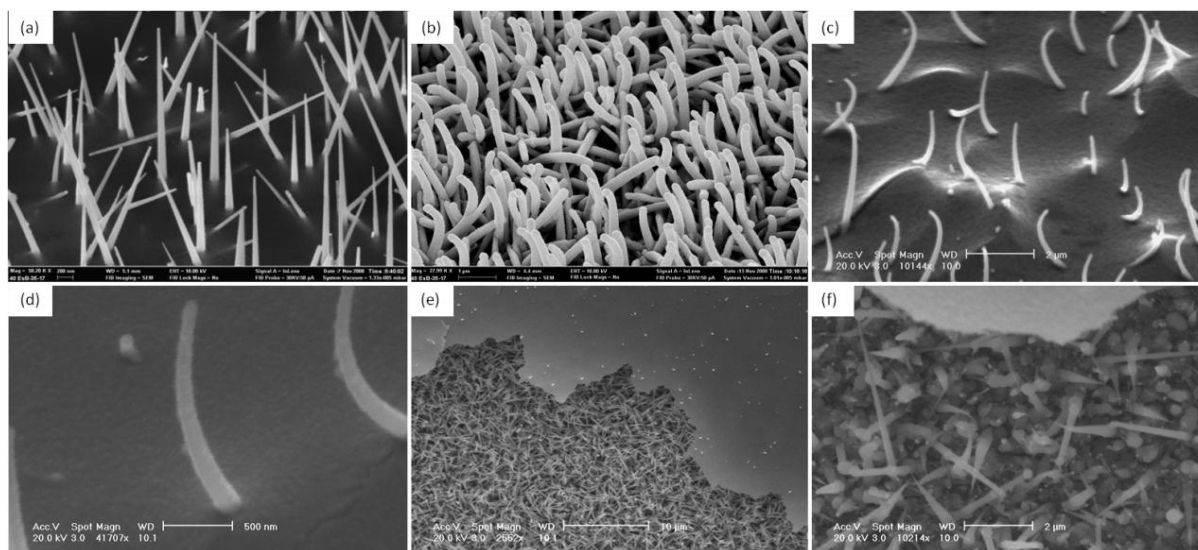


**Figure 48:** Ge NWs embedded into AZ5214 photo resist and subsequent opened at the tips by O<sub>2</sub> plasma etching (a). The resulting structures after coating with 250 nm of copper and resist lift-off in acetone are shown in (b). The lift-off procedure applied to Ge NWs coated by CoFe is depicted in from (c) to (f). The arrays are characterized by SEM after being embedded into AZ5214 photo resist, partial removal at the tips by O<sub>2</sub> plasma etching and sputter coating of 150 nm CoFe in low (c) and high (d) magnification. Images (e) and (f) attest non-satisfying result since the magnetic metal only partly detaches after 2 hours of lift-off in NMP (MR1165) at 80 °C.

### 4.3.3 Nanoparticles: EDC-crosslinking (PPy system)

In section 4.3.1, an EDC-crosslinking procedure in combination with a thiol bond is introduced. Here, the crosslinking of carboxyl (COOH)-functionalized superparamagnetic particles (“Nanomag“ by miromod) to the NH-group of the PPy NW array is described. Again, an EDC crosslinker is adducted for the covalent binding procedure (see Fig. 44). A fraction of the particle solution is incubated with 0.4 molar EDC and 0.1 molar NHS (N-hydroxysuccinimide). The particles are subsequently separated from the solution with a NdFeB magnet and transferred into an acetate buffer (pH between 5 and 6). Next, the nanoparticles are pipetted at a concentration of 100 µg/ml onto the NW-coated substrate and dried. The amount of applied nanoparticles is expected to allow for a dense, continuous coverage. The incubation and drying is performed in a well tightly fitting the extents of the NW-coated substrate, which is fabricated by fixing a PMMA frame onto a glass slide<sup>15</sup>. The frame surrounding the sample is intended to assure coherent drying and exclude capillary effects. The drying however lasts longer than the binding/incubation process (several hours, depending on the amount of liquid). This is disadvantageous since the COOH-groups most likely recover within the drying time (see Fig. 44). Agglomeration occurred as is observed by means of SEM in Fig. 49a. To avoid magnetically induced agglomeration, the separation step has also been carried out by centrifugation instead of the use of NdFeB magnets. However, the result has neither been satisfactory. In general, the images from Fig. 49 suggest failed cross-linking, since no coherent binding is found.

<sup>15</sup> The PMMA surface has therefore been exposed to an O<sub>2</sub>-plasma for cleaning, roughening and the activation of C-O-groups prior to the fixation to the glass slide.

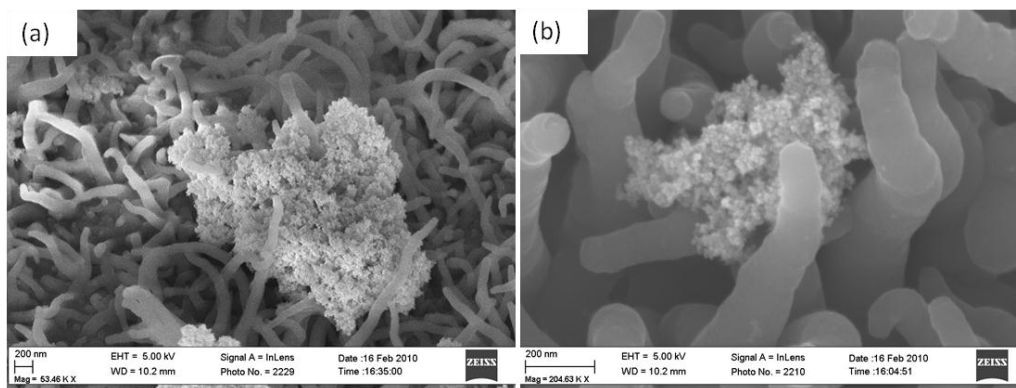


**Figure 49: Low (a) and high (b) magnification SEM images of COOH-functionalized superparamagnetic particles on top of a PPy NW array. The images indicate non-spherical particle morphologies and agglomeration.**

There have been further attempts to non-specifically bind ferromagnetic and superparamagnetic nanoparticles (see following compilation) to the PPy arrays.

- (1) Micromod: 45-00-202, pure iron oxide, nominal diameter: 200 nm
- (2) Micromod: 09-02-502, nanomag<sup>®</sup> -D, COOH terminated, nominal diameter: 500 nm
- (3) Micromod: 39-02-153, sicastar<sup>®</sup> -M, COOH terminated, nominal diameter: 1500 nm

However, the shape of the utilized particles (when dried), particle conglomeration and the contamination of the NW array by solvent or buffer residues, remain problematic. The homogeneity of the particle coverage - even for superparamagnetic particles which lack spontaneous magnetization - is insufficient. With permanent magnets (see NdFeB disc from section 2.9) positioned underneath the sample during drying, a more homogeneous distribution has been anticipated due to magnetic repulsion of particles within the surface layer, but the result of these experiments also turned out to be not satisfying.

#### 4.3.4 Nanoparticles: non-specific binding (e-beam resist)

In case of the e-beam synthesized rods, tagging via sputter deposition is not applicable due to the lower wire density. Also, from Fig. 69a it is obvious that the structures - when coated with 100 nm CoFe - are pulled down to the substrate surface. Consequently, superparamagnetic beads (Bioclone BcMag<sup>™</sup>, diameter: 5  $\mu$ m, COOH-terminated, magnetization: 40-45 emu/g (kA/m)) are applied as magnetic tagging. Like some of the particles described in the previous sections, the beads consist of iron oxide ( $\text{Fe}_3\text{O}_4$ )-clusters embedded in a silica matrix. The solution is pipetted and dried onto the rod array. As seen from Fig. 69, the particles, which are expected to adhere to the resist non-specifically [129], have proven to be stable even after drying out of the solution. Due to the larger diameters (nominally 5  $\mu$ m), the particles appear spherical but show broad size distribution (see section 5.4 for further details). For the preparation (concentration: 1600  $\mu$ g/ml), the particles are collected with a small NdFeB-magnet and subsequently the original stock solution is exchanged by *MilliQ*<sup>16</sup> water. This way, contamination of the NW array can be completely avoided.

<sup>16</sup> Highly pure, deionized water with a resistivity of 18.2 M $\Omega$ cm.



### 4.3.5 Sputter deposition

Unfortunately, the attachment of magnetic particles via cross-linking and also the tip-directed coating by sputter deposition and subsequent resist lift-off failed. Consequently and at the risk of attaching material to the NW roots, tagging is provided in the following by sputtering of high moment  $\text{Co}_{50}\text{Fe}_{50}$  metal. This is done successively with the following parameters:

DC plasma, Ar gas at 2  $\mu\text{bar}$  and 6 sccm, 80 W, 0,18 nm/s.

To avoid destructive heating (especially in case of PPy samples), the sources are cooled and only 100 nm are deposited at a time. The material is again deposited locally on the substrate by the use of shadow masks and Kapton tape. Unless otherwise stated, the experiments presented in the following are carried out with such a sputter-deposited magnetic tagging.

## 5 Measurements

The presented measurements refer to the setup introduced in section 2 and are intended to attest a proof of the concept. The aim is the detection of an AC voltage signal from the embedded GMR sensor, which is attributed to a periodic distance change of magnetic NW tips relative to the sensor substrate when mechanically agitated by piezo actuators. Approach or withdrawal of the tips is expected to occur either as a consequence of inertial forces or resonant deflection. The NW morphologies introduced in the previous section are investigated. A rigid fixation of the samples to the piezo drive is provided with conductive silver paste, which also allows for an easy release of the sample after the measurement. The sensor signal is read in a 2-point or 4-point geometry, and the electrical connections to the sensor are established by soldered indium contacts to thin elastic wires (diameter: 0.25 mm), thus assuring decoupling from the agitation (see Fig. 50a, b). The wires are connected to commercial probe tips which are screwed to the probe arms. The connection is established by soldering and “crimp” contacts. Due to limitations of both the piezo response and the lock-in amplifier, the accessible frequency range is limited to below 250 kHz. In this work, the GMR sensor exclusively comprises magnetic multilayers in CIP geometry. Measurements are carried out by recording the AC voltage signal as a function of frequency  $f$ . Unless otherwise stated, the situation refers to the shear actuator in vertical, i.e. z-extension, and agitation voltage indications refer to the amplified peak-to-peak voltage  $U_{pp}$ , which is generated as sinusoidal signal by the function generator and serves as reference for the lock-in amplifier.

### 5.1 Zinc nanowires

For the reasons of comparison and validation, all measurements presented in this section stem from one single device. Fig. 50a indicates the wiring of a sample with as-grown Zn NWs on top of the GMR sensor and its mounting to the probe station. The NW equipped sensor area is about 12 mm x 6 mm and its zero-field DC resistance is about 9  $\Omega$  with a GMR amplitude of 10 % and a saturation field of about 75 Oe (see Fig. 51). A side-view of Zn NWs on the sample edge is shown in Fig. 50c. The wires incline arbitrary angles (see section 4.2.1) with the substrate, meaning that the tip-substrate distance is - on average - smaller than the full nanowire length.

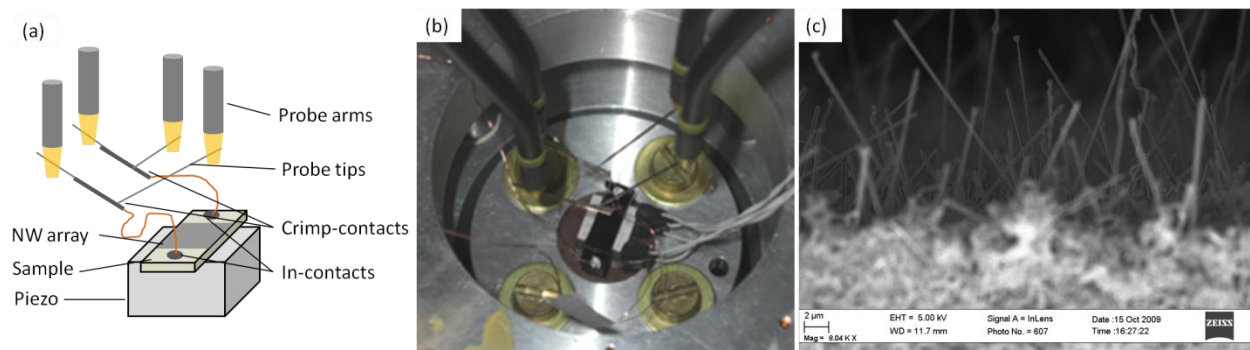


**Figure 50:** Schematic of the sample wiring (a) and corresponding photography of the sample fixed to the piezo actuator and mounted to the probe station (b). A cross-sectional SEM image of the sample shows the Zn NW morphology (c).

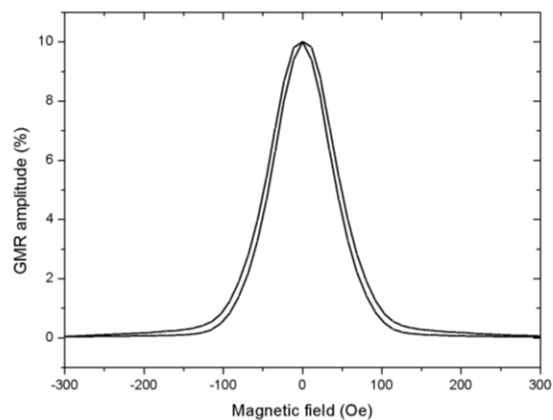


**Figure 51:** GMR sensor response of the device depicted in Fig. 50.

In order to identify the desired mechanosensing “effect”, the measurements are parameterized by the passed in-plane sensor current as well as the external magnetic field. In case the measured AC voltage relates to magnetically induced sensor resistance changes, a modification of the probe current should lead to a proportionally changed AC output voltage according to *Ohms* law. The effect of the magnetic z-field is given by magnetizing the  $\text{Co}_{50}\text{Fe}_{50}$  coating perpendicular to the sensor plane, which is expected to lead to an increase of the induced magnetic stray field within the sensor area. For frequencies at which the magnetic coating actually oscillates with respect to the sensor plane, the increased magnetic interaction induced by the magnetizing field should also lead to higher AC voltage amplitudes of the sensor output.

It is assumed that due to the huge shape anisotropy of the sensor layers, the z-field is unable to affect the sensor magnetization significantly<sup>17</sup>. Therefore, prior to each measurement the effect of z-field on the GMR properties of the sensors is investigated. The alignment of the chuck within the setup is assured to be such that the GMR amplitude is not affected by the magnetic field within the range of field strengths used (i.e. possibly occurring in-plane field components due to a misalignment of the magnetizing z-field with respect to the sensor plane are balanced by fine-adjustment of the field angle).

Fig. 52a shows 4-point signals of a typical GMR device with as-grown Zn NW (reference: uncoated state) in dependence of the frequency, which is swept between 50 k Hz and 250 kHz in 100 Hz steps. For

<sup>17</sup>The layer thickness can be regarded as infinitely thin compared to its lateral dimensions. Therefore, a demagnetizing field with strength comparable to the saturation magnetization of NiFe (namely 860 kA/m [61]) is necessary to turn the magnetization out of plane.

all measurements, the lock-in sensitivity and integration time are set to 20  $\mu\text{V}$  and 7.5 s, respectively, and a waiting time of 2.5 seconds is allowed after each frequency step before data recording. Thus, a single frequency sweep takes several hours. Below 50 kHz, resonances in the wire connections lead to prominent noise. The piezo agitation<sup>18</sup> is adjusted either to 50 V (triangles) or 100 V (circles). These values are expected to lead to reasonable piezo extensions in the given frequency range. For the pink and bright blue curves, an in-plane current of 20 mA is passed through the sensor, whereas only for the pink data a magnetic field of 50 Oe is applied. Black, brown and red data belong to an in-plane current of 40 mA. They depict the situation for zero-field, 50 Oe and 100 Oe, respectively. The general signal behavior shows “bumps” around 140 kHz and 220 kHz that reach AC voltages of 3.9  $\mu\text{V}$  and 5.0  $\mu\text{V}$ , respectively, which reflects the response of the soldered contacts and the piezo drive. As the first resonance of the shear actuator is located around 150 kHz (unclamped) the mentioned “bumps” could be correlated with the actuators intrinsic mechanical properties. This behavior is characteristic and since it scales with agitating voltage  $U_{pp}$  (compare circles and triangles in the data), it could be attributed to Joule heat, that causes a larger resistivity in the sensor layers. The heat power produced by the actuator can be assessed by

$$P = \frac{\pi}{4} \tan \delta f C U_{pp}^2 \quad (5.1)$$

with  $\tan \delta$  representing the contribution of dielectric losses.

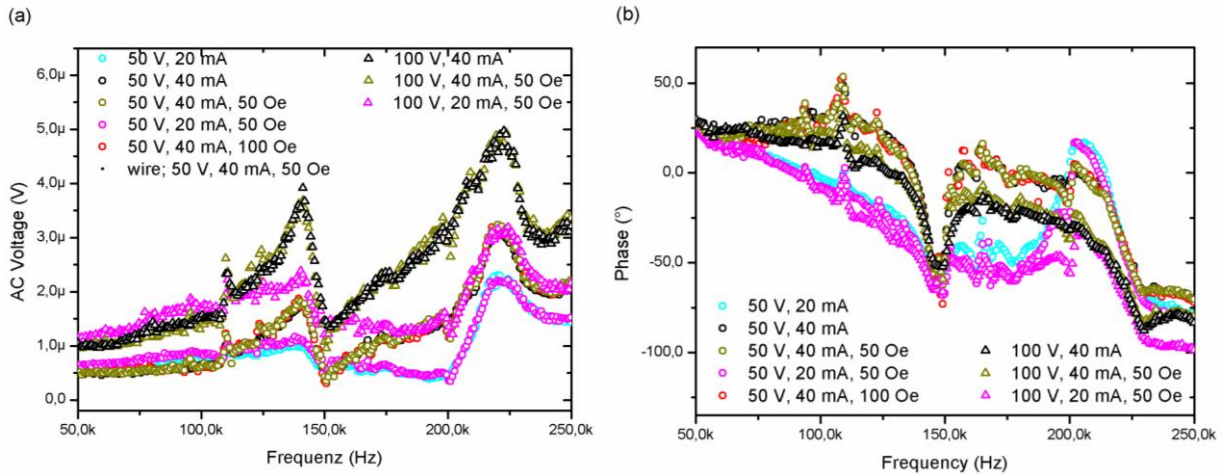


**Figure 52: AC sensor voltage (a) and corresponding phase (b) of the reference signal as a function of frequency when agitated from 50 kHz to 250 kHz.**

One further effect is striking which arises in the presented reference data. Since not all curves of a given agitation amplitude coincide, but only those recorded with the same sensor current passed, a current induced artifact arises (predominantly at higher frequencies) which separates the 20 mA and 40 mA data for 50 V and 100 V each. Therefore, thermal effects can be excluded as source of this separation, as this effect would not depend on the current. Any inverse magnetostriction from deformation of magnetic layers in the sensor can also be excluded, since magnetostriction can be neglected for NiFe, which is mainly used in the sensor layers. This finding is confirmed as the branching is also present in reference experiments replacing the GMR sensor by a 60 nm aluminum layer without NWs, which possesses definitely no magnetostriction. Though the sensor current dependent splitting for reference systems

<sup>18</sup> The actuator extension follows proportional to the applied voltage.

without magnetic tag is observed in the present case, it has proven to be irreproducible for similar systems. Hence the current branching is ascribed to an artifact caused by the soldered contacts.

The phase angle between the measured AC voltage and the agitating stimulus is depicted in Fig. 52b. Like the voltage data in (a), the “current” branching is present, whereas the data, especially those of the 40 mA-current, also branch with the agitation voltage. Fig. 42 shows NWs of the same sample tagged with 150 nm CoFe by means of SEM. The coating led to slight wire bending as a consequence of lattice strain. The origin, therefore, can be different thermal expansion coefficients of Zn and CoFe during post-deposition cooling. Beside the wires, also “wool-like” crystallites are observed (Fig. 53a) which potentially also contribute to the sensing effect.

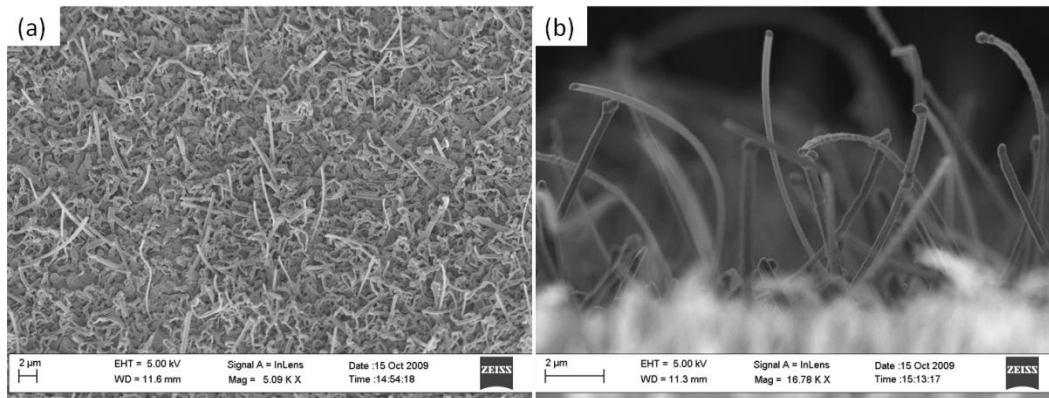


**Figure 53: Low (a) and high magnification side view SEM image (b) of Zn NWs arranged on a GMR sample and tagged with 150 nm of CoFe. The image in (a) is taken at 40° tilt of the sample normal relative to the electron beam.**

In Fig. 54, measurements of the tagged device agitated by applying 50 V piezo drive voltage are depicted. Since the contacts have to be reestablished after the tag deposition, non-systematic differences relative to the reference arise despite all other measurement parameters are kept the same. Deviations of pink and blue data from the other curves (in voltage and also phase) could attest the aimed sensing effect since the branching is a consequence of different sensor currents (20, 40 mA). The effect, however, could also be ascribed to the artifact which is revealed by the reference measurements. It has to be stated here that the irreproducibility caused by the subsequent contacting presents a major drawback in terms of the interpretation of the results. Phase differences mainly appear among data of different in-plane currents. In order to avoid induced voltages (by a temporal change of magnetic flux) in the measurement circuit, the contact wires (see Fig. 50a) are wound around each other before any measurement is started. Any currents evolving from those voltages will then be compensated. Rudiments of such inductions, however, are still observed around the minor “bump” of the black, brown and red data in Fig. 54a. Therefore, measurements with applied external magnetic field (brown and red) differ from the black line recorded at zero field. In the corresponding phase curves, the 20 mA data without an external field applied defer significantly from the others.

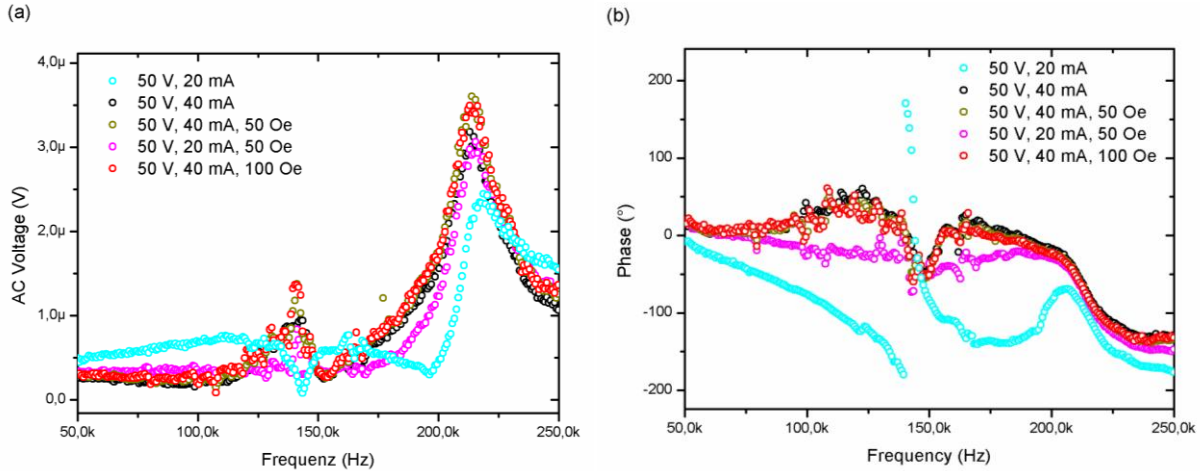


**Figure 54:** Voltage (a) and corresponding phase (b) of the Zn NW sample tagged with 150 nm of CoFe as a function of frequency.

After these measurements, the sample has been demounted from the setup and coated with 200 nm of additional CoFe metal in a second run. The decline of the GMR amplitude could originate from a slight shunting effect of the tagging through the insulating layer, but remained within 1.5 % throughout this section. Respective measurement data is shown in Fig. 55a for 50 V as well as 100 V piezo excitation. Actually, the curves seem to coincide even better for the thicker tagging. A possible explanation could be a slightly different arrangement of the contact wires that suppress the evolution of inductions. Only the formerly mentioned shift due to the agitating voltage is observed. In the phase measurements, however, also the differences for varying piezo agitation vanish and all curves coincide quite well (Fig.55b) For better identification, the phases belonging to an agitation of 50 V and 100 V have been shifted by 200°.

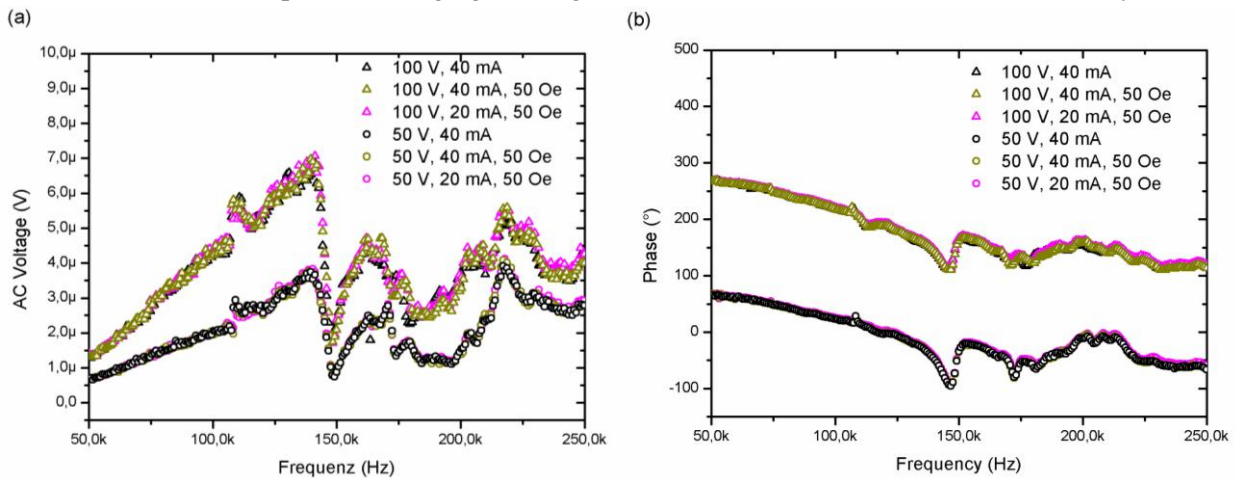


**Figure 55:** Sensor output voltage (a) and corresponding phase shift relative to the piezo excitation (b) of the Zn NW sample tagged with 350 nm of CoFe as a function of frequency.

Fig. 58 shows an SEM image of an oscillating Zn NW agitated by the electron beam. The NW is oriented perpendicular to the substrate. At perpendicular orientation, the tip experiences two approaches and withdrawals with respect to the substrate surface during one period of oscillation. Thus, in the drawn scenario the magnetic detection of the NW movement is best performed at twice the agitating frequency (2<sup>nd</sup> harmonic). Respective results of a plain Zn NW sample (reference curves, empty symbols) and the same sample coated by 150 nm of CoFe (solid symbols) are shown in Fig. 56. However, no additional

effects but the already mentioned ones can be observed. Owing to the required re-contacting following tag deposition, the signal amplitudes for the reference and the tagged device differ from each other. For scenarios in which the majority of the NWs are tilted relative to the substrate normal, however, the major signal is expected at the agitating frequency (first harmonic). As can be seen from Fig. 53b, the latter scenario is most applicable to our situation.

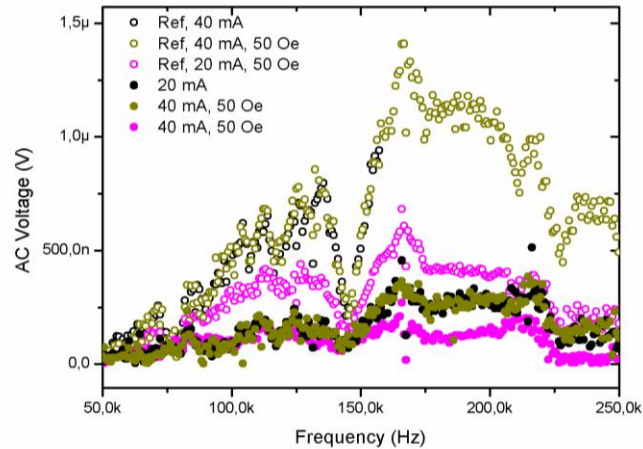


**Figure 56:** AC sensor voltage recorded at twice the agitation frequency (second harmonic) for a tagged Zn NW device (150 nm CoFe, solid symbols) and for the untagged reference case (empty symbols).

Next, the device response of an agitation in the sensor plane is presented. The piezo excitation is carried out at 50 V. Fig. 57 shows respective data for Zn NWs with 150 nm CoFe tagging (solid symbols) together with reference data (same sample with no tagging, empty symbols). For better clarity in the figure display, the reference data is shifted upwards by 4  $\mu\text{V}$  (a) and 200  $^\circ$  (b) respectively. Likewise to the case of perpendicular piezo excitation described above, smaller peaks between 75 kHz and 150 kHz can again be ascribed to induced currents. Since no other curve splitting is observed, no evidence for the aimed magnetic detection is present.

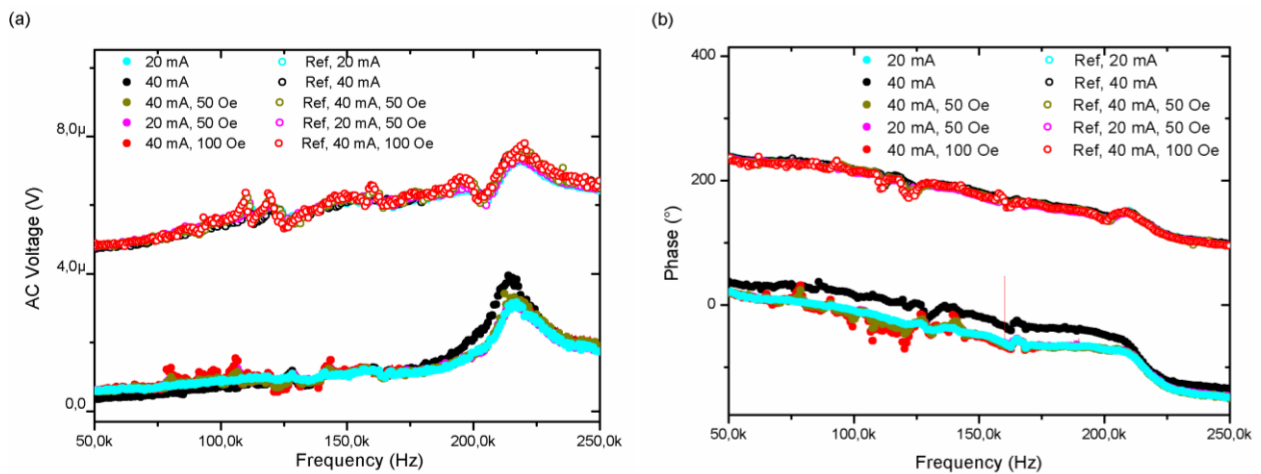


**Figure 57:** Voltage (a) and corresponding phase (b) of the Zn NW sample tagged with 150 nm of CoFe (solid symbols) and the reference state without tagging (empty symbols) as a function of frequency under agitation in lateral x-direction.



### 5.1.1 Mechanical properties and resonance behavior

In contrast to semiconducting NWs [130, 131], there are only few reports on the mechanical properties of Zn NWs. Despite of its small dimensions and the characteristic crystalline structure, it is expected to be less brittle compared to semiconductors. However, for large stresses one has to consider plastic deformation typically experienced for metals. In the elastic regime, on the other hand, the crystalline nature of the NW increases the stress the structures endure due to a decreased crack length. For the oxide of Zn, it is reported on a lowering of the *Young's* modulus (~100 GPa) for NWs compared to the bulk value by up to 30 % [130]. Fig. 58 shows a Zn NW brought to oscillation by the imaging electron beam in a scanning electron microscope. Derived from elastic beam theory [132], the resonance frequency of a NW with one end ideally fixed and the other end free is given by:

$$f_n = \frac{\beta_n^2 d}{2\pi l^2} \sqrt{\frac{E}{16\rho}} \quad (5.2)$$



**Figure 58: SEM image of an oscillating Zn NW, agitated by the imaging electron beam.**

with  $n$ ,  $\beta$ ,  $d$ ,  $l$ ,  $E$  and  $\rho$  being mode index, eigenvalue of the respective characteristic equation [132], diameter, length, *Young's* modulus and density. Obviously, the oscillation is strongly affected by the aspect ratio of the beam. Inserting the measured wire dimensions from Fig. 58 into (5.2), its first resonance is expected at approximately  $f \approx 718$  kHz ( $l=13.6$   $\mu\text{m}$ ,  $d=250$  nm,  $E=103$  GPa [133] and  $\rho=7140$  kg/m<sup>3</sup>). Besides internal friction, NW oscillation is mainly determined by damping of the surrounding medium, and quality factors depend strongly on the ambient pressure [134]. The force necessary to bend a NW is – depending on its mechanical properties and dimensions – expected in the range of nN [90]. The simple harmonic oscillator can be described by the following differential equation:

$$\ddot{x} + 2\gamma\dot{x} + \omega_0^2 x = X_{ext} . \quad (5.3)$$

Thereby, velocity proportional Stokes friction with damping coefficient  $\gamma$ , the angular frequency  $\omega_0$  as well as an inhomogeneous term  $X_{ext}$  for the external agitation is taken into account.

### 5.1.2 Resonance behavior by means of finite element analysis and SEM characterization

Up to now, the bending of NW tips towards the sensor surface has not been modeled. From (5.2), it is obvious that the most important parameter determining the resonance frequency is the length of the NW, which enters inversely squared. With the aid of FEM analysis<sup>19</sup>, the resonance behavior of a typical Zn NW (as-deposited and with tagging) is investigated. As boundary setting, the only constraint is the fixation at the bottom end of the structure. The first mechanical resonance mode of a 10  $\mu\text{m}$ -long NW with a diameter of 250 nm amounts to 1.68 MHz as indicated in Fig. 59a. The tagging is mimicked with

<sup>19</sup> Comsol multiphysics software version 3.4 and MEMS module with 3D eigenfrequency analysis based on the elastic beam theory is used.

an additional “subdomain”, i.e. a cylindrical ring of cobalt, which lowers this resonance to 622 kHz (Fig. 59b). The respective material parameters are density and *Young’s* modulus (according to (5.2)). The length of the ring is chosen to 4  $\mu\text{m}$  and the thickness to 150 nm as indicated in Fig. 59b.

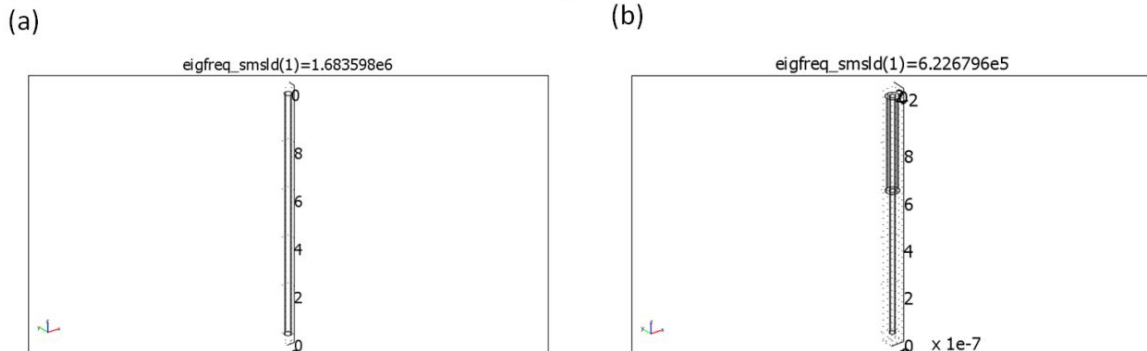


**Figure 59:** Calculated resonance frequency by FEM analysis for an as-deposited Zn NW with a length of 10  $\mu\text{m}$  and a diameter of 250 nm (a). Same NW with an attached Co cylinder ring (length: 4  $\mu\text{m}$  and thickness 150 nm) to mimic the tagging (b). The calculated resonance frequencies are indicated at the top in Hz.

Despite of this remarkable decrease, the resonance of the tagged wire is still beyond the experimentally accessible frequency range. In addition, the situation depicts an ideal case since in reality the coating will somewhat extend to the NW root without being homogeneously distributed around the NW. A homogeneous coating with cobalt metal which covers the whole wire surface would result in an increase of resonance frequency to 3.69 MHz due to a larger effective diameter.

In order to get deeper insight into the agitation, the shear piezo actuator is mounted to the respective chuck and loaded in a “Zeiss Neon 40XB” SEM (Fig. 60a). All necessary electrical connections have been fed through. The red wire in Fig. 60a serves as connection to earth ground. Fig. 60b depicts conductive silver paste at the side edge of the stack when inclined by 68° relative to the electron beam. A chosen vertical piezo agitation of 50 V at 140 kHz results in an extension of 50 nm. In the “frame averaging” mode, this value can be directly extracted from the SEM image. When corrected for the inclination, it indeed amounts to ~54 nm (=50 nm / cos (90°-68°)).

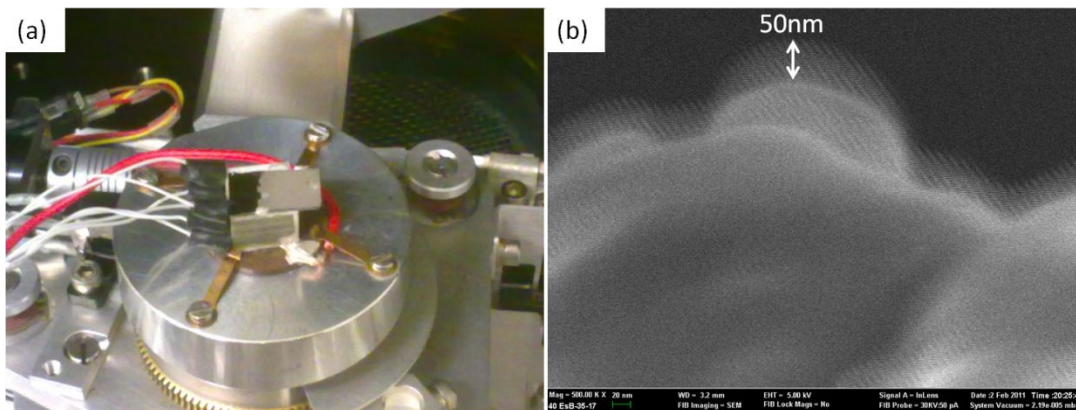


**Figure 60:** Shear actuator, mounted inside a SEM (Zeiss Neon 40XB) (a). A sample partly coated with Zn NWs is fixed on top. A fraction of conductive silver paste on the sample edge under vertical agitation at 140 kHz and a peak-to-peak voltage of 50 V is shown in (b).



It is expected that the piezo extension is hampered by additional mass (usually  $\sim 0.5$  g) from the sample. In the following, the difference in extension of the substrate and the NW tip is examined. In Fig. 61(a) and (b), a structure on the substrate surface is depicted at rest and agitated vertically at 140 kHz by 250 V piezo drive voltage, respectively. Upon agitation, the measured width increases from 50 nm to around 65 nm. The resulting difference of 15 nm can be compared to that experienced by a NW tip in order to assess its oscillation behavior. In Fig. 61 (bottom), the tip of a strongly tilted NW (length: 8.7  $\mu\text{m}$ , diameter: 190 nm) which has been coated with 60 nm CoFe is again shown at rest (c) and agitated like mentioned above (d). Its extension and oscillation amplitudes add up to  $\sim 80$  nm. Though this value is significantly larger than that for the structure on the sample surface, it is still small with regard to a magnetic detection of such deflections.

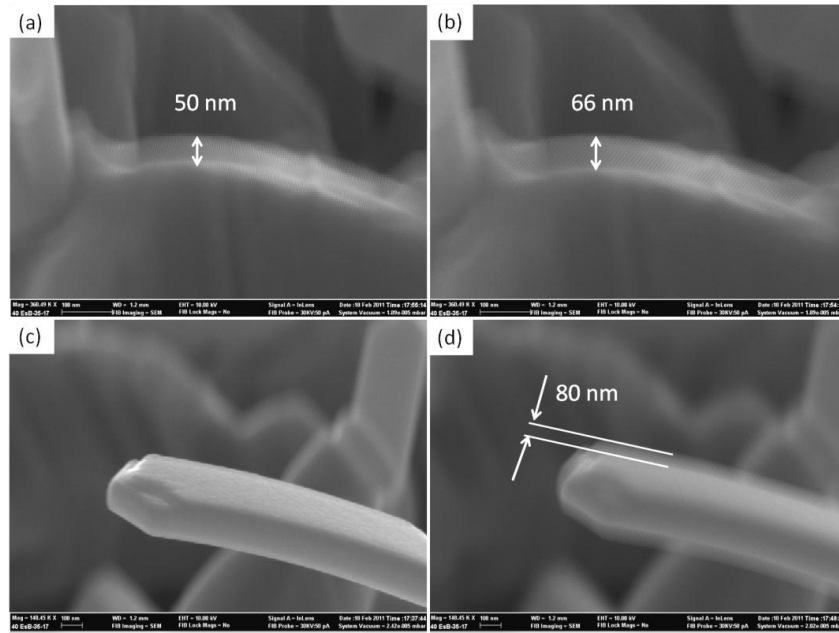


**Figure 61:** Surface feature at rest (a) and under agitation at 140 kHz (b). Tip of a NW on the sample at rest (c) and agitated (d), respectively.

The reason for the small value is the resonance frequency of the structure, which is approximated to 2.6 MHz according to (5.2). Owing to the fairly broad spread of NW sizes arising from the self-assembled growth, also the resonances cover a broad range. The tagging applied in the experiments, however, was thicker than that of the wire in Fig. 61(c) and (d). The SEM examination, on the other hand, is performed under high vacuum conditions. Hence, under atmospheric conditions there will actually be much stronger damping of the wire oscillation, which further hampers the tip deflections.

### 5.1.3 Conclusion

In conclusion, the difficulty in the magnetic detection of NW oscillations has multiple reasons. At first, the NW geometries can only marginally be tailored towards low resonance frequencies due to the self-assembled nature of the growth (see section 4.2.1). Furthermore, only the wire fraction which is aligned oblique will potentially contribute to the “mechanosensing”. The tagging which is performed via sputter-coating (see section 4.3), however, further stiffens the structures, provided it is applied to the wire as a

whole and not only to the tip. Finally, the maximum amount of magnetic material deposited onto the Zn NW samples ( $\sim 350$  nm CoFe) is insufficient to produce a measurable signal in the GMR sensor when taking into account the small oscillation amplitude and the large distances of several micrometers (see Fig. 53b). Thus, the main drawback for the Zn NW system is given by the stiffness of the wires and the limited agitation frequency range, which in combination results in too low amplitudes of the magnetic tagging to be measured by the embedded GMR sensor.

## 5.2 Germanium nanowires

Ge NWs possess smaller dimensions compared to the investigated Zn structures. The morphologies, however, suffer from a distinct crystallite background as can be seen in Fig. 62a. As mentioned above, this is attributed to a lowered synthesis temperature of  $310^\circ\text{C}$ . An optimal NW yield with little crystallites is achieved closer to the eutectic point at  $340^\circ\text{C}$  (see Fig. 38d). From the inset of Fig. 62a, the resulting NW dimensions as well as their conical shape become obvious.

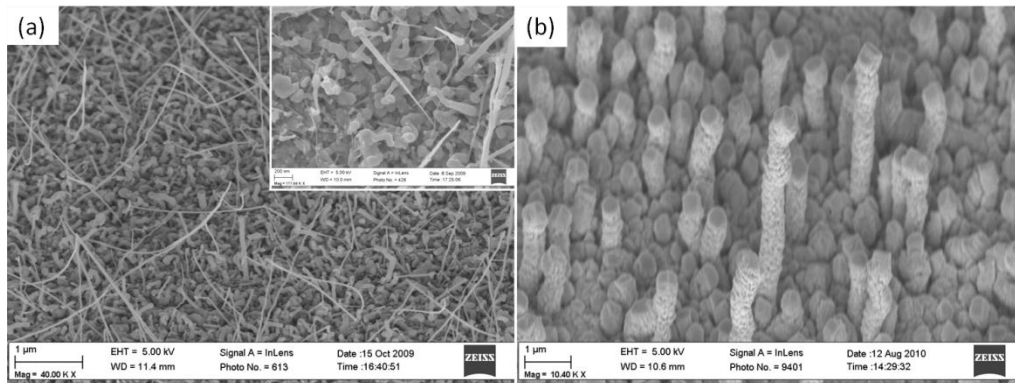


**Figure 62:** SEM images of as-deposited VLS-grown Ge NWs grown at  $310^\circ\text{C}$  (a) and with a 100 nm CoFe tagging (b) recorded under an  $40^\circ$  tilting angle. The deposition leads to a perpendicular alignment of the wires with respect to the substrate surface (b).

The GMR sensor for the examined device showed a GMR effect of only 5.1 % following NW synthesis (zero field DC resistance  $10.6\ \Omega$ , saturation field  $\sim 100$  Oe). In the as-deposited state before NW synthesis, the GMR effect was more than 10 %. The decrease is attributed to thermal effects such as layer interdiffusion during NW synthesis (see section 4.1).

The measurement parameters are chosen similarly to those set for the Zn NW sample. However, lock-in sensitivity and integration time are set to  $20\ \mu\text{V}$  and 7.5 s respectively. Fig. 63 shows data for the Ge NWs with 100 nm thick CoFe tagging (reference data not shown), the corresponding morphology of which is depicted in Fig. 62b. Besides different curve characteristics due to slightly different device dimensions and contacts, a current “branching” appears, which is already known from Fig. 52, 54 and 56 (compare pink and bright blue data from this plot with black, red and brown data in previous graphs). The phases belonging to agitation voltages of 50 V and 100 V are separated by  $400^\circ$  for the sake of clarity in Fig. 63b. Since no reference data has been recorded for this sample, the interpretation of the results is not straightforward. Nevertheless, the observed effects are similar and seem closely related to the ones explained in section 5.1.

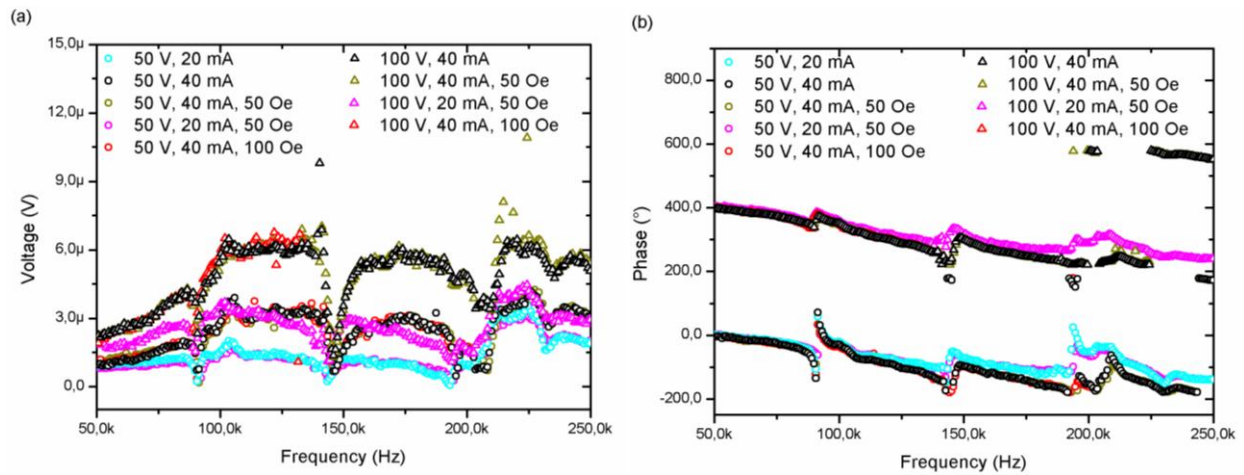


**Figure 63: Voltage (a) and corresponding phase (b) of the Ge NW sample tagged with 100 nm of CoFe as a function of frequency in z-agitation.**

Finally, FEM calculations to assess the Ge NW resonance frequencies are adducted. The approach is the same as the one employed for the Zn NWs. Due to the tapering of the structures and their smaller dimensions (especially the length), a cone-shaped Ge NW with a length of 4  $\mu\text{m}$  and a root diameter of 150 nm is assumed which possesses its first mechanical resonance at about 12.5 MHz (Fig. 64a). This is nearly one order of magnitude larger than that of a typical Zn NW. The dimensions are again chosen to be characteristic for the distinct spread of NW lengths and diameters that originate in the self-assembled growth. A cylinder mimicking the tagging with a length of 2  $\mu\text{m}$  and a radius of 150 nm is applied in the model as depicted in Fig. 64b. Although it lowers the resonance by nearly one order of magnitude to 1.41 MHz, the situation is again oversimplified since the NWs are actually coated completely.

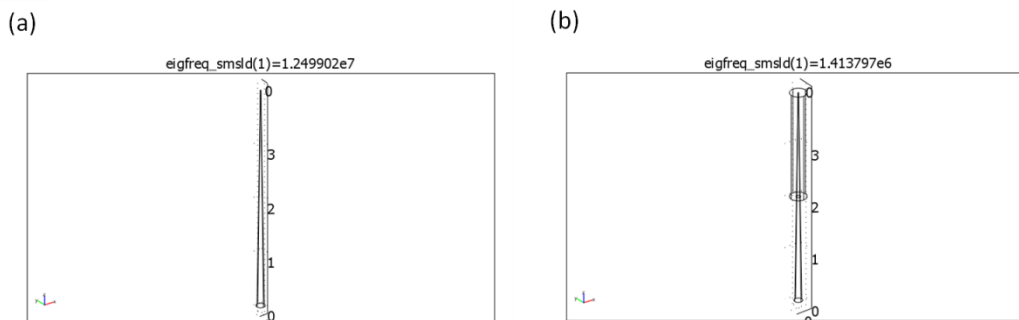


**Figure 64: Calculated resonance frequency by FEM for an as-deposited Ge NW with a length of 4  $\mu\text{m}$  and bottom diameter of 150 nm (a). Same NW with attached Co cylinder (length: 2  $\mu\text{m}$  and radius 150 nm) to mimick the tagging (b). The respective resonance frequencies are indicated at the top of the images.**

Taking into account the downgraded GMR amplitude, the unfavorable NW morphology and the inaccessible resonance frequencies (even higher than for Zn NWs), the germanium system is regarded as inappropriate for the intended purposes.

### 5.3 Polypyrrole nanowires

The polymeric structures introduced here feature a growth mechanism that does not require any template nor seeded or patterned surface and works at room temperature via electro-polymerization [124]. PPy is a high-melting, electro-active and flexible polymer with mechanical properties close to those of biological tissue. Furthermore, it is known to be robust and stable to organic solvents. The *Young's* modulus of PPy nanostructures amounts to  $\sim 0.96$  GPa [135]. Although the NW dimensions can hardly be influenced experimentally, the obtained morphology is promising for the intended purpose in terms of density, length and homogeneity (Fig. 41b). Prior to the self-assembled NW formation, an insulating layer of overoxidized PPy is generated. The thickness of this layer amounts to less than 100 nm, which favors the proximity of the NW array to the underlying sensor.

In the present study, the readily processed device possesses a magnetoresistance of around 8 % and a saturation field of 150 Oe (see Fig. 65). The sensor area is about 15 mm x 5 mm and its zero field DC resistance is about 10  $\Omega$ .

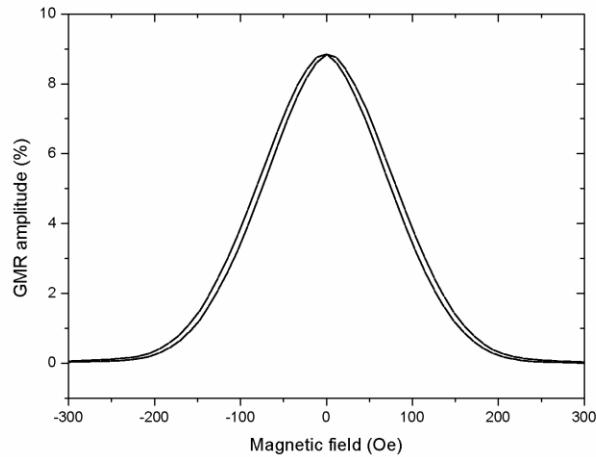


**Figure 65: GMR response curve of the device.**

The deterioration of the GMR amplitude from about 12 % for the as-deposited sensor can most likely be attributed to oxidation during the NW synthesis. Like in the previous sections,  $\text{Co}_{50}\text{Fe}_{50}$  is used for the magnetic tag. In order to allow for a comprehensive investigation of the performance and to assess the optimal thickness/amount of material, the metal is sputtered in a series of various thicknesses, namely 50, 100, 300 and 600 nm on a single sample. This allows for the comparability of measurements that are performed directly after each deposition step. During the series of measurements, the GMR of the device decreased from 8.87 % for the reference to 8.05 % (in the case of the 600 nm tagging) due to shunting effects. Figure 66 shows a row of top-view SEM images in which the amount of deposit is increased from 50 nm (a) over 300 nm (b) to 600 nm (c).

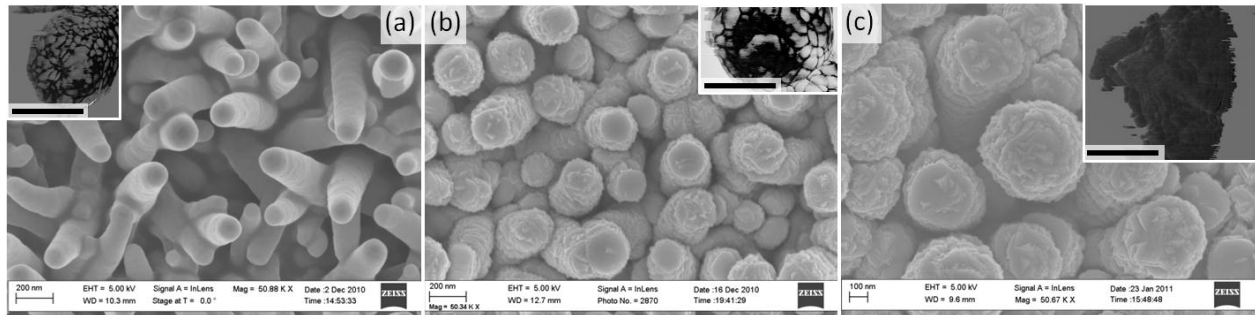


**Figure 66: Top-view SEM images of PPy NW cilia coated with 50 (a), 300 (b) and 600nm CoFe (c). The insets show magnetic contrast of one representative NW by means of MFM, respectively. The scale bars correspond to 200 nm.**

The insets in the SEM images represent magnetic contrast images performed by MFM of an individual NW with the respective tagging. Bright and dark sites reflect regions on the surface with the magnetization pointing in and out, respectively. As the coating thickness increases, the magnetic contrast turns from an initial multi-pole state to a condition with a single predominant magnetization direction. While in the low thickness regime, the NW roughness favors the formation of domain walls within the tag layer, a tag thickness beyond 300 nm leads to a homogeneous magnetization along the NW long axis, resulting in uniform MFM contrast when imaged at the tip. This behavior can be explained by (i) a smoother coverage (compared to (b)) that suppresses local stray fields and (ii) a larger magnetic moment.

For the measurements, an agitating voltage of 50 V is applied with an adjusted lock-in sensitivity and integration time of 20  $\mu$ V (70 dB) and 12.5 s, respectively. In Fig. 67, the AC output voltage (black data) of the sensor as well as the respective phase (red data) is plotted against the excitation frequency in a range between 188 kHz and 200 kHz, which turned out to be the important frequency range.

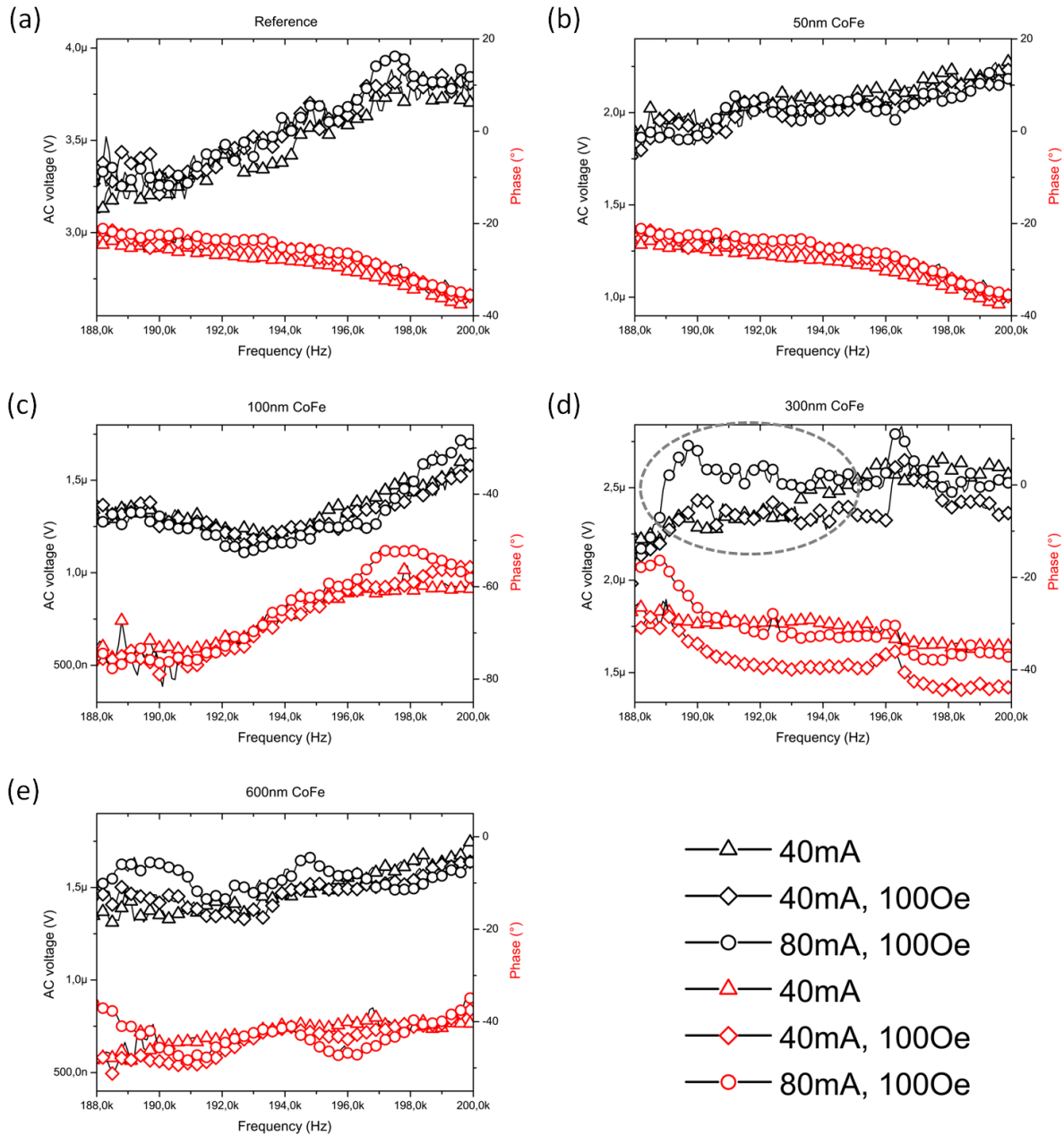


**Figure 67:** AC voltages (black) with corresponding phase (red) angles as a function of the agitation frequency parameterized by the applied in-plane current and the external z-field. Reference data are displayed in (a). A series of measurements with a tagging thickness of 50, 100, 300 and 600 nm CoFe is shown in (b), (c), (d) and (e), respectively.

Though the measurements of only one single device are presented, other devices with different tagging thicknesses behave similarly with a slightly shifted operating frequency. The reason why the scope is limited to this single device is given by the fact that consecutive deposition and measurement of increasing layer thicknesses have only been realised for this sample. Five different situations are depicted, namely the reference one (device without tagging in (a)) and those of the same device coated with 50 (b), 100 (c), 300 (d) and 600 nm of  $\text{Co}_{50}\text{Fe}_{50}$  (e). For each set, a reference curve at 40 mA sensor current without an external magnetic field is taken (triangles). Next, a magnetic field of 100 Oe in magnitude is applied perpendicular to the sensor plane in z (rhombs). In each of the third recorded data tracks, the sensor current is doubled to 80 mA (circles). When focusing on the reference data of Fig. 67a, a good

coincidence of the three curves within a small noise level<sup>20</sup> becomes obvious. In contrast to the results for germanium and zinc, this presents a good prerequisite in order to identify signals which potentially attest a proof of the investigated principle. Between the diagrams of different tagging thicknesses, there are again non-systematic signal variations present that arise from the reestablished contacts. Like the reference data, also the spectra from Fig. 67 (b) and (c) basically coincide. This suggests that tagging thicknesses of 50 nm and 100 nm are obviously insufficient for the detection.

Only the data sets for the 300 nm and 600 nm thick coating show a distinct branching between the different states (see dashed ellipse in Fig. 67d). Since these curves differ in dependence of the current applied to the sensor, the observed splitting can be attributed to changes in the sensor magnetization configuration caused by contributions of the magnetized oscillating NW array. For the 300 nm coating, one can clearly observe that a current of 80 mA results in the highest signal voltage, which is expected for magnetic interactions between the coating and the sensor. While a curve splitting is still observed for the 600 nm thick coating, it is already less pronounced compared to the 300 nm thick coating, which can be attributed to the onset of nanowire conglomeration (see section 7).

The phase shift data basically shows the same dependence on the coating thickness as analyzed in terms of the amplitude evolution. Under these conditions, the whole elongated NW array including the tag layer can be regarded as a driven oscillatory system with defined phase lag relative to its agitation. Thus, a coating thickness of about 300 nm is regarded as ideal for observing magnetic interactions of the tagged NW array onto the sensor layer in this setup. The reproducibility of the results in the given frequency range is guaranteed, since single measurement runs have been repeated reproducibly. The morphology of the tagged NWs has been examined regularly between the various agitation and deposition steps by means of SEM. It turned out that no structural change has been observed as a consequence of the agitation. Moreover, a series of EDX investigations have been carried out in order to rule out substantial oxidation of the  $\text{Co}_{50}\text{Fe}_{50}$  tagging. The sample plane was perpendicular to the direction of incidence of the electrons, and a tagged nanowire region (600 nm tag thickness) of about  $90 \mu\text{m}^2$  was examined at a magnification of 10.000 and a 10 mm working distance. In order to obtain depth resolution, a series of increasing accelerating voltages has been applied (1.5, 2.5, 5, 10, 15 and 20 kV). The higher the voltage, the deeper is the penetration of the beam and the respective x-ray analysis. With increasing accelerating voltage, the oxygen content first decreases from  $\sim 17.3$  to  $\sim 8$  at. %, then rises again to  $\sim 12.5$  at. %. The decrease indicates that the oxidation is only superficial. Since the rise of oxygen content is also accompanied by a rise of carbon ( $\sim 11$  at. % at 20 kV) and silicon ( $\sim 4$  at. % at 20 kV), part of the signal at higher accelerating voltages already stems from the underlying polymer and substrate material. In the bulk tag material, which is seen at around 5 kV accelerating voltage, the following atomic element percentages have been obtained: C (5.62 %), O (8.21 %), Si (1.05 %), Fe (42.17 %) and Co (42.95 %). Since the abundance of Co and Fe of  $\sim 42$  at. % each, are almost equivalent ( $\text{Co}_{50}\text{Fe}_{50}$  alloy) and oxygen is only present with  $\sim 8$  at. %, these results confirm only superficial oxidation.

Also for a PPy NW with reasonable average dimensions in the as-deposited and tagged state, representative resonance frequencies are calculated by means of the FEM model mentioned in section 5.1.1. The structure from Fig. 68a possesses a length of 1  $\mu\text{m}$  and a diameter of 100 nm. Its lowest resonance of  $\sim 15$  MHz (Fig. 68a) is lowered to about 1 MHz (Fig. 68b), when a tag of a cylindrical Co head with a rounded tip, a length of 800 nm and a radius of 150 nm is attached as indicated in the figure.

---

<sup>20</sup> Noise sources include Brownian mechanical noise from air damping and electronic noise from the readout circuit.

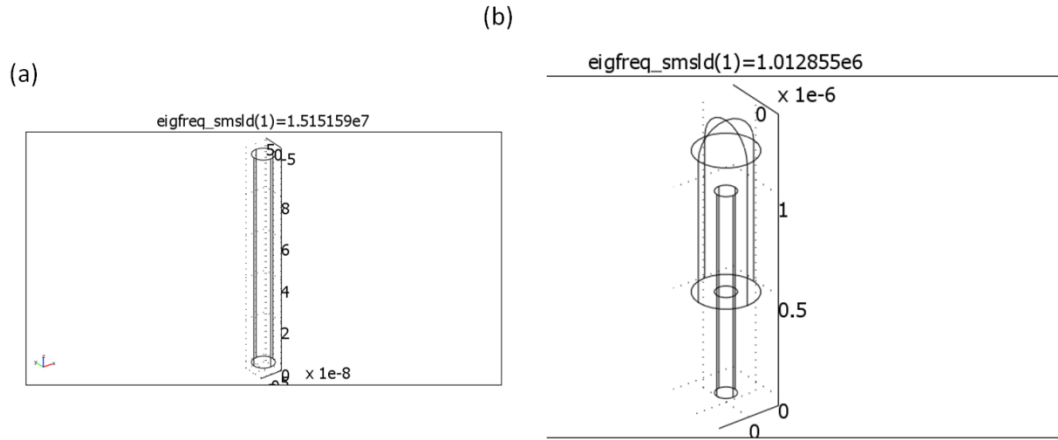


**Figure 68:** Calculated resonance frequency by FEM for an as-deposited PPy NW with a length of 1  $\mu\text{m}$  and diameter of 100 nm (a). Same NW with attached Co head (length: 800 nm and radius 150 nm) to mimick the tagging (b). The respective resonance frequencies are indicated at the top of the images.

Judging from these FEM-simulation results, the lowered resonance would still reside in a range that is experimentally inaccessible. Due to the - at least to a certain extend - flexible structure of PPy, the mode of oscillation of the NW array can be regarded as damped rather than resonant (see section 7).

## 5.4 E-beam resist nanorods

In this section, measurements of a device equipped with the lithographically synthesized “artificial cilia” from section 4.2.4 are presented. The approach has been intended to overcome the difficulties of random growth that are intrinsic to NW self-assembly (see section 5.1 and 5.2). The advantage is the possibility to tailor density and mutual distance of the structures.

The meanders mentioned in section 4.2.4 possess dimensions of  $450 \times 142 \mu\text{m}^2$  and  $450 \times 48 \mu\text{m}^2$  with trace widths of 5  $\mu\text{m}$  and 3  $\mu\text{m}$ , respectively. The corresponding fabrication process is outlined in Appendix D. Fig. 69(b) and (c) show the rod array covering the meandered sensor ( $450 \times 142 \mu\text{m}^2$ , trace width: 5  $\mu\text{m}$ ). The e-beam writing is carried out by dividing the target area into square-shaped arrays with sizes of maximal 100  $\mu\text{m} \times 100 \mu\text{m}$ . In order to cover the whole meander,  $7 \times 6 = 42$  adjacent fields are scanned with a resulting overall area of 0.42  $\text{mm}^2$ .

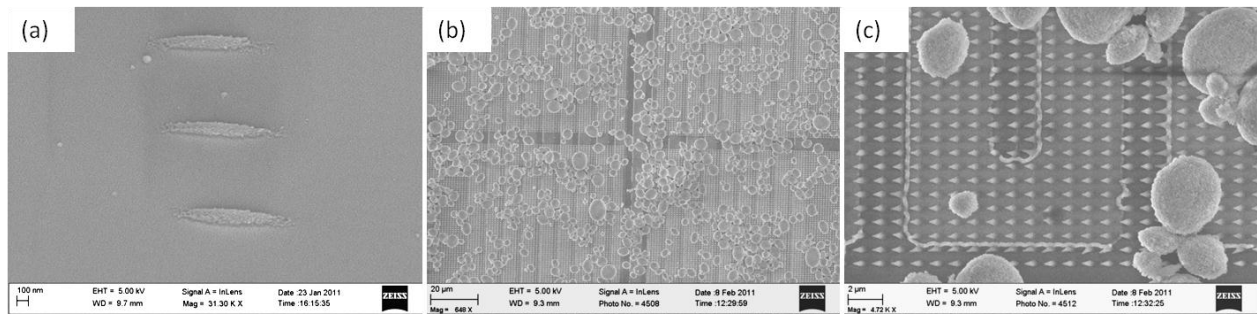


**Figure 69:** E-beam structured NWs coated with 100 nm CoFe (a). The deposit pulls the structures to the substrate surface. Top view images of the array, meander and beads at different magnifications (b, c).



Like already mentioned in section 4.3.4, an alternative tagging to the sputter-deposited CoFe layer is also tested for the E-beam structured NWs, which is given by superparamagnetic beads (“Bioclone BcMag”, silica-coated iron oxide, diameter: 5  $\mu\text{m}$ , COOH-termination, magnetization: 40-45 kA/m) pipetted onto the array at a concentration of 1600  $\mu\text{g/ml}$ . The beads are supposed to affect the GMR meander locally by their induced stray fields, provided an external magnetizing field is applied. The particles have been pipetted (see Fig. 69d) only after the sample was mounted to the measurement setup. Owing to the meander-shaped pattern of the sensor, a resistance of about 7 k $\Omega$  evolves. The response curve shown in Fig. 70 reveals a GMR amplitude of 11.5 % at a saturation field of approximately 100 Oe (in-plane field applied parallel to the long meander axis).

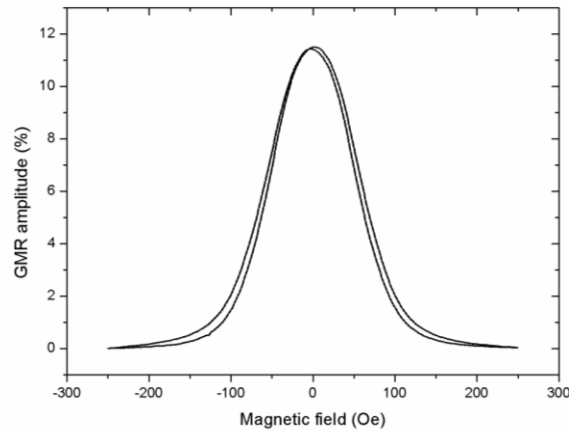


**Figure 70: GMR response curve of the structured sensor.**

Reference measurements are carried out without beads. Fig. 71 depicts the sensor’s AC output voltage (a) as well as phase angle (b) as a function of frequency between 120 k Hz and 250 kHz. Piezo agitation is adjusted to 100 V, while the lock-in integration time is 12.5 s. All other parameters are adjusted like described in section 5.1. The voltage signals are, owing to the increased sensor resistance, significantly larger than those obtained for samples with an un-patterned sensor and decrease from about 600 mV at 120 kHz to ~ 130 mV at 250 kHz (see Fig. 71a). The in-plane sensor currents are set to 0.5 mA and 1 mA. However, also the orange and green curves which exhibit data of the device with applied superparamagnetic particles as well as an external magnetic field with a magnitude of 100 Oe, are located within the noise level of the reference curves, there is no evidence for any signal originating from an approach of the particles. Accordingly, also the phases (Fig. 71b) coincide quite well (the strong shift at 160 kHz is a result of the lock-in output switching reference points from  $-180^\circ$  to  $+180^\circ$ ).

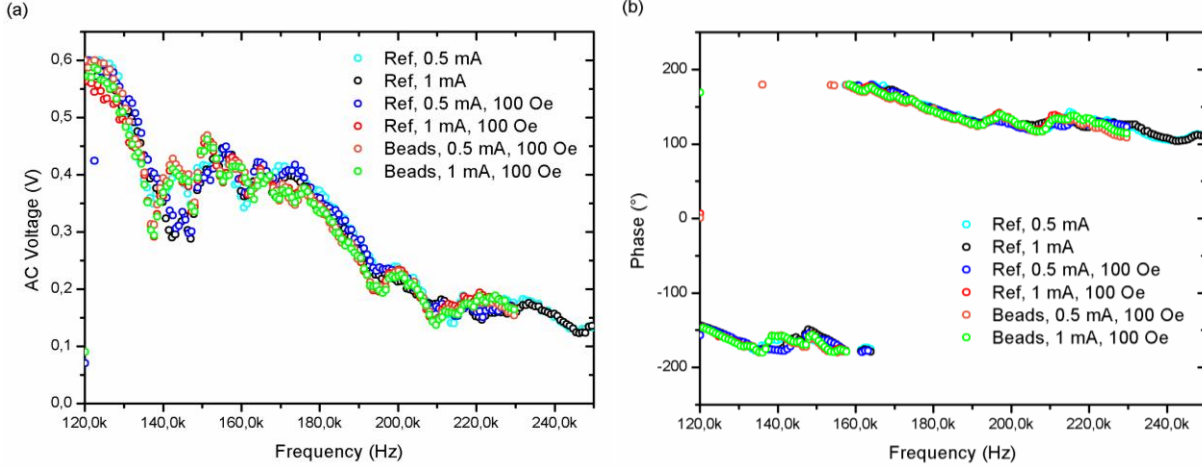


**Figure 71: AC voltage (a) and corresponding phase (b) of the e-beam written array as a function of frequency from 120 kHz to 250 kHz.**

To explain the absence of signals originating from the array it has to be stated here that unspecific binding of the beads to the rod array is assumed. The bond forces involved range roughly from femto to several hundred piconewton [129]. Consequently, those forces are smaller than the inertial forces exerted by the bead mass sitting on top of the rods<sup>21</sup>. Hence, there is a certain risk for the beads to get detached from the nanorod array during agitation. Moreover, the magnetization of the “Bioclone” beads at an external field of only 100 Oe (5-10 kA/m) is supposed to be insufficient (see the simulation results in section 6.4).

The resonance behavior of the resist structures is again calculated according to the FEM model presented in section 5.1.1. Young’s modulus and density of the resist structures are modeled with  $E=200$  MPa and  $\rho=1000$  kg/m<sup>2</sup>, respectively. Fig. 72 shows the drawn cone with dimensions resembling the original rods, namely a length of 1  $\mu\text{m}$  and base and tip diameter of 200 nm and 100 nm respectively. As indicated, the first resonance is located around 16 MHz, which is far beyond the scope of the measurement setup.

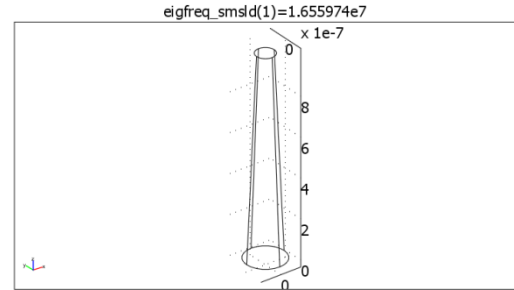


**Figure 72: FEM-calculated resonance frequency for an as-deposited resist rod with a length of 1  $\mu\text{m}$  and diameters of 200 nm (base) and 100 nm (tip).**

## 6 Micromagnetic simulation

By means of the OOMMF (object-oriented, micro-magnetic framework) software from *NIST* (National Institute of Standards and Technology, USA), interactions of magnetic moments and fields can be modeled on the microscale. Considering different energy terms, a variety of micromagnetic problems are solved with the aid of the *Landau-Lifshitz-Gilbert* equation,

$$\frac{\partial M}{\partial t} = -\gamma M \times H_{eff} + \frac{\alpha}{M_s} \left( M \times \frac{\partial M}{\partial t} \right), \quad (5.5)$$

<sup>21</sup>Gravitational forces of the “Bioclone” beads amount to 2-3 pN (see also section 7).

which describes the temporal change of magnetizations  $M$  with the aid of an effective field  $H_{eff}$  and the gyromagnetic ratio  $\gamma$ . Thereby,  $a$  and  $M_s$  represent the damping parameter and the saturation magnetization, respectively.

## 6.1 OOMMF model

In this chapter, the influence of spherical magnetic particles on the GMR amplitude of embedded sensors is simulated and parameterized by the distance from the particle center to the sensor surface. To that end, the multilayer sensor is simplified by a NiFe(2 nm) / Cu(2 nm) / NiFe(2 nm) tri-layer system. The tagging is adopted by dipolar  $\text{Co}_{70}\text{Fe}_{30}$  particles, which are assumed to be magnetized to saturation (1650 kA/m [136]) along the vertical axis (perpendicular to the sensor plane). In the model, the polycrystalline metal layers comprising the sensor are divided into 20 nm x 20 nm x 2 nm cells. In addition to the Zeeman coupling, the demagnetizing energy, the exchange coupling contribution of 6 nearest neighbors (exchange constant  $A=13$  pJ/m [61]) and the interlayer exchange coupling are also included in the model. The effective exchange coupling  $J^*$  is determined according to  $J^*=2J_Q+J_L= -7.74 \mu\text{J}/\text{m}^2$  from the linear and biquadratic coupling strengths  $J_L$  and  $J_Q$ , which are obtained from the measured GMR response by the *downhill simplex* fitting procedure, which is described in the PhD thesis of Volker Höink (chapter 2.7.2) [137]. Since the sensor is reduced to a tri-layer system, the resulting value represents twice the value for the antiferromagnetic coupling strength. Crystalline anisotropy has been neglected due to the vanishing contribution from NiFe ( $K_V=-0.4$  kA/m [61]).

OOMMF solves the problem by calculating the particle stray fields and their impacts on the layer magnetizations in dependence on the vertical distance between the sensor layer and the particles. The stray field created by a single dipolar particle with moment  $\mathbf{m}$  at position  $\mathbf{x}$  is given by [138]:

$$\mathbf{B}(\mathbf{x}) = \frac{\mu_0}{4\pi} \frac{3\mathbf{n}(\mathbf{n}\cdot\mathbf{m})-\mathbf{m}}{|\mathbf{x}|^3}; \quad \mathbf{n} = \frac{\mathbf{x}}{|\mathbf{x}|} \quad (6.1)$$

Due to the strong distance dependence of the stray field strength (6.1), it becomes clear that the beads have to come as close as possible to the sense layer in order to produce strong magnetic stray fields. Based on the magnetization information of the sensor layers and the given GMR amplitude of the device, the relative electrical resistance is calculated for each associate cell element and summed over the whole area. For a detailed description of the resistance calculation, it is referred to the PhD thesis of Jörg Schotter (chapter 5.3) [138]. The stopping criteria for the calculation of the temporal change of magnetization vectors is set to 0.01 °/ns in each stage.

Fig. 73 gives simulations of a series of particles with diameters of 100, 150, 200, 300 and 500 nm approaching the sensor surface from 2  $\mu\text{m}$  to 200 nm. A GMR amplitude of 12 % is assumed for a rectangular sensor element 1  $\mu\text{m}$  x 1  $\mu\text{m}$  in lateral size with the magnetic particle situated in the center at the respective vertical distance. Obviously, the effect for 100, 150 and 200 nm is fairly small (<1%), while a GMR decline of nearly 6 % results from the particle with a diameter of 300 nm. The stray field of the largest particle, on the other hand, causes a complete sensor saturation.

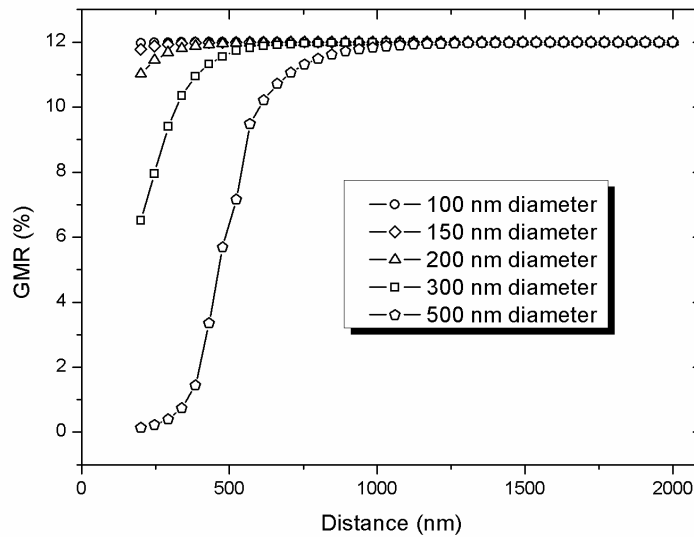


**Figure 73: Simulated GMR response of dipolar CoFe particles with various dimensions as a function of distance from its centers to the sensor surface.**

In the following sections, the presented model is applied to the individual implementations of NWs or nanorods presented in section 4.2.

## 6.2 Polypyrrole nanowires

In order to model the situation of the PPy device, an ensemble of  $3 \times 10$  CoFe particles is approximated (as a whole) to the sensor element from vertical distances of 3000 nm to 800 nm. While the upper limit of separation is chosen large enough to assure vanishing effect of the particles stray fields, the lower limit is derived from damping and mutual NW interactions, which prevent the cilia from approaching the sensor surface any further. A diameter of 300 nm is assumed according to an optimal deposited tagging thickness of 300 nm as confirmed by the measurement results. Fig. 63 shows the simulated GMR response of the ensemble acting on a sensor element of two different sizes. The 3000 nm x 900 nm rectangle refers to the closest packed cubic lattice (see rhombs and bottom left sketch of Fig. 74), while the particles are arranged in the same manner for the larger sensor element (5000 nm x 1800 nm). An approach over the full range which is divided into 220 distance steps (stages) leads to a decline of the sensor's GMR amplitude of 5.6 %. Due to a decreased areal stray field density, this value shrinks to about 4 % if the larger sensor element is adducted. While both data curves coincide for distances which are too large to let the stray field have an effect on the sensor, the saturation sets in earlier for the closely packed ensemble. The slight buckling effect around 1700 nm is reproducible and obviously arises from discrete changes of domain magnetizations. The bottom part of Fig. 74 depicts the stray field effect of the particle ensemble on the magnetization pattern (indicated by arrows) of the sensor in the case of close packaging. Apart from boundary effects that arise since it is not accounted for periodic boundary conditions in the model, the magnetizations of top (red) and bottom (blue) layer are aligned perfectly antiparallel at a distance of 3000 nm (right). For a vertical distance of 800 nm on the other hand (left), there are parallel magnetization contributions present, which explain the obtained GMR decrease. However, parallel magnetization alignment arises predominantly at the element boundaries. Since the assumed sensor element exhibits only

a negligible small fraction<sup>22</sup> ( $2.7 \mu\text{m}^2$  and  $9 \mu\text{m}^2$  respectively) compared to the whole active sensor area ( $70 \text{mm}^2$ ), these boundary effects are supposed to determine the magnetic impact on the sensor in this model and do limit the model's applicability.

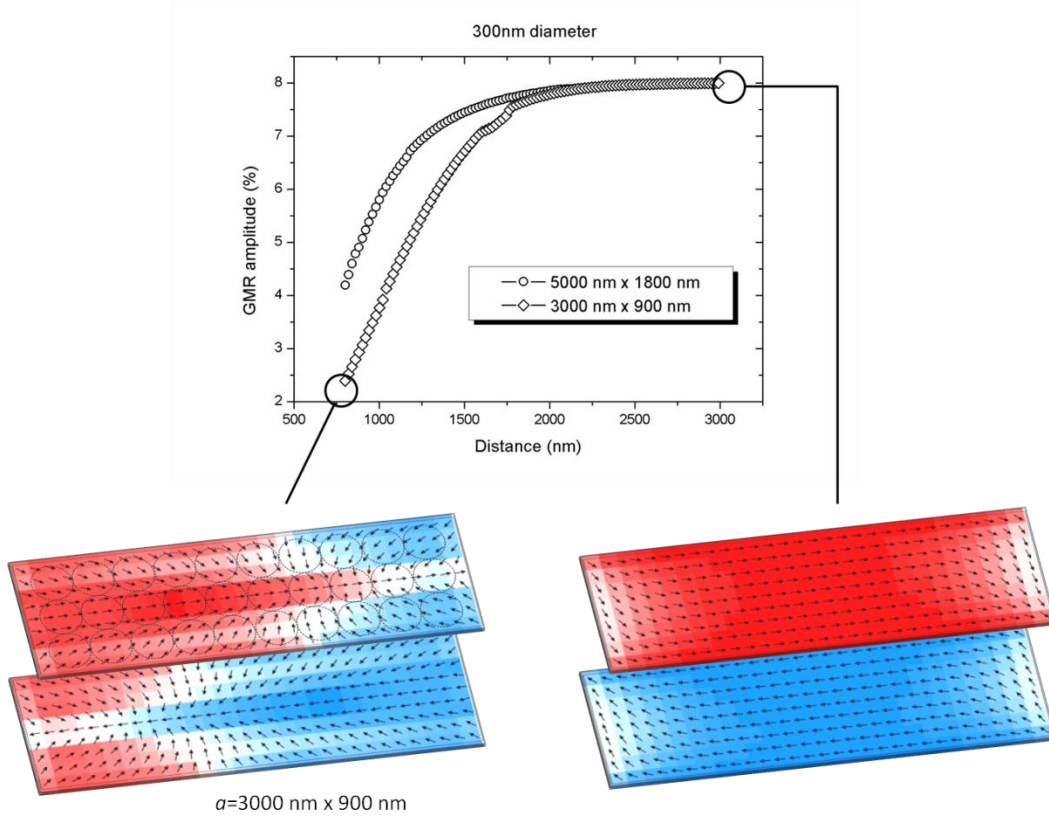


**Figure 74: Simulated GMR response of 30 dipolar CoFe particles (diameter 300 nm) for two different sensor areas as a function of distance from center to the sensor surface. The respective magnetization patterns (arrows) are shown at the bottom.**

In order to create a more reasonable modeling scenario for the PPy device, the contribution of the edge effect is annulated by only taking into account the sensor area claimed by a single NW. By means of SEM and counting over a representative area of  $\sim 100 \mu\text{m}^2$ , the unit area for a single NW is determined to  $A=a^2=300 \text{ nm} \times 300 \text{ nm}$ , with  $a$  being the unit cell size in a cubic lattice arrangement. For the tagging, the nanowire directly within the unit area as well as its eight nearest neighbors are taken into account, with the tagging volume deposited onto a single NW unit area (50, 100, 300 and 600 nm tag thickness, see section 5.3) approximated by a sphere with the same volume. The corresponding sphere diameters are  $\sim 100, 260, 370$  and  $550 \text{ nm}$  (see table 4). Fig. 75 shows the results of the OOMMF simulation for particle diameters of 260 nm and 370 nm. These values describe the effective sphere diameters mentioned above according to a nominal deposition of 100 nm and 300 nm CoFe, respectively. For certain arrangements, it is possible that stray fields generated by adjacent tagging particles compensate each other, thus leading to very low signals compared to single particles modeled on the same sensor region. However, this has been ruled out in the present case, since simulations dealing with nine particles (central one along with its neighbors in a cubic lattice) have always resulted sensor impacts larger than those originating from single particle simulations.

<sup>22</sup> In the present case, element dimensions of e.g.  $18 \mu\text{m}^2$  already lead to calculation times of up to one week (at a processor speed of 3.3 GHz and 24 GB of RAM).

In the diagram in Fig. 75, the resulting sensor GMR amplitude is depicted as a function of the tag distance from 3000 nm to 800 nm according to the model described above. Owing to a larger magnetic moment, the larger particles generate larger stray fields compared to the small ones, thus resulting in signal changes which diminish the original GMR amplitude encountered at large particle distances by around 0.11 %. Though the sensor response to the smaller particles is qualitatively similar, the overall GMR decrease is only 0.017 %. The onset of saturation occurs at lower distances for the smaller particle (1250 nm compared to 1500 nm), which is a result of the lower range of the stray fields from the smaller particles. The impact of stray fields originating from the larger particles (effective diameter of 370 nm) is illustrated by means of the resulting magnetization patterns in the top and bottom layers as indicated by the arrows (see lower part of Fig. 75). The sensor magnetization for vanishing stray field influence is given on the right side (3000 nm particle distance), which shows an antiferromagnetically coupled S-state. No periodic boundary conditions were applied here. For comparison, the left part of the figure shows the situation with the particle at a distance of 800 nm, which reveals the effect of the radially symmetric stray fields of the particles onto the magnetization state of the sensor layers, resulting also in parallel contributions in opposing layer regions. This is indicated by the yellow and violet region, which arises on the right side only in a less pronounced way due to boundary effects. The black circles indicate the vertical projection of the central particle (solid) and those of the neighbors (dashed). The fact that the circle area is larger than the unit cell is counterintuitive and due to the model simplifications, i.e. the introduction of effective diameters. The measured average diameters of the cilia with the respective tagging are listed in table 4.

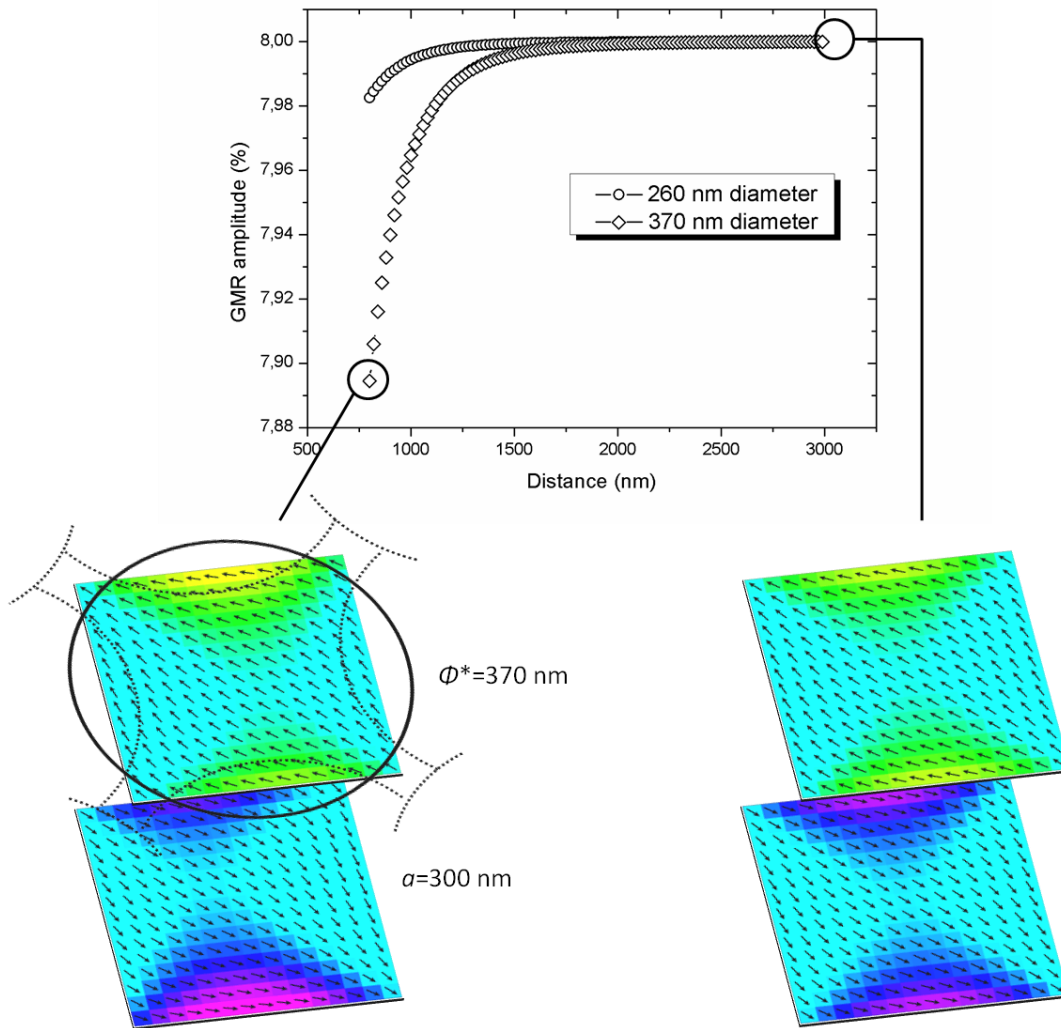
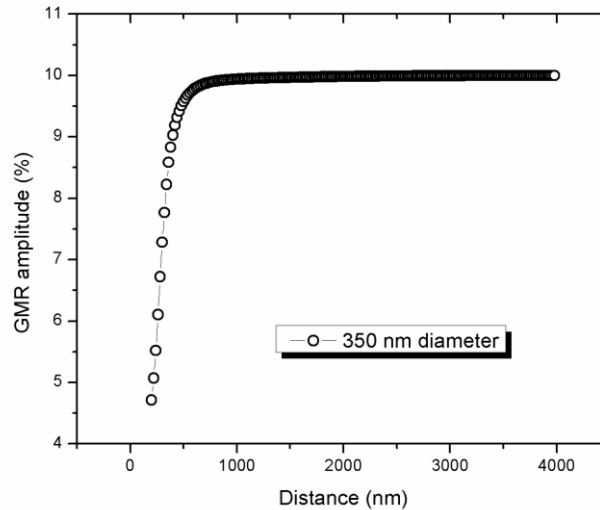


Figure 75: OOMMF simulation of the change in GMR amplitude as a function of the distance from an ensemble of 9 magnetic particles approaching the sensor. The influence of two particle diameters (260 nm and 370 nm) with its stray field acting on a unit cell area is investigated. For the 370 nm diameter particles, the effect of stray fields on the magnetization patterns is illustrated for a particle distance of 800 nm (bottom left) and 3000 nm (bottom right). Though the antiparallel state is predominant in both cases, there are parallel magnetization contributions in the case of the smaller distance (indicated e.g. by the more pronounced yellow and violet regions in the left image). The circles indicate the positions of the central particle (solid line) and its neighbors (dashed line) with respect to the sensor area.

### 6.3 Zinc nanowires

In this section, a scenario is treated that simulates the situation for Zn NW. The underlying mean unit cell area is again determined by means of SEM and counting over a representative area of about  $1200\ \mu\text{m}^2$  to approximately  $1000\ \text{nm} \times 1000\ \text{nm}$ . Here, the 350 nm CoFe-tagging is likewise replaced by CoFe particles with the respective volume-equivalent diameter. Fig. 76 shows the impact of the particles stray fields onto a sensor with a GMR amplitude of 8 % constrained to the unit cell dimensions for distances ranging from 4000 nm to 100 nm. The wider range of distances is chosen since, in principle, the approach of the introduced Zn NWs is not restricted by mutual interactions. However, this scenario is hypothetical and only

reasonable under consideration of long wires aligned distinctly oblique with respect to the substrate. The strong decrease of more than 4 % is thus solely attributed to the closer approach (until 100 nm) compared to the simulations modeling the PPy system. The results underline the importance of the vicinity of sensor and magnetic component for the sensing effect. However, SEM imaging of Zn NW oscillations (see Fig. 61) suggest that the maximum amplitude is of the order of 100 nm for a base-tag distance of several micrometers, which explains that no magnetically induced sensor signals could be measured for this system. The sensor saturation between 3900 nm and 4000 nm, for instance, amounts to only about one tenth of the overall saturation in the case of PPy.



**Figure 76: Simulated GMR response of dipolar CoFe particle as a function of distance from its center to the sensor surface from 4000 nm to 200 nm. The underlying sensor element (unit cell) is 1000 nm x 1000 nm in size.**

## 6.4 E-beam resist nanorods

Based on the model assumptions of section 6.1, also the expected sensor response to the configuration of tagged resist nanorods is simulated. In order to exclude boundary effects, again nine particles are implemented in a cubic lattice and the impact on a GMR sensor with an amplitude of ~12 % (see Fig. 70) is investigated within a unit cell for tag distances ranging between 2  $\mu\text{m}$  and 2.5  $\mu\text{m}$ . This distance range resembles the actual situation for the tagging by “Bioclone” particles (2  $\mu\text{m}$  bead radius) since 0.5  $\mu\text{m}$  is approximately the distance between the rod tip and the sensor surface (see Fig. 43b). A magnetization of 10 kA/m is estimated from the corresponding magnetization curve of the “Bioclone” beads at external field strength of 100 Oe. Due to a fairly large size distribution of the beads (see Fig. 69c), the particle diameter is adjusted to 4  $\mu\text{m}$  in the simulation, which is regarded to be more reasonable compared to the nominal diameter of 5  $\mu\text{m}$ . Fig. 77a shows the bead coverage as obtained by means of SEM imaging. From the corresponding binary<sup>23</sup> picture (b), a bead surface coverage of approximately 38 % is extracted by automated pixel counting.

<sup>23</sup> For details of the method used to extract the bead coverage from a grayscale SEM image, see section 5.4.2 of [138]).



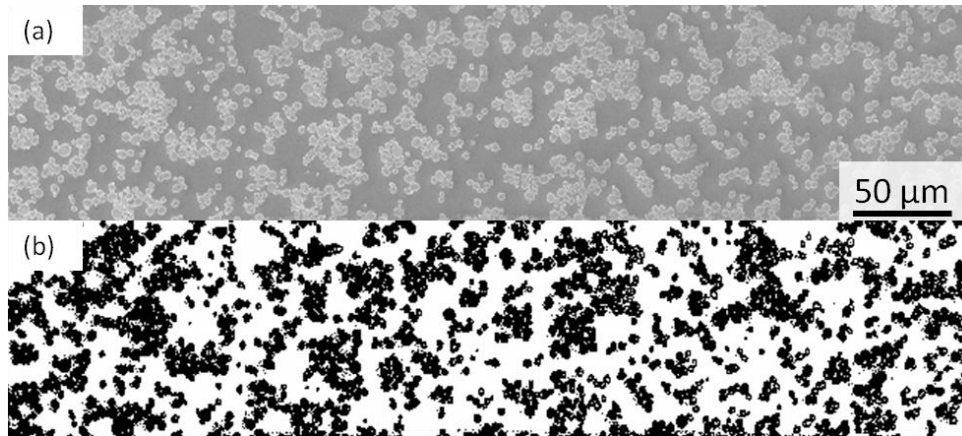


**Figure 77:** Distributed "Bioclone" beads at concentration of 1600  $\mu\text{g/ml}$  as imaged by SEM (a). The corresponding binary two color picture reveals a bead surface coverage of approximately 38 % (b).

Fig. 78 shows the results for a quadratic sensor area ( $31,36 \mu\text{m}^2$ ) with an edge length of 5.6  $\mu\text{m}$ . This area reflects the unit cell area corresponding to a coverage of  $\sim 40\%$ . The obtained GMR decrease is fairly small, namely 0.00043 % for the given distance range, which is more than two orders of magnitude smaller than the signals obtained in section 6.3 ( $\sim 0.106\%$  for eff. diameter of 370 nm). This explains why no signals have been obtained in this geometry. A reason therefore could be the small distance changes that arise from comparable large bead diameters. Moreover, a magnetic field with a magnitude of 100 Oe could be too small as to magnetize the beads sufficiently and the non-specific binding of the beads could be the cause.

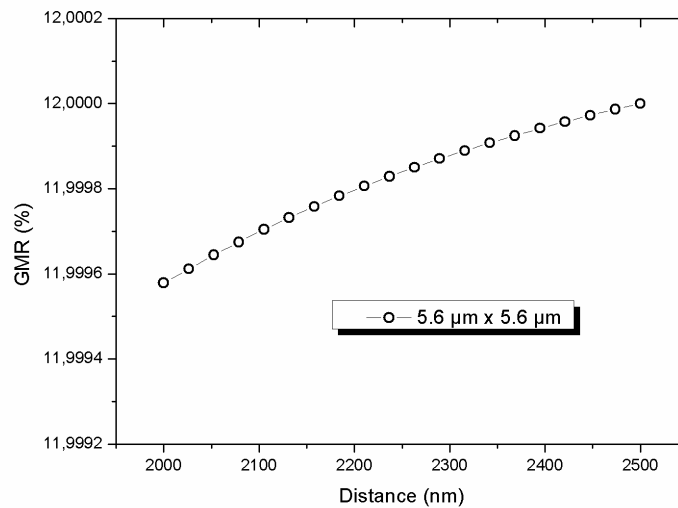


**Figure 78:** Simulated GMR response of superparamagnetic particles (diameter: 4  $\mu\text{m}$ ) as a function of distance from the centers to the sensor surface according to the OOMMF model from section 6.1. A unit cell area of  $31,36 \mu\text{m}^2$  is assumed.

## 7 Conclusion

Since only the results obtained for the PPy structures indicate a proof of the aimed mechanosensing, which is presented throughout this work, the following conclusion and discussion is dedicated to chapter 5.3. Originating from a simple geometric model consideration, a maximum possible threshold tagging can be estimated at which the NWs can no longer be regarded as mutual independent. To that end, we assume that the nominal deposition thickness is always reached at the top of the NWs, while the material deposited within the inter-wire space forms a uniform conformal coating of thickness  $d^*$  both around the nanowire sidewalls and the open substrate surface (see figure 79a). By equalizing the volume of deposited material according to this model with the nominal volume deposited on a flat surface, this “conformal mapping” model leads to a certain value of the coating  $d^*$  for each nominal coating thickness (see table 4). When the coating gets thicker than half of the interwire spacing, i.e.  $d^* > 89$  nm at a medium nanowire period of 300 nm, the tagging leads to clustering of the whole array to a continuous solid (see figure 79a). As shown by table 4, this limit is not reached even for the thickest nominal coating. However, the actual sputter coating is inhomogeneously distributed and more mushroom-shaped, thus causing the wires to come into mutual contact at a lower nominal coating thickness than estimated by the “conformal mapping” model. Looking at the measured mean NW diameters as they appear from a top view (see line 4 in table 4), nanowire conglomeration occurs at a nominal coating thickness of around 600 nm, which explains the reduced splitting of the measurement curves in comparison to the 300 nm thick coating as described in section 5.

**Table 4: The nominal thickness, modeled coating thickness, effective diameter as well as measured diameter are listed for the indicated tagging.**

Nom. thickness	As-deposited	50 nm CoFe	100 nm CoFe	300 nm CoFe	600 nm CoFe
Modeled coating thickness $d^*$ (nm)	-	7.8	14.4	33.7	51.0
Eff. Diameter $\Phi^*$ (nm)	-	100	260	370	550
Measured $\Phi$ (nm)	122	-	133	203	309

Although the simulation results allow a qualitative description of the magnetic sensing principle and help to assess important parameters, there are limitations in the applicability to the experiments that concern the modeling of the tag. At first, the precondition of ideal dipoles for deposited CoFe is hardly fulfilled since magnetic domains will form that diminish stray field formation due to the reduced shape anisotropy. In this context it should also be mentioned that the closer the wires come and the more CoFe material is deposited, the more likely the magnetic coupling will turn from “rod-like” to “film”-coupling [139]. This behavior will further reduce the stray field that arises from every single NW. The increased damping of the NW with increased tagging due to a larger stiffness is also disregarded in the model. Though the tag covers the NW surfaces at the top, it is seen that cavities remain between the NW roots due to shadowing effects and thus the NWs maintain flexibility (see Fig. 79c). Stiffness and “film-coupling” counteract with the magnetic moment and the additional mass which the tagging provides in order to achieve high signal amplitudes. The presented results suggest that a compromise of these aspects is met for tag thicknesses around 300 nm.

In the following an estimation of the NW bending due to inertial forces is carried out. Fig. 79b shows the result of a 2D finite element simulation of the NW bending implemented as a buckling problem with a parametric solution. Reasonable NW dimensions (diameter: 100 nm, vertical length projection: 1  $\mu\text{m}$ , radius of curvature: 1.75  $\mu\text{m}$ ) and material parameters ( $E \sim 1$  GPa) are assumed. The color

distribution reflects the *von Mises* stress. A force of  $F = 1$  nN exerted to the NW from the top thus causes a deflection of about 15 nm, toward the sensor (black line), as indicated in the figure. This associated information of force and bending is used to assess the quantity of deposit inducing the bending:

$$F = \rho_{CoFe} \cdot \frac{4}{3} \cdot \pi \cdot r^3 \cdot a_{max} \rightarrow r \approx 700 \text{ nm} \quad (7.2)$$

In this calculation the tagging of one single NW is again assumed to be spherical with radius  $r$ ,  $a_{max}=71300$  kgm/s<sup>2</sup> being the maximal acceleration the NW experiences during agitation at 190 kHz. The piezo extension at this frequency amounts to 50 nm, measured by means of SEM (see section 5.1.1). The obtained value of 700 nm suggests that the NW deflections are probably even smaller than 15 nm.

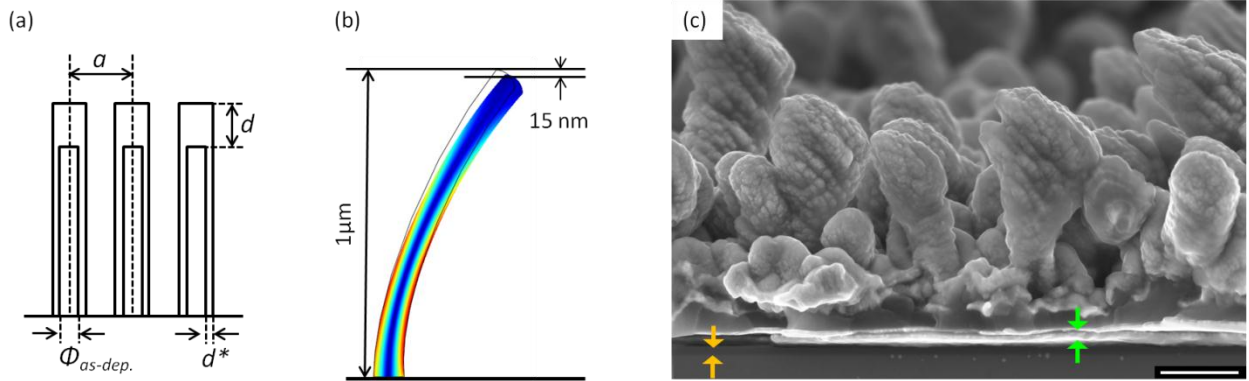


**Figure 79:** Schematic cross-section of the tagged NW array with indicated unit cell length  $a$ , thickness  $d$  and  $d^*$  and diameter  $\Phi_{as-dep}$ . (a). FEM calculation of a PPy NW bending under static force of 1 nN applied to the tip from above. The NW displacement is indicated. The color distribution reflects the *von Mises* stress in the NW (b). Cross-sectional SEM image of the cilia array coated with a 300 nm CoFe tagging (c). Orange and green arrows indicate the sensor multilayer and overoxidized PPy layer. The thicknesses amount to about 60 nm and 70 nm, respectively. The scale bar corresponds to 500 nm.

By means of the simulation such small displacements can be transferred into a GMR change. A GMR change of e.g. 0.002 % extracted from the course of Fig. 64, together with the underlying sensor resistance and the passed current would lead to a voltage of

$$V_{AC} = \frac{0.002}{100 \cdot \sqrt{2}} 10 \Omega \cdot 80 \text{ mA} = 11 \mu V . \quad (7.3)$$

Though this value defers from the measurements, the signals of which amount to around 0.5  $\mu V$ , one has to reflect that not the whole cilia array will perform a coherent, driven oscillation but due to slightly different geometries the phase correlation between the wires will disperse and thus lead to further signal reduction. In the current implementation of the introduced concept and referred to the scenario of PPy NWs used as artificial cilia, there is an inherent trade-off from the magnetic moment and mass on one side and the NW stiffness and parasitic, magnetic coupling on the other side, which limits the obtained signal amplitudes. Generally, the concept necessitates the close vicinity between sensor and magnetic component. Considering artificial cilia “transducers” in the nanoscale in conjunction with the respective tagging amounts and thus stray fields, this distance has to be realised to few hundreds of nanometers. These facts together with the limitations given by the NW self-assembly and associated synthesis temperatures complicate the achievement of an increased sensor performance in terms of voltage

amplitudes. Nevertheless, it has been shown that the detection of NW movements down to few nanometers is possible. For comparison, natural cilia of mechanoreceptors of cricket can detect displacements of less than one nanometer [8].

## 7.1 Outlook

A way to extend the temperature range in favor of the growth of e.g. Ge NW - which could then be grown in a higher density - would be the usage of tunnel-magneto-resistance (TMR) sensors that possess larger amplitudes than the GMR counterparts and which are known to endure temperatures of up to 450 °C without a significant loss of performance. In order to shift their resonance frequencies towards the experimentally accessible range, the NWs could be grown longer by increasing the growth time. Fig. 80 shows the morphology of Ge NWs grown at 340 °C on top of a TMR stack by means of SEM. The underlying stack is composed as follows:

Si(100) 50nm thermal oxide / Ta 5 nm / Ru 40 nm / Ta 5 nm / CoFeB 2.5 nm / MgO 1.65 nm / CoFeB 2.5 nm / Ru 1 nm / CoFe 5 nm / IrMn 15 nm / Ru 10 nm / Au 2 nm

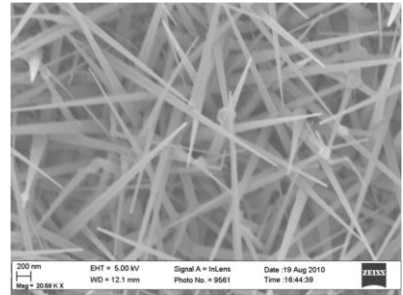


**Figure 80: Ge NWs grown on a structured TMR stack at temperatures of 340 °C and 75 mbar.**

and lithographically structured into 100 μm x 100 μm pillars (as well as 50 μm x 50 μm and 20 μm x 20 μm ellipses) with the aid of ion-etching by a “Roth & Rau Ionsys 500” instrument. The processing however would be much more complex due to the necessity of driving the current perpendicular to the stack plane.

In conclusion, the principle of a mechanosensor based on the GMR effect and nanowires as artificial cilia has been initially proven. However, the field remains ambitious due to the complexity of integrating non-related materials (polypyrrole) and processing techniques (self-assembly) into the well investigated schemes.

## Appendices

### A. Silicon nanowires by wet-etching

Within the studies of the sensing concept presented in this work a chemical approach for the synthesis of Si NWs by wet-etching with hydrofluoric acid and silver nitrate (HF/AgNO<sub>3</sub>) has been investigated according to [140]. The self-assembled process directly applied to a silicon (100) wafer, is independent of crystal orientation and proceeds via a localized micro-electro-chemical “re-dox” reaction [141]. The wafers are therefore freed from the native oxide in a buffered HF solution<sup>24</sup> and left in a solution of 0.02 molar AgNO<sub>3</sub> and 4.6-molar HF at 50°C. The etching rate has been extracted to be ~0,3-0.4 μm/min. The wire length is adjustable by the etching time, while density control of the NWs by basic parameters is not possible. During the etching process, metallic atoms depositing on the Si surface form nuclei that behave as a cathode, whereas the area surrounding the nuclei behaves as an anode and will thus be etched away and dissolve. Fig. 81 shows a tilted view SEM image of a small fraction of the etched structures. The insets show images from the top (left) and substrate surface (right). NW diameters measure about 100 nm, whereas the top view suggests that sometimes “chain-like”, elongated structures form. Furthermore there is tendency of bunching of the tips which increases with the wire length. This bunching is attributed to electrostatic interactions [142]. After each synthesis the sample surface is covered with dendrites of Ag, the removal of which is performed in a (5:1)-solution of HNO<sub>3</sub> and H<sub>2</sub>O at 70 °C.

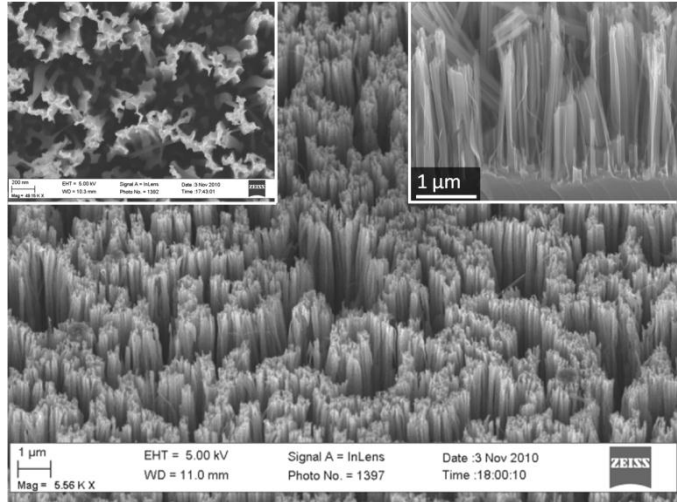


**Figure 81: Tilted (40°) view SEM image of Si NWs chemically wet-etched by HF/AgNO<sub>3</sub> in a top-down manner. Right inset depicts top and left one tilted view (40°) of the substrate edge.**

In general the etching approach was intended for the fabrication of NWs as artificial cilia. Since the structures cannot be assembled on top of GMR sensors, a “flip-chip” process was discussed in which the NW tips oppose the sensor. A frame of photo-resist served for the separation. Due to the vertical alignment, stiffness and bunching of the structures and the demands to place the NWs closely to the sensor without any contact, the idea was abolished.

### B. Nanowires of polycyanurate thermoset

In this section it is shortly deferred to the integration of top-down fabricated, polymeric nanorods on GMR samples. Therefore the cyanate ester [143] monomer is filled into the nanopores of track-etched alumina membranes [142] as substrates as shown schematically in Fig. 82a. The nanopores have diameters of 180 nm and lengths of 1 μm (see Fig. 82b, c). Any excess monomer is detached by cutting at low temperatures of about 200 K to obtain a plane surface. Next the sample is flipped and pressed against the Au surface of

<sup>24</sup> HF, H<sub>2</sub>O and NH<sub>4</sub>F mixed 1:5:5 by volume parts.

a readily prepared GMR sample<sup>25</sup>. The whole device is fixed with teflon tape and cured at temperatures of maximal 260 °C for 13 h to provoke polymerization to a polycyanurate thermoset (PCT) and cross-linking of a thiol-Au-bond. Afterwards the edge regions of the sample are painted with nail polish in order to protect the sensor layers against subsequent chemical detachment of the membrane. Therefore the aluminum base and the alumina membrane are dissolved selectively in  $\text{CuCl}_2 \cdot \text{H}_2\text{O} / \text{HCl}$  for 5 h and  $\text{H}_3\text{PO}_4$  (10 %) for 3 h, respectively.

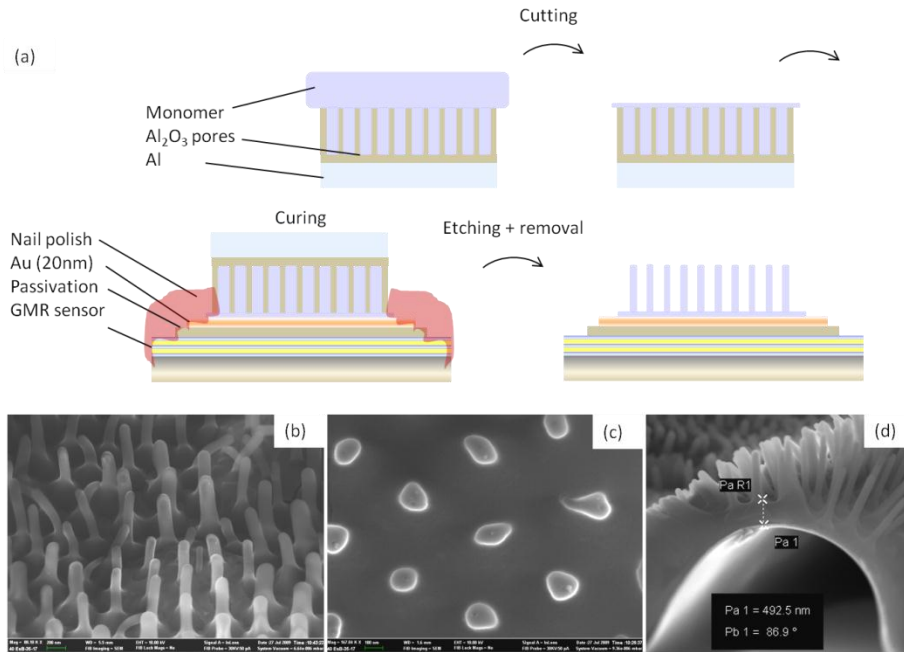


**Figure 82:** Schematic of PC nanorod preparation process (a). Tilted (b), top (c) and side view (d) SEM images of the nanorod array arising from the process. A PC base layer with a thickness of about 500 nm is shown underneath the rod network (d).

Although PCT possesses a Young's modulus of  $\sim 3$  GPa [143] and is thus potentially suitable as NW transducer material, there are major drawbacks which disqualify the approach for the aimed concept. This is e.g. the deficient connection between the sensor / Au and the thermoset (Fig. 82d) as well as the inherent pitch which comes from the cutting (Fig. 82a). Like indicated in Fig. 82d there is thus a separation of at least 500 nm between sensor and NW array. By means of section 6, however, the importance of close vicinity of the respective artificial cilia structure, is made clear and the approach is this way not applicable. Moreover the final etching procedures lead to the delamination of metallic layers at the sides, where the sensor is not covered by the PCT structures.

<sup>25</sup> After the sensor layer deposition, the sample is coated subsequently with 20 nm MgO, 2 nm Ta and 20 nm Au.

## C. EDX results of section 5.3

### Summary results (1.5 kV)

Element	Weight %	Weight % $\sigma$	Atomic %
Carbon	1.872	0.203	7.295
Oxygen	5.935	0.530	17.361
Iron	48.661	2.999	40.776
Cobalt	43.532	2.898	34.568

### Summary results (2.5 kV)

Element	Weight %	Weight % $\sigma$	Atomic %
Carbon	1.340	0.128	5.570
Oxygen	3.807	0.250	11.882
Iron	46.395	1.510	41.486
Cobalt	48.459	1.461	41.062

### Summary results (5 kV)

Element	Weight %	Weight % $\sigma$	Atomic %
Carbon	1.318	0.100	5.615
Oxygen	2.567	0.131	8.206
Silicon	0.576	0.116	1.049
Iron	46.044	0.832	42.171
Cobalt	49.495	0.813	42.959

### Summary results (10 kV)

Element	Weight %	Weight % $\sigma$	Atomic %
Carbon	1.389	0.105	5.880
Oxygen	2.805	0.094	8.914
Silicon	0.412	0.050	0.747
Iron	45.510	0.555	41.428
Cobalt	49.883	0.552	43.032

### Summary results (15 kV)

Element	Weight %	Weight % $\sigma$	Atomic %
Carbon	1.975	0.132	8.080
Oxygen	3.458	0.084	10.620
Silicon	0.636	0.037	1.112
Chlorine	0.224	0.035	0.311
Iron	45.454	0.218	39.991
Cobalt	47.664	0.225	39.740
Gold	0.589	0.141	0.147

### Summary results (20 kV)

Element	Weight %	Weight % $\sigma$	Atomic %
Carbon	3.094	0.472	11.729
Oxygen	4.401	0.255	12.526
Silicon	2.714	0.119	4.401
Chlorine	0.311	0.076	0.400
Iron	43.419	0.413	35.405
Cobalt	45.094	0.427	34.846
Copper	0.968	0.199	0.694



## D. Conversion of Miller- to Bravais-indices

For hexagonal crystals, it is useful to utilize the *Bravais*- instead of *Miller* indexing system. *Bravais* indices comprise four components, namely “HKIL” (instead of the *Miller* indices “hkl” ), the first three of which describe three main axes of the six-fold symmetry of a hexagonal plane, whereas L describes the collinear, vertical axis. Directional indices are denoted with “uvw” and “UVTW” accordingly.

Plane indices:  $H=h$ ;  $K=k$ ;  $I=-(H+K)$ ;  $L=l$

Direction indices:  $U=1/3(2u-v)$ ;  $V=1/3(2v-u)$ ;  $T=-(U+V)$ ;  $W=w$

## E. Processing outline for GMR sensor structuring

1. Substrate cleaning:
  - Aceton and isopropanol + soft ultrasonication for 2 min each
  - 2 min drying at 120 °C
2. Resist:
  - HDMS (35 s / 4000 rpm)
  - LOR 3A (35 s / 3000 rpm) + 5 min bake at 150 °C
  - MIR 701 (35 s / 4000 rpm) + 1 min bake at 110 °C
3. UV Illumination and development:
  - Frame (18 mm): 60 s (“Suss MJB3”, 350-450nm, 350 W mercury lamp) + 30 s MIF development; rinsing in deionized water
  - Meander : develop AZ 726 and MIF 6 s and 30 s resp.; rinsing in deionized water
4. Sputter-dep. Ta-mask:
  - 45 nm Ta layer
5. Removal:
  - NMP / MR1165 at 80 °C for 30 min
  - NMP/ MR1165, aceton and isopropanol + soft ultrasonication for 5 min each
6. Ion beam etching (“Roth & Rau, Ionsys 500”):
  - Time: 11 min.
  - Tilt: 50 °
  - Beam voltage: 500 V
  - Accel. Voltage: 500 V
  - Power: 300 W
  - Beam current: 45 mA
  - Rotation: 3 rpm
  - Ar gas flow: 10 sccm
7. Resist (see above)
8. Illumination:

- Contact leads 7s + MIF development for 40-45 s; rinsing in deionized water
9. Sputter-dep:  $P_{Ar}=8e-3$  bar,  $P_{Base} = 2e-5$  bar, Power: 50 /100 W
    - Ti: 2 x 30 s (10 nm), 50 W
    - Au: 4 x 30 s Au (250 nm), 50 W
    - Ti: 30 s (5 nm), 50 W
  10. Removal:
    - NMP / MR1165 at 80°C for 30min
    - NMP/ MR1165, acetone and isopropanol + soft ultrasonication for 5 min each
  11.  $Si_3N_4$  passivation by plasma-enhanced chemical vapor deposition (PECVD)
    - $SiH_4/N_2$  flow: 700 sccm
    - $NH_3$  flow: 18 sccm
    - Power: 10 W
    - Temperature: 200 °C
    - Time: 20 min
    - Druck:  $1.33 \cdot 10^{-3}$  bar
  12. Resist:
    - Ti-Prime (HDMS) (35 s / 4000 rpm)
    - AZ 5214 (35s / 8000 rpm) + 1 min bake at 120 °C
  13. Image reversal:
    - Illumination contact leads: 3s
    - 1 min bake at 120 °C
    - Illumination: 10 s
    - MIF development for 30 s; rinsing in deionized water
  14. Buffered (ammoniumfluoride 875-125 Riedel-de Haén 40207) HF-etching:
    - Time: 25s + 1min rinsing in deionized water
  15. Removal (AZ 5214):
    - Acetone and isopropanol + soft ultrasonication

## Bibliography

- [1] E. Munch, M. E. Launey, D. H. Alsem, E. Saiz, A. P. Tomsia and R. O. Ritchie (2008) Tough, bio-Inspired hybrid materials *Science* 322, 1516
- [2] A. Dussutour, V. Fourcassie, D. Helbing and J. L. Deneubourg (2004) Optimal traffic organization in ants under crowded conditions *Nature* 428, 70
- [3] Y. Bar-Cohen (2004) *Electroactive Polymer (EAP) Actuators as Artificial Muscles – Reality, Potential and Challenges*, 2<sup>nd</sup> Edition, SPIE press, Bellingham WA
- [4] “Whale power” from *Technology Review* 03/2011 (Deutsche Ausgabe)
- [5] (a) T. F. Otero (2008) Reactive conducting polymers as actuating sensors and tactile muscles *Bioinspir. Biomim.* 3 035004; (b) K. Kaneto, H. Suematsu and K. Yamato (2008) Training effect and fatigue in polypyrrole-based artificial muscles *Bioinspir. Biomim.* 3 035005
- [6] (a) S. M. van Netten (2006) Hydrodynamic detection by cupulae in a lateral line canal: functional relations between physics and physiology *Biol. Cybern.* 94: 67; (b) Y. Yang, N. Nguyen, N. Chen, M. Lockwood, C. Tucker, H. Hu, H. Bleckmann, C. Liu and D. L Jones (2010) Artificial lateral line with biomimetic neuromasts to emulate fish sensing *Bioinspir. Biomim.* 5 016001
- [7] T. Shimozawa, T. Kumagai and Y. Baba (1998) Structural scaling and functional design of the cercal wind-receptor hairs of cricket *J. Comp. Physiol. A* 183 171
- [8] F. G. Barth, J. A. G. Humphrey and T. W. Secomb (2003) *Sensors and sensing in biology and engineering* Springer Vienna New York, chapter 9
- [9] F. G. Barth, J. A. G. Humphrey and T. W. Secomb (2003) *Sensors and sensing in biology and engineering* Springer Vienna New York, chapter 10
- [10] F. Delcomyn (1996) *Foundations of Neurobiology* Freeman New York
- [11] (a) J. P. Strachan, V. Chembrolu, Y. Acremann, X. W. Yu, A. A. Tulapurkar, T. Tyliczszak, J. A. Katine, M. J. Carey, M. R. Scheinfein, H. C. Siegmann and J. Stohr (2008) Direct observation of spin-torque driven magnetization reversal through nonuniform modes *Phys. Rev. Lett.* 100 247201 1; (b) M. Wenin, A. Windisch and W. Pötz (2010) Optimal control of magnetization dynamics in ferromagnetic heterostructures by spin-polarized currents *J. Appl. Phys.* 108 103717 1
- [12] (a) J. Bernstein, R. Miller, W. Kelley and P. Ward (1999) Low-noise MEMS vibration sensor for geophysical applications *J. Microelectromech. Systems* 8 4; (b) L. P. Wang, R. A. Wolf, Y. Wang, K. K. Deng, L. Zou, R. J. Davis and S. Trolier-McKinstry (2003) Design, fabrication, and measurement of high-sensitivity piezoelectric microelectromechanical systems accelerometers *J. Microelectromech. Systems* 12 4
- [13] N. Roxhed, P. Griss and G. Stemme (2007) A method for tapered deep reactive ion etching using a modified Bosch process *J. Micromech. Microeng.* 17 1087
- [14] [http://www.meas-spec.com/product/t\\_product.aspx?id=2474](http://www.meas-spec.com/product/t_product.aspx?id=2474)
- [15] <http://www.bosch-sensortec.de/content/language1/html/4691.htm>

- [16] L. Svensson, J. A. Plaza, M. A. Benitez, J. Esteve and E. Lora-Tamayo (1996) Surface micromachining technology applied to the fabrication of a FET pressure sensor *J. Micromech. Microeng.* 6 80
- [17] Z. G. Zhou and Z. W. Liu (2008) Biomimetic cilia based on MEMS technology *J. Bionic Engin.* 5 358
- [18] K. Oh, J. H. Chung, S. Devasia and J. J. Riley (2009) Bio-mimetic silicone cilia for microfluidic manipulation *Lab Chip* 9 1561
- [19] C. Liu (2007) Micromachined biomimetic artificial haircell sensors *Bioinspir. Biomim.* 2 S162
- [20] Y. Yang, N. Nguyen, N. Chen, M. Lockwood, C. Tucker, H. Hu, H. Bleckmann, C. L. Douglas and L. Jones (2010) Artificial lateral line with biomimetic neuromasts to emulate fish sensing *Bioinspir. Biomim.* 5 016001
- [21] G. J. M. Krijnen, M. Dijkstra, J. J. van Baar, S. S. Shankar, W. J. Kuipers, R. J. H. de Boer, D. Altpeter, T. S. J. Lammerink and R. Wiegerink (2006) MEMS based hair flow-sensors as model systems for acoustic perception studies *Nanotechnology* 17 S84
- [22] J. V. I. Timonen, C. Johans, K. Kontturi, A. Walther, O. Ikkala and R. H. A. Ras (2010) A facile template-free approach to magnetodiven, multifunctional artificial cilia *Appl. Mater. Int.* 2 8 2226
- [23] B. A. Evans, A. R. Shields, R. L. Carroll, S. Washburn, M. R. Falvo and R. Superfine (2007) Magnetically actuated nanorod arrays as biomimetic cilia *Nano Lett.* 7 5 1428
- [24] P. D. McGary, L. Tan, J. Zou, B. J. H. Stadler, P. R. Downey and A. B. Flatau (2006) Magnetic nanowires for acoustic sensors *J. Appl. Phys.* 99 08B310
- [25] (a) F. Fahrni, M. W. J. Prins and L. J. van IJzendoorn (2008) Magnetization and actuation of polymeric microstructures with magnetic nanoparticles for application in microfluidics *J. Magn. Magn. Mater.* 321 1843; (b) F. Fahrni, M. W. J. Prins and L. J. van Ijzendoorn (2009) Micro-fluidic actuation using magnetic artificial cilia *Lab on Chip* 9 3413
- [26] S. Ghosh, A. K. Sood and N. Kumar (2003) Carbon nanotube flow sensors *Science* 299 1042
- [27] W. Schmickler (1996) *Grundlagen der Elektrochemie* Vieweg
- [28] S. Cosnier and A. Karyakin, (2010) *Electropolymerization (Concepts, Materials and Applications)* Wiley-Vch
- [29] <http://www.piceramic.de/piezoeffekt.php>
- [30] G. Binasch, P. Grünberg, F. Saurenbach and W. Zinn (1989) Enhanced magnetoresistance in layered magnetic structures with antiferromagnetic interlayer exchange *Phys. Rev. B* 39 4828
- [31] M. N. Baibich, J. M. Broto, A. Fert, F. Nguyen-Van-Dau, F. Petroff, P. Etienne, G. Creuzet, A. Friedrich and J. Chazelas (1988) Giant Magnetoresistance of (001) Fe / (001) Cr Magnetic Snperlattices *Phys. Rev. Lett.* 61 2472
- [32] U. Hartmann (2000) *Magnetic Multilayers and Giant Magnetoresistance* (2000) Springer
- [33] P. Grünberg, R. Schreiber, Y. Pang, M. B. Brodsky and H. Sowers (1986) Layered Magnetic Structures: Evidence for Antiferromagnetic Coupling of Fe Layers across Cr Interlayers *Phys. Rev. Lett.* 57 2442

- [34] (a) R. F. C. Farrow, C. H. Lee and S. S. P. Parkin (1990) Magnetic multilayer structures *IBM J. Res. And Develop.* 34 903; (b) Y. Y. Huang, G. P. Felcher and S. S. P. Parkin (1991) Antiferromagnetic and ferromagnetic order in Co/Cu multilayers *J. Magn. Magn. Mater.* 99 L31; (c) S. S. P. Parkin, R. Bhadra and K. P. Roche (1991) Oscillatory Magnetic Exchange Coupling through Thin Copper Layers *Phys. Rev. Lett.* 66 2152
- [35] (a) J. Barnas, A. Fuss, R. E. Camley, U. Walz, P. Grünberg and W. Zinn. (1990) *Vacuum* 41 1241; (b) J. Barnas, A. Fuss, R. E. Camley, P. Grünberg and W. Zinn. (1990) Novel magnetoresistance effect in layered magnetic structures: Theory and experiment *Phys. Rev. B* 42 8110
- [36] (a) M. A. Rudermann and C. Kittel (1956) Indirect Exchange Coupling of Nuclear Magnetic Moments by Conduction Electrons *Phys. Rev.* 96 99; (b) T. Kasuya (1954) A theory of metallic ferromagnetism and antiferromagnetism on zeners model *Progr. Theor. Phys.* 16 45; (c) K. Yosida (1957) Magnetic Properties of Cu-Mn Alloys. *Phys. Rev.Lett.* 106 893
- [37] (a) L. M. Roth, H. J. Zeiger and T. A. Kaplan (1966) Generalization of the Ruderman-Kittel-Kasuya-Yosida Interaction for Nonspherical Fermi Surfaces *Phys. Rev.* 149 519; (b) M. T. Johnson, R. Coehoorn, J. J. de Vries, N. W. E. McGee, J. aan de Stegge and P. J. H. Bloemen (1992) Orientational Dependence of the Oscillatory Exchange Interaction in Co/Cu/Co *Phys. Rev. Lett.* 69 969; (c) M. T. Johnson, S. T. Purcell, N. W. E. McGee, R. Coehoorn, J. aan de Stegge and W. Hoving (1992) Structural Dependence of the Oscillatory Exchange Interaction across Cu Layers *Phys. Rev. Lett.* 68 2688
- [38] P. Bruno and C. Chappert (1991) Oscillatory coupling between ferromagnetic films separated by a non-magnetic metal spacer *Phys. Rev. Lett.* 67 1602
- [39] P. Bruno and C. Chappert (1992) Ruderman-Kittel theory of oscillatory interlayer exchange coupling *Phys. Rev. B* 46 261
- [40] (a) J. Mathon, M. Villeret, R. B. Muniz, J. d'Albuquerque e Castro and D. M. Edwards (1995) Quantum Well Theory of the Exchange Coupling in Co/Cu/Co(001) *Phys. Rev. Lett.* 74 3696; (b) J. Mathon, M. Villeret, A. Umerski, R. B. Muniz, J. d'Albuquerque e Castro and D. M. Edwards (1997) Quantum-well theory of the exchange coupling in magnetic multilayers with application to Co/Cu/Co.001 *Phys. Rev. B* 56 11797
- [41] R. Gross (2004) Manuscript zur Vorlesung „Spinelektronik“ Walter-Meissner Institut, Walter-Meissner-Straße 8, D-85748 Garching
- [42] P. Bruno (1995) Theory of interlayer magnetic coupling. *Phys. Rev. B* 411-439
- [43] P. Bruno (1993) Oscillations of Interlayer Exchange Coupling vs. Ferromagnetic-Layers Thickness *Euro. Phys. Lett.* 23 615
- [44] J. Barnas (1992) Coupling between two ferromagnetic films through a nonmagnetic metallic layer *J. Magn. Magn. Mater.* 111 L215
- [45] (a) M. D. Stiles (1996) Spin-dependent interface transmission and reflection in magnetic multilayers *J. Appl. Phys.* 79 5805; (b) M. D. Stiles (1999) Interlayer exchange coupling *J. of Magn. and Magn. Mater.* 200 322

- [46] (a) J. C. Slonczewski (1993) Origin of biquadratic exchange in magnetic multilayers *J. appl. Phys.* 73 5957; (b) M. Schäfer, S. Demokritov, S. Müller-Pfeiffer, R. Schäfer, M. Schneider, P. Grünberg and W. Zinn. (1995) Investigation of 90° coupling in Fe/Ag/Fe structures: ‘‘Loose spins’’ and fluctuation mechanism *J. Appl. Phys.* 77 6432
- [47] N. Mott (1936) The Resistance and Thermoelectric Properties of the Transition Metals *Proc. Roy. Soc.* 156 368
- [48] (a) B. Dieny (1992) Quantitative Interpretation of Giant Magnetoresistance Properties of Permalloy-Based Spin-Valve Structures *Euro. Phys. Lett.* 17 261; (b) B. Dieny, V. S. Speriousu, J. P. Nozieres, B. A. Gurney, A. Vedyayev and N. Ryzhanova (1993) *Magnetism in Structure in Systems of reduced dimensions*, eds. R. F. C. Rarrow et al. Plenum New York
- [49] N. Mott (1936) The Electrical Conductivity of Transition Metals *Proc. Roy. Soc. A* 153 699
- [50] H. Kronmüller and S. Parkin *Handbook of Magnetism and Advanced Magnetic Materials*, Wiley
- [51] K. Fuchs (1938) The conductivity of thin metallic films according to the electron theory of metals *Mathematical Proceedings of the Cambridge Philosophical Society* 34 100; E. H. Sondheimer (1952) The mean free path of electrons in metals *Advan. Phys.* 1 1
- [52] (a) P. M. Levy, S. Zhang and A. Fert (1990) Electrical Conductivity of Magnetic Multilayered Structures *Phys. Rev. Lett.* 65 1643; (b) A. Vedyayef, B. Dieny and N. Ryshanova (1992) Quantum Theory of Giant Magnetoresistance of Spin-Valve Sandwiches *Euro. Phys. Lett.* 19 329
- [53] R. Kubo (1957) Statistical-Mechanical Theory of Irreversible Processes I. Generell Theory and Simple Applications to Magnetic and Conduction Problems *Journal of the Physical Society of Japan* 12 570
- [54] A. Barthelemy and A. Fert (1991) Theory of the magnetoresistance in magnetic multilayers: Analytical expressions from a semiclassical approach *Phys. Ref. B* 43 13124
- [55] P. Zahn, I. Mertig, M. Richter and H. Eschrig (1995) Ab Initio Calculations of the Giant Magnetoresistance *Phys. Rev. Lett.* 75 2996
- [56] G. J. Long and F. Grandjean (1991) *Supermagnets: Hard magnetic materials* Kluwer
- [57] R. Schad, C. D. Potter, P. Belien, G. Verbanck, V. V. Moschalkov and Y. Bruynseraede (1994) Giant magnetoresistance in Fe/Cr superlattices with very thin Fe layers *Appl. Phys. Lett.* 64 3500
- [58] S. S. P. Parkin, Z. G. Li and S. J. Smith (1991) Giant magnetoresistance in antiferromagnetic Co/Cu multilayers *Appl. Phys. Lett.* 58 2710
- [59] C. Buzau Ene, G. Schmitz, R. Kirchheim and A. Hütten (2005) Stability and thermal reaction of GMR NiFe/Cu thin films *Acta Materialia* 53 3383
- [60] M. Hecker, D. Tietjen, H. Wendrock, C.M. Schneider, N. Cramer, L. Malkinski, R.E. Camley and Z. Celinski (2002) Annealing effects and degradation mechanism of NiFe/Cu GMR multilayers *J Magn Mater.* 247 62

- [61] R. M. Bozorth (1978) *Ferromagnetism* IEEE Press, The Institute of Electrical and Electronics Engineers New York
- [62] (a) M. S. Islam, S. Sharma, T. L. Kamins and R. S. Williams (2004) Ultrahigh-density silicon nanobridges formed between two vertical silicon surfaces *Nanotechnology* 15 L5; (b) T. L. Kamins, S. Sharma, A. A. Yasseri, Z. Li and J. Straznicky (2006) Metal-catalysed, bridging nanowires as vapor sensors and concept for their use in a sensor system *Nanotechnology* 17 S291
- [63] (a) R. S. Wagner and W. C. Ellis (1964) Vapor-liquid-solid mechanism of single crystal growth *Appl. Phys. Lett.* 4 89 ; (b) B. J. Ohlsson, H. M. Magnusson, M. T. Björk, L. R. Wallenberg, K. Deppert and L. Samuelson (2001) Size-, shape-, and position-controlled GaAs nano-whiskers *Appl. Phys. Lett.* 79 3335; (c) M. T. Björk, B. J. Ohlsson, T. Sass, A. I. Persson, C. Thelander, M. H. Magnusson, K. Deppert, L. R. Wallenberg and L. Samuelson (2002) One-dimensional Steeplechase for Electrons Realized *Nano Lett.* 2 87 ; (d) C. M. Lieber (1998) One-Dimensional Nanostructures: Chemistry, Physics and Applications *Solid State Comm.* 107 607; (e) Y. Cui and C. M. Lieber (2001) Functional Nanoscale Electronic Devices Assembled Using Silicon Nanowire Building Blocks *Science* 291 851
- [64] (a) Z. L. Wang (2004) Zinc oxide nanostructures: growth, properties and applications *J. Phys.: Cond. Mat.* 16 R829; (b) R. Yang, Y. Chueh, J. R. Morber, R. Snyder, L. Chou and Z. L. Wang (2007) Single-Crystalline Branched Zinc Phosphide Nanostructures: Synthesis, Properties, and Optoelectronic Devices *Nano Lett.* 7 269; (c) J. S. Lee, M. S. Islam and S. Kim (2006) Direct Formation of Catalyst-Free ZnO Nanobridge Devices on an Etched Si Substrate Using a Thermal Evaporation Method *Nano Lett.* 6 1487
- [15] (a) J. K. Gimzewski and R. Moller (1987) Transition from the tunneling regime to point contact studied using scanning tunneling microscopy *Phys. Rev. B* 36 1284; (b) J. I. Pascual, J. Mendez, J. Gomez-Herrero, A. M. Baro, N. Garcia and V. T. Binh (1993) Quantum Contact in Gold Nanostructures by Scanning Tunneling Microscopy *Phys. Rev. Lett.* 71 1852; (c) J. I. Pascual, J. Mendez, J. Gomez-Herrero, A. M. Baro, N. Garcia, U. Landmann, W. D. Luedtke, E. N. Bogachek and H. P. Cheng (1995) Properties of Metallic Nanowires: From Conductance Quantization to Localization *Science* 267 1793
- [66] (a) C. J. Muller, J. M. van Ruitenbeek and L. J. de Jongh (1992) Conductance and Supercurrent Discontinuities in Atomic-Scale Metallic Constrictions of Variable Width *Phys. Rev. Lett.* 69 140; (b) J. M. Krans, J. M. van Ruitenbeek, V. V. Fisun, I. K. Yasun and L. J. de Jongh (1995) The signature of conductance quantization in metallic point contacts *Nature* 375 767; (c) U. Landmann, W. D. Luedtke, B. E. Salisbury and R. L. Whetten (1996) Reversible Manipulations of Room Temperature Mechanical and Quantum Transport Properties in Nanowire Junctions *Phys. Rev. Lett.* 77 1362; (d) J. L. Costa-Kramer, N. Garcia, P. Garcia-Mochales and P. A. Serena (1995) Nanowire formation in macroscopic metallic contacts: quantum mechanical conductance tapping a table top *Surf. Sci.* 342 L1144; (e) H. Yasuda and A. Sakai (1997) Conductance of atomic-scale gold contacts under high-bias voltages *Phys. Rev. B* 56 1069
- [67] (a) C. Z. Li and N. J. Tao (1998) Quantum transport in metallic nanowires fabricated by electrochemical deposition/dissolution *Appl. Phys. Lett.* 72 894; (b) C. Z. Li, A. Bogozzi, W. Huang and N. J. Tao (1999) Fabrication of stable metallic nanowires with quantized conductance *Nanotechnology* 10 221
- [68] (a) J. G. Wang, M. Tian, N. Kumar and T. E. Mallouk (2005) Controllable Template Synthesis of

- Superconducting Zn Nanowires with Different Microstructures by Electrochemical Deposition *Nano Lett.* 5 1247; (b) M. Tian, N. Kumar, S. Xu, J. Wang, J. S. Kurtz and M. H.W. Chan (2005) Suppression of Superconductivity in Zinc Nanowires by Bulk Superconductors *Phys. Rev. Lett.* 95 76802
- [69] (a) F. Elhoussine, S. Matefi-Tempfli, A. Encinas and L. Piraux (2002) Conductance quantization in magnetic nanowires electrodeposited in nanopores *Appl. Phys. Lett.* 81 1681; (b) M. Tian, J. Wang, J. Kurtz, T. E. Mallouk and M. H. W. Chan (2003) Electrochemical Growth of Single-Crystal Metal Nanowires via a Two-Dimensional Nucleation and Growth Mechanism *Nano Lett.* 3 919
- [70] L. Li, Y. Yang, X. Huang, G. Li and L. Zhang (2006) Pulsed electrodeposition of single-crystalline Bi<sub>2</sub>Te<sub>3</sub> nanowire arrays *Nanotechnology* 17 1706
- [71] F. J. Himpsel, T. Jung and J. E. Ortega (1997) Nanowires on Stepped Metal Surfaces *Surf. Rev. Lett.* 4 371
- [72] B. Gates, Y. Yin and Y. J. Xia (2000) A Solution-Phase Approach to the Synthesis of Uniform Nanowires of Crystalline Selenium with Lateral Dimensions in the Range of 10-30 nm *Am. Chem. Soc.* 122 12582
- [73] J. P. Heremans, C. M. Thrush, D. T. Morelli and M. C. Wu (2003) Resistance, Magnetoresistance, and Thermopower of Zinc Nanowire Composites *Phys. Rev. Lett.* 91 076804
- [74] S.R.C. Vivekchand, G. Gundiah, A. Govingaraj and C.N.R. Rao (2004) A New Method for the Preparation of Metal Nanowires by the Nebulized Spray Pyrolysis of Precursors *Adv. Mater.* 16 1842
- [75] S. Kar, T. Ghoshal and S. Chaudhuri (2006) Simple thermal evaporation route to synthesize Zn and Cd metal nanowires *Chem. Phys. Lett.* 419 174
- [76] Y. Yan, P. Liu, M. J. Romero and M. M. Al-Jassim (2003) Formation of metallic zinc nanowires *J. Appl. Phys.* 93 4807
- [77] J. Li, X. Chen (2004) Large-scale and catalyst-free synthesis of zinc nanotubes and nanowires *Solid State Comm.* 131 769
- [78] X. S. Peng, L. D. Zhang, G. W. Meng, X. Y. Yuan, Y. Lin and Y. T. Tian (2003) Synthesis of Zn nanofibres through simple thermal vapour-phase deposition *J. Phys. D: Appl. Phys.* 36 L35
- [79] J. Liu, Z. Zhang, X. Su and Y. Zhao (2005) From zinc nanowires to zinc oxide nanowires: a low substrate-temperature approach *J. Phys. D: Appl. Phys.* 38 1068
- [80] X. Wen, Y. Fang and S. Yang (2005) Ultrathin Zinc Nanowires and Nanotubes Grown by Vapor Transport *An. Chem. Int. Ed.* 44 3562
- [81] W. Seifert, M. Borgström, K. Deppert, K. A. Dick, J. Johansson, M. W. Larsson, T. Mårtensson, N. Sköld, C. P. T. Svensson, B. A. Wacaser, L. R. Wallenberg and L. Samuelson (2004) Growth of one-dimensional nanostructures in MOVPE *J. Cryst. Growth* 272 211
- [82] V. G. Dubrovskii, N. V. Sibirev, G. E. Cirlin, J. C. Harmand and V. M. Ustinov (2006) Theoretical analysis of the vapor-liquid-solid mechanism of nanowire growth during molecular beam epitaxy *Phys. Rev. E* 73 21603



- [83] K. Keem, D.Y. Jeong, S. Kim, M.S. Lee, I.S. Yeo, U.I. Chung and J.T. Moon (2006) Fabrication and Device Characterization of Omega-Shaped-Gate ZnO Nanowire Field-Effect Transistors *Nano Lett.* 6 1454
- [84] X. Feng, L. Feng, M. Jin, J. Zhai, L. Jiang and D. Zhu (2004) Reversible Super-hydrophobicity to Super-hydrophilicity Transition of Aligned ZnO Nanorod Films *Am. Chem. Soc.* 126 62
- [85] J.B. Baxter and E.S. Aydil (2005) Nanowire-based dye-sensitized solar cells *Appl. Phys. Lett.* 86 053114
- [86] (a) Z. Fan and J.G. Lu (2005) Gate-refreshable nanowire chemical sensors *Appl. Phys. Lett.* 86 123510; (b) Z. Fan, D. Wang, P.C. Chang, W.Y. Tseng and J.G. Lu (2004) *Appl. Phys. Lett.* 85 245923; (c) Q. Wan, Q.H. Li, Y.J. Chen, T.H. Wang, X.L. He, J.P. Li and C.L. Lin (2004) *Appl. Phys. Lett.* 84 183654
- [87] M.H. Huang, S. Mao, H. Feick, H. Yan, Y. Wu, H. Kind, E. Weber, R. Russo and P. Yang (2001) Room Temperature Ultraviolet Nanowire Nanolasers *Science* 292 1897
- [88] C. Xu, M. Kim, J. Chun and D. Kim (2005) Growth of Ga-doped ZnO nanowires by two-step vapor phase method *Appl. Phys. Lett.* 86 133107
- [89] Y. Qin, X. Wang and Z.L. Wang (2008) Microfibre-nanowire hybrid structure for energy scavenging *Nature* 451 06601
- [90] X. Wang, J. Zhou, J. Song, J. Liu, N. Xu and Z. L. Wang (2007) Piezoelectric Field Effect Transistor and Nanoforce Sensor Based on a Single ZnO Nanowire *Nano Lett.* 6 2768
- [91] Z.L. Wang (2004) Nanostructures of zinc oxide *Materials Today* 6 26
- [92] W.T. Chiou, W.Y. Wu and J.M. Ting (2003) Growth of single crystal ZnO nanowires using sputter deposition *Diamond and Related Materials* 12 1841
- [93] W. Lee, M.C. Jeong and J.M. Myoung (2004) Fabrication and application potential of ZnO nanowires grown on GaAs(002) substrates by metal-organic chemical vapour deposition *Nanotechn.* 15 254
- [94] H.Y. Dang, J. Wang and S.S. Fan (2003) The synthesis of metal oxide nanowires by directly heating metal samples in appropriate oxygen atmospheres *Nanotechnology* 14 738
- [95] H.J. Fan, R. Scholz, F.M. Kolb and M. Zacharias (2004) Two-dimensional dendritic ZnO nanowires from oxidation of Zn microcrystals *Appl. Phys. Lett.* 85 4142
- [96] J.F. Conley Jr., L. Stecker and Y. Ono (2005) Directed assembly of ZnO nanowires on a Si substrate without a metal catalyst using a patterned ZnO seed layer *Nanotechnology* 16 292
- [97] P. Yang, H. Yan, S. Mao, R. Russo, J. Johnson, R. Saykally, N. Morris, J. Pham, R. He and H.J. Choi (2002) Controlled Growth of ZnO Nanowires and Their Optical Properties *Adv. Funct. Mater.* 12 323
- [98] X. Wang, Q. Li, Z. Liu, J. Zhang, Z. Liu, and R. Wang (2004) *Appl. Phys. Lett.* 84 244941
- [99] Q.H. Li, Y.X. Liang, Q. Wan and T.H. Wang (2004) *Appl. Phys. Lett.* 85 266389

- [100] M.J. Zheng, L.D. Zhang, G.H. Li and W.Z. Shen (2002) Fabrication and optical properties of large-scale uniform zinc oxide nanowire arrays by one-step electrochemical deposition technique *Chem. Phys. Lett.* 363 123
- [101] S. Kim, M.C. Jeong, B.Y. Oh, W. Lee and J.M. Myoung (2006) Fabrication of Zn/ZnO nanocables through thermal oxidation of Zn nanowires grown by RF magnetron sputtering *J. of Crystal Growth* 290 485
- [102] M. Ohring (2001) *Material science of thin films* Elsevier
- [103] M. Kast, P. Schroeder, Y.J. Hyun, P. Pongratz and H. Brückl (2007) Synthesis of Single-Crystalline Zn Metal Nanowires Utilizing Cold-Wall Physical Vapor Deposition *Nano Lett.* 8 2540
- [104] The Powder Diffraction Files [Internat. Center for Diffraction Data, PDF 4 831 (Zn) and 36 1451 (ZnO)]
- [105] N. Cabrera and N.F. Mott (1949) Theory of the oxidation of metals *Rep. Prog. Phys.* 12 163; R. Nakamura, J.G. Lee, D. Tokozakura, H. Mori and H. Nakajima (2007) Formation of hollow ZnO through low-temperature oxidation of Zn nanoparticles *Mat. Lett.* 61 1060
- [106] H. B. Lu, H. Li, L. Liao, Y. Tian, M. Shuai, J.C. Li, M.F. Hu, Q. Fu and B.P. Zhu (2008) Low-temperature synthesis and photocatalytic properties of ZnO nanotubes by thermal oxidation of Zn nanowires *Nanotechnology* 19 045605
- [107] Y. Wang, L. Zhang, G. Meng, C. Liang, G. Wang and S. Sun (2001) Zn nanobelts: a new quasi one-dimensional metal nanostructure *Chem. Commun.* 2632
- [108] Z. R. Dai, Z. W. Pan and Z. L. Wang (2003) Novel Nanostructures of Functional Oxides Synthesized by Thermal Evaporation *Adv. Funct. Mater.* 13 9
- [109] X. Wang, J. Song, Z. L. Wang (2006) Single-crystal nanocastles of ZnO *Chem. Phys Lett.* 424 86
- [110] Y. Yang, J. X. Wang, X.W. Sun, B. K. Tay, Z. X. Shen and Y. Z. Zhou (2007) Diamond-shaped ZnO microrrafts and their optical and magnetic properties *Nanotechnology* 18 055709
- [111] K. Yu, Y. Zhang, L. Luo, W. Wang, Z. Zhu, J. Wang, Y. Cui, H. Ma and W. Lu (2004) Growth and optical properties of quadrangular zinc oxide nanorods on copper-filled porous silicon *Appl. Phys. A* 79 443
- [112] H. J. Fan, B. Fuhrmann, R. Scholz, C. Himcinschi, A. Berger, H. Leipner, A. Dadgar, A. Krost, S. Christiansen, U. Gösele and M. Zacharias (2006) Vapour-transport-deposition growth of ZnO nanostructures: switch between *c*-axial wires and *a*-axial belts by indium doping *Nanotechnology* 17 S231
- [113] <http://www.rockhounds.com/rockshop/xtal/part6.html>
- [114] (a) A. Wander, F. Schedin, P. Steadman, A. Norris, R. McGrath, T. S. Turner, G. Thornton and N. M. Harrison (2001) Stability of Polar Oxide Surfaces *Phys. Rev. Lett.* 86 3811; (b) B. Meyer and D. Marx (2003) Density-functional study of the structure and stability of ZnO surfaces *Phys. Rev. B* 67 035403

- [115] H. Peng, S. Meister, C. K. Chan, X. F. Zhang and Y. Cui (2007) Morphology Control of Layer-Structured Gallium Selenide Nanowires *Nano Lett.* 7 199
- [116] J. H. Park, H. J. Choi, Y. J. Choi, S. H. Sohn and J. G. Park (2004) Ultrawide ZnO nanosheets *J. Mat. Chem.* 14 35
- [117] C.X. Wang and G.W. Yang (2005) Thermodynamics of metastable phase nucleation at the nanoscale *Materials Science and Engineering R* 49 157
- [118] T. Burchhart, C. Zeiner, A. Lugstein, C. Henkel and E. Bertagnolli (2011) Tuning the electrical performance of Ge nanowire MOSFETs by focused ion beam implantation *Nanotechnology* 22 035201
- [119] X.L. Chen, Y.C. Lan, J.Y. Li, Y.G. Cao and M. He (2001) Radial growth dynamics of nanowires *J. of Cryst. Growth* 222 586
- [120] (a) M. Pagels, J. Heinze, B. Geschke and V. Rang (2001) A new approach to the mechanism of polymerisation of Oligovinylthiophene *Electrochim. Acta* 46 3943; (b) M. Zhou and J. Heinze (1999) Electropolymerization of Pyrrole and Electrochemical Study of Polypyrrole. 2. Influence of Acidity on the Formation of Polypyrrole and the Multipathway Mechanism *J. Phys. Chem. B* 103 8443; (c) M. Zhou and J. Heinze (1999) Electropolymerization of pyrrole and electrochemical study of polypyrrole: 1. Evidence for structural diversity of polypyrrole *Electrochim. Acta* 44 1733; (d) M. Zhou, M. Pagels, B. Geschke and J. Heinze (2002) Electropolymerization of Pyrrole and Electrochemical Study of Polypyrrole. 5. Controlled Electrochemical Synthesis and Solid-State Transition of Well-Defined Polypyrrole Variants *J. Phys. Chem. B* 106 10065
- [121] (a) A. F. Diaz, K. K. Kanazawa and J. P. Gardini (1979) Electrochemical polymerization of pyrrole *Chem. Soc. Chem. Commun.* 635; (b) K. K. Kanazawa, A. F. Diaz, R. H. Geis, W. D. Gill, J. F. Kwak, J. A. Logan, J. F. Rabolt and G. B. Street (1979) Organic metals: polypyrrole, a stable synthetic metallic polymer *J. Chem. Soc. Chem. Commun.* 854
- [122] M. A. De Paoli and W. A. Gazotti (2002) Conductive polymer blends: preparation, properties and applications *Macromolecular Symposia* 189 83
- [123] (a) T. Dai, X. Yang, Y. Lu (2007) Conductive composites of polypyrrole and sulfonic-functionalized silica spheres *Mater. Lett.* 61 3142; (b) G. Cho, M. Jung, H. Yang, B. Lee and J. H. Song (2007) Photonic crystals with tunable optical stop band through monodispersed silica-polypyrrole core-shell spheres *Mater. Lett.* 61 1086; (c) A. Van Blaaderen, J. Van Geesta and A. Vrij (1992) Monodisperse colloidal silica spheres from tetraalkoxysilanes: Particle formation and growth mechanism *J. Colloid Int. Sci.* 154 481
- [124] C. Debiemme-Chouvy (2008) Template-free one-step electrochemical formation of polypyrrole nanowire array *Electrochem. Commun.* 11 298
- [125] M. Li, Z. Wie and L. Jiang (2008) Polypyrrole nanofiber arrays synthesized by a biphasic electrochemical Strategy *J. Mater. Chem.* 18 2276
- [126] H. Sellers, A. Ulman, Y. Shnidman and J. E. Eilers (1993) Structure and Binding of Alkanethiolates on Gold and Silver Surfaces: Implications for Self-Assembled Monolayers *J. Am. Chem. Soc.* 115 9389

- [127] (a) A. Badia, W. Gao, S. Singh, L. Demers, L. Cuccia and L. Reven (1996) Structure and Chain Dynamics of Alkanethiol-Capped Gold Colloids *Langmuir* 12 5 1262; (b) L. H. Dubois and R. G. Nuzzo (1992) Synthesis, Structure, and Properties of Model Organic Surfaces *Annu. Rev. Phys. Chem.* 63 437
- [128] Thermo scientific instructions NHS and sulfo-NHS (product nr. 24500, 24510, 24520, 24525)
- [129] Dissertation Michael Panhorst (2005) *On-chip manipulation and positioning of biomolecules with magnetic beads* Universität Bielefeld (Division: Thin films and physics of nanostructures) chapter 4
- [130] S. Hoffmann, F. Östlund, J. Michler, H. F. Fan, M. Zacharias, S. H. Christiansen and C. Ballif (2007) Fracture strength and Young's modulus of ZnO nanowires *Nanotechnology* 18 205503
- [131] (a) D. A. Dikin, X. Chen, W. Ding, G. Wagner, and R. S. Ruoff (2003) Resonance vibration of amorphous SiO<sub>2</sub> nanowires driven by mechanical or electrical field excitation *J. Appl. Phys.* 93 1; (b) G. Stan, C. V. Ciobanu, P. M. Parthangal and R. F. Cook (2007) Diameter-Dependent Radial and Tangential Elastic Moduli of ZnO Nanowires *Nano Lett.* 7 3691
- [132] (a) S. Timoshenko, *Theory of Elastic Stability*, McGraw–Hill (1936) New York; (b) R. E. D. Bishop and D. C. Johnson, *Mechanics of Vibration*, Cambridge University Press (1960) Cambridge, U.K.
- [133] M. Merkel, K. H. Thomas (2008) *Taschenbuch der Werkstoffe* 7. Auflage Hansa Leipzig
- [134] S. M. Tanner, J. M. Gray, C. T. Rogers, K. A. Bertness and N. A. Sanford (2007) High-*Q* GaN nanowire resonators and oscillators *Appl. Phys. Lett.* 91 203117
- [135] S. W. Lee, B. Kim, D. S. Lee, H. J. Lee, J. G. Park, S. J. Ahn, E. E. B. Campbell and Y. W. Park (2006) Fabrication and mechanical properties of suspended one-dimensional polymer nanostructures: polypyrrole nanotube and helical polyacetylene nanofibre *Nanotechnology* 17 992
- [136] G. Güntherodt and U. Rüdiger (1999) *Magnetische Schichtsysteme* Sommerschule Forschungszentrum Jülich chapter A9
- [137] Dissertation Volker Höink (2008) *Magnetoresistance and ion bombardment induced magnetic patterning* Universität Bielefeld (Division: Thin films and physics of nanostructures), chapter 2.7.2
- [138] Dissertation Jörg Schotter (2004) *Development of a magnetoresistive biosensor for the detection of biomolecules* Universität Bielefeld (Division: Thin films and physics of nanostructures) chapter 3.2.1
- [139] M. Pardavi-Horvath, P. E. Si, M. Vazquez, W. O. Rosa and G. Badini (2008) Interaction effects in permalloy nanowire systems *J. Appl. Phys.* 103, 07D517
- [140] K. Peng, Y. Xu, Y. Wu, Y. Yan, S. T. Lee and J. Zhu (2005) Aligned Single-Crystalline Si Nanowire Arrays for Photovoltaic Applications *Small* 1 11 1062
- [141] K. Q. Peng, Y. J. Yan, S. P. Gao and J. Zhu (2002) Synthesis of Large-Area Silicon Nanowire Arrays via Self-Assembling Nanoelectrochemistry *Adv. Mater.* 14 64
- [142] J. Liu, S. Lee, K. Lee, Y. H. Ahn, J.Y. Park and K. H. Koh (2008) Bending and bundling of metal-free vertically aligned ZnO nanowires due to electrostatic interaction *Nanotechnology* 19 185607

[143] B. Yameen, H. Duran, A. Best, U. Jonas, M. Steinhart, W. Knoll (2008) Polycyanurate Thermoset Networks with High Thermal, Mechanical, and Hydrolytic Stability Based on Liquid Multifunctional Cyanate Ester Monomers with Bisphenol A and AF Units *Macromol. Chem. Phys.* 209 1673

## Publications

P. Schroeder, J. Schotter, A. Shoshi, M. Eggeling, O. Bethge, A. Hütten and H. Brückl (2011) Artificial cilia of magnetically tagged polymer nanowires for biomimetic mechanosensing (accepted for publication in *Bioinspir. and Biomim.*)

P. Schroeder, M. Kast, E. Halwax, C. Edtmaier, O. Bethge and H. Brückl (2009) Morphology alterations during post-synthesis oxidation of Zn nanowires *J. Appl. Phys.* 105 104307

M. Kast, P. Schroeder, Y. J. Hyun, P. Pongratz and H. Brückl (2007) Synthesis of single-crystalline Zn metal nanowires utilizing cold-wall physical vapor deposition *Nano Lett.* 7 8 2540

## Conferences

Poster at the “NanoSens 2010” conference “Nanosensors for Industrial Applications”, Vienna, December 2<sup>nd</sup> – 3<sup>rd</sup>, 2010

Talk at the “IEEE International Symposium on Metallic Multilayers”, Berkeley, USA, September 19<sup>th</sup> - 24<sup>th</sup>, 2010

Poster at the “1<sup>st</sup> International conference on natural and biomimetic mechanosensong”, Dresden, October 26<sup>th</sup> – 28<sup>th</sup>, 2009

Poster at the “Arge Sensorik” PhD summit, Vienna, July 1<sup>st</sup>, 2009

Poster at the “NanoSens 2008” conference “Nanosensors for Industrial Applications”, Vienna, September 29<sup>th</sup> – 30<sup>th</sup>, 2008

Poster at the “Cilia” Summer School “Mechanosensors: from biological to bionic systems”, Sant Feliu de Guixols, Spain, March 30<sup>th</sup> - April 3<sup>rd</sup>, 2008

## Danksagung

Zuerst bedanke ich mich bei meinem Betreuer PD Dr. Hubert Brückl, der das Projekt des Biomimetischen Beschleunigungssensors im Geschäftsfeld *Nano Systems* des *Austrian Institute of Technology* ins Leben gerufen hat. Ohne seine umfassende Unterstützung und viele hilfreiche Tipps sowie die materielle Unterstützung durch den Wissenschaftsfond FWF (Projektnummer: L332–1416) wäre die Arbeit nicht möglich gewesen.

Des Weiteren gilt mein Dank meinem Betreuer Prof. Dr. Andreas Hütten von der Abteilung *Dünne Schichten und Nanostrukturen* der Universität Bielefeld für die Fernbetreuung und hilfreiche Anmerkungen.

Ich bedanke mich bei Dr. Jörg Schotter für die Betreuung in der Endphase der Arbeit, allgemeine Hilfestellungen, wie z. B. der fachliche Unterstützung bei den mikromagnetischen Simulationen sowie die SEM-Benutzereinführung.

In einem Zug möchte ich Dr. Ole Bethge für außerordentliche Zusammenarbeit im Bereich der „In-situ“ SEM-Charakterisierungen, EDX-Untersuchungen und diverser Probenpräparation, Astrit Shoshi für Unterstützung bei Fragestellungen, die magnetische Partikel und deren Anbindung betreffen, sowie die kollegiale Nutzung der strukturierten Chip-Proben und Moritz Eggeling für seine Hilfe bei der *Labview*-Programmierung und seine konstruktiven Ideen danken. Im Allgemeinen spreche ich ihnen Dank für kontinuierliche fachliche, als auch moralische Unterstützung aus.

Dr. Theodoros Dimopoulos danke ich für die Einführung in die magnetische Kraftmikroskopie und magnetische Transportmessungen. Darüber hinaus bin für seine kompetenten Ratschläge bei der magnetischen Schichtabscheidung und im Speziellen der Realisierung der indirekten magnetischen Austauschkopplung dankbar.

Für die innovative Betreuung der durchgeführten Oxidationsexperimente von Zink Nanodrähten danke ich Dr. Michael Kast. Dr. Markus Milnera danke ich für die aufwendige, unterstützende Arbeit im Rahmen der Lithographie und Chip-Prozessierung. Dr. Thomas Uhrmann danke ich für die Unterstützung bei der anfänglichen magnetischen Probencharakterisierung und die Softwareumstellung auf den alternativen Mess-Stand. Dr. Nadezhda Kataeva danke ich für ihre konstruktive Hingabe bei der Synthese von Kobalt-Nanopartikeln. Leonie Breth danke ich für eine TMR-Probenpräparation sowie allgemeine, hilfreiche Diskussionen. Dr. Antonis Gitsas danke ich für seine kompetente Zusammenarbeit bei der Prozessierung und Anbindung der „thermoset“-Polymerstrukturen und Monika Madl für ihre Zusammenarbeit bei den Crosslinker-Experimenten.

Ein spezieller Dank gilt auch Dr. Rudolph Heer für die AFM-Einführung, als auch für zahlreiche elektrotechnische Expertenratschläge. Ebenfalls wichtig für die Fertigstellung der Arbeit waren die Hilfestellung von Dr. Thomas Maier bei der laboratorischen Infrastruktur, wie z.B. Gasanschlüssen oder der Lithographie und die Einführung in die elektrochemische Abscheidung durch Dr. Peter Ertl.

Vom Kooperationspartner des Sensorprojekts, der Technischen Universität Wien, bedanke ich mich bei Dr. Thomas Burchard und Ass. Prof. Alois Lugstein für die Synthese der halbleitenden Nanodrähte.

Ein außerordentlicher Dank gilt Dr. Samuel Hoffmann für die Bereitstellung von nützlichen Informationen zu den mechanischen Eigenschaften von halbleitenden Nanodrähten und Kerstin Formanek für administrative Unterstützung.

Abschließend bedanke ich mich herzlich für die großartige Arbeitsatmosphäre innerhalb des Geschäftsfelds „Nano Systems“ als auch der Abteilung D2 von der Universität Bielefeld.